Observations of Auroral Plasma Lines

Tom Grydeland

June 2, 1998

To Maya

Contents

Chapter 1

Introduction

Incoherent scattering has, since its conception in the late '50ies, been a valuable tool in observing and diagnosing the ionosphere under various conditions, day and nighttime for more than four full solar cycles.

It is a very sophisticated observation technique, and one which enables us to extract a wealth of information about the plasma state in the ionosphere for extended periods of time at relatively low cost.

In the summer of 1985, observations were made of plasma lines of unprecedented power. These observations have not been analysed and/or interpreted before, and they inspired the current work.

The theory behind incoherent scatter is far from simple. To interpret incoherent scatter data, knowledge of kinetic theory of a plasma is necessary. Adding to the complexity are varying ionisation ratios, precipitating particles, photoionisation, external electric fields etc. Chapter 2 provides a short summary of the theory necessary to interpret such observations. We briefly describe the velocity distributions of particles in the ionosphere, then we use kinetic (Vlasov) theory to examine the streaming instabilities of a plasma. After this comes the crux of the chapter; the calculation of the incoherent scatter radar cross section.

The technique is limited in spatial and temporal resolution; spatial resolution down to 300 m has been obtained, but anything better than this should not be expected. Compared with the sub-meter scale observable by rockets, this is extremely coarse. Current radars regularly run at time resolutions of 5 s, but the low signal-to-noise ratio of incoherent scatter makes it unlikely that much finer time resolution than this can yield data of sufficient quality to be analysed. Incoherent scatter radars are therefore incapable of resolving e.g. fine structure in auroral arcs. Whereas optical instruments can scan sections of the sky in seconds, radars (phased array radars excepted) need to point to the

same volume throughout an integration period, leaving them unable to map the sky like optical instruments can. In this respect, the radar is essentially a point measurement.

Radars naturally have their strengths as well. Rockets trace a ballistic orbit once, and obtaining time series from a point from rocket-based instruments is essentially impossible. Radars regularly observe the same volume for 24 hours or more. Optical instruments have superior time resolution and all-sky capability, but they can only provide us with line-of-sight integrated intensities — tomography must be used to obtain spatial structures — and they are unable to operate during overcast or sunlit conditions, limiting potential observation time significantly. Radars are of course impervious to visible light and are not influenced by clouds or adverse weather.

Throughout the era of incoherent scatter radars, the ion part of the spectrum has received by far the most attention. Although the plasma line was quickly recognised as a valuable diagnostic, plasma line observations are still not part of the regular observation schedule at any of the world's incoherent scatter facilities. Despite the fact that plasma lines have been applied to estimate parameters that are difficult to obtain through standard ion-spectrum analysis, plasma lines cannot be used with the standard analysis programs currently in use.

Strongly enhanced plasma lines have been observed at many of the world's incoherent scatter facilities, and many theories have been developed to explain the observations. The different enhancement mechanisms are reviewed in section 2.4. From the outset, we expected plasma instabilities to be the cause for these strongly enhanced plasma lines. Both linear Vlasov theory and the theory of incoherent scattering assumes a stable plasma, and we have therefore studied how the incoherent scattering cross section is affected when this assumption is invalidated.

The observations that the present work is based on were made during a Norwegian special programme at the European Incoherent Scatter (EISCAT) facilities in Tromsø and Sodankylä on the fourth and fifth of July, 1985. This experiment is described in some detail in chapter 3. In addition to the desired quiet-time observations of photoelectron enhanced plasma lines, very strong plasma lines were observed during two events in the afternoon of July 4th. These observations have not previously been analysed or interpreted.

In chapter 4, the results of the analysis are presented. The presentation includes several plots of the two events analysed and quiet-time data for comparison. We finally discuss different interpretations of the data.

It turns out that the experiment we have analysed is less than ideally suited for observations of the kind of events we have seen. The final chapter, chapter 5 is

therefore a presentation of a design for a new *E*-region plasma line experiment which incorporates some of the recent developments within incoherent scattering, specifically alternating codes. The design is formulated quite broadly and parametrised with a series of parameters in the hope that others will find it useful and that it can be applied to a broader range of observations than we have foreseen at this moment. Possible applications are observations of sporadic *E* and PMSE with simultaneous plasma line observations, something which has not been done previously.

For the existing EISCAT radar systems, the design is realised through a correlator program, which is the same for all experiments of our design, and a parameter driven experiment generation program which creates all the files necessary to run the experiment on the radars and to analyse the data with GUISDAP.

There is currently no realisation of the design for the EISCAT Svalbard Radar.

Acknowledgements

Thanks are due to my supervisor, Noralv Bjørnå, for his devotion and continued interest in this project, and the countless hours he has spent trying to teach me some physics. Thanks also to Patrick Guio, GUISPERT *par excellence*. Without your help none of the data analysis or GUISDAP-related experiment design would ever have been finished.

Thanks to the staff at the EISCAT site at Ramfjordmoen for your skill and competence, and for making my stay with you an educational and pleasant experience. Thanks to Tony for believing in me and my abilities.

Thanks to Unni Pia and César for fruitful discussions, and to Truls and Liv for their help with the riometer and ionosonde figures. Thanks to Sheila Kirkwood for permission to use her figures.

Thanks in particular to my wife, Ane, for enduring me in my perpetually postponed final effort with this thesis.

The EISCAT Scientific Association is supported by National Institute for Polar Research of Japan, the Centre National de la Recherche Scientifique of France, Suomen Akatemia of Finland, Max Planck Gesellschaft of Germany, Norges Forskningsråd of Norway, Naturvetenskapliga Forskningsrådet of Sweden and the Science and Engineering Research Council of the United Kingdom.

Chapter 2

Theory

When trying to understand the observations that inspired the current work, the original assumption was that the enhancements were caused by ionospheric plasma instabilities, similar to the explanation by *Valladares et al.* [1988]. Since, as we will see in section 2.3, the theory of incoherent scattering assumes a stable plasma, a review of this theory where the stability assumptions are emphasised is necessary. This is done in section 2.3.

Also, if we want to examine the observations in terms of instabilities, we will necessarily have to summarise the parts of plasma instability theory that are relevant under ionospheric conditions. Beam-plasma instabilities — expected to occur during precipitation events — are examined, while the configuration space instabilities crucial for laboratory plasma experiments are of little or no interest to us, and are therefore not treated. This is done in section 2.2.

Before exploring any of these subjects in any detail, we shall take a closer look at non-Maxwellian velocity distributions used to model the ionospheric plasma and how the different distributions influence the fundamentals of plasma physics.

2.1 Particle velocity distributions in the ionosphere

A direct measurement of the energy spectrum of precipitating particles, be it electrons or protons, requires *in situ* instruments, meaning balloons, rockets or satellites, depending on the altitude.

Direct rocket measurements of photoelectron fluxes have been made by e.g. *Doering et al.* [1970] and *Sharp and Hays* [1974]. Similar measurements of proton fluxes as a function of energy and pitch-angle was made by *Søraas et al.* [1974]. Direct satellite measurements have been made by e.g. *Knudsen* [1972]; *Wrenn*

[1974] (above 500 km), and *Frank et al.* [1976] (above 677 km). Recent rocket and satellite measurements seem to concentrate on energies from 10 keV and upwards.

Indirect measurements of the suprathermal electron flux can be made by incoherent scatter radar plasma line observations. In a collisionless plasma where the suprathermal population is small enough that the background plasma still can be accurately described by a Maxwellian velocity distribution, the total power in the plasma line depends only on the logarithmic derivative of the suprathermal distribution function at the phase velocity of the Langmuir wave [*Perkins and Salpeter*, 1965]. The full velocity distribution cannot be measured directly, due to e.g. only one measured point at each altitude and the radar seeing only waves of a single $\boldsymbol{k}$.

Radar measurements of suprathermal electron velocity distributions under these assumptions have been made by e.g. *Cicerone* [1974]; *Carlson et al.* [1977] and *Kofman and Lejeune* [1980],

There are also several authors that have simulated particle precipitation in the ionosphere under various circumstances [e.g. *Stamnes and Rees*, 1983; *Min et al.*, 1993; *Lummerzheim and Lilensten*, 1994].

As pointed out by *Cicerone* [1974] and *Wrenn* [1974], discrepancy between calculated and measured particle fluxes is most likely due to a lack of suitable input data for theoretical computations.

As indicated above, the customary way of modelling the ionospheric plasma is as a Maxwellian background, sometimes with a (small) population of nonthermal particles. These suprathermal particles are then modelled, usually by assuming a flux with an inverse power-law dependency on energy. Sometimes more advanced techniques are used. *Kirkwood et al.* [1995] uses the electron density profile as input to a numerical model for calculating the suprathermal flux.

Since the power-law distribution diverges for low energies, it can only be used in a limited energy interval. A different analytical model, using a generalised Lorentzian or kappa distribution, has been used in magnetospheric physics, but has rarely been used in ionospheric modelling. The kappa distribution combines similarity with the Maxwellian at low energies and a high-energy tail similar to a power-law, while remaining continuous at all energies. It also has desirable analytical properties. We therefore expect that ionospheric modelling could be improved by using kappa distributions instead of Maxwellian distributions in many cases. The limits of applicability of the kappa distribution will have to be determined.

2.1.1 Maxwellian distribution functions

It is customary in plasma physics to assume a thermal or near-thermal situation. This means that we assume Maxwellian velocity distributions, or at least that the departure from the Maxwellian is small enough that it can be expanded as a series.

The velocity distribution in a plasma will tend towards the Maxwellian on a timescale of the order of the interparticle collision time.

The three-dimensional Maxwellian is defined as

$$f_{\mathrm{M}}(\boldsymbol{v}) = \frac{1}{\pi^{3/2}\theta^3} \exp\left\{-\frac{v^2}{\theta^2}\right\} \tag{2.1}$$

and by integrating this function as in (A.6), the one-dimensional Maxwellian becomes

$$F_{\mathrm{M}}(u) = \frac{1}{\sqrt{\pi}\theta} \exp\left\{-\frac{u^2}{\theta^2}\right\} \tag{2.2}$$

In the above equations, we interpret θ as the thermal velocity of the particles; a characteristic velocity of the particles which defines the temperature of the species.

As demonstrated by observations and simulations, the departure from the Maxwellian can be significant in the ionosphere, particularly at higher energies. (In the magnetosphere and in the solar wind, the departure is even greater.)

2.1.2 Power-law distributions

A common feature of all measured and calculated velocity distributions is the presence of more particles at high velocities (greater than the thermal velocity of the distribution) than the background Maxwellian. These particles are called suprathermal, and they are often treated as a separate particle species.

Many plasma line studies use a power-law distribution to model suprathermal particles. Already the first investigation of the effects of suprathermal electrons on the plasma line by *Perkins and Salpeter* [1965] used a velocity distribution $\propto u^{-s}$ as an example.

Several of the references cited above on calculated and directly or indirectly measured electron and proton fluxes (see also the flux used by *Kirkwood et al.* [1995, Figure 7], which was calculated according to the procedure of *Lummerzheim and Lilensten* [1994]) suggest that we can describe the flux of particles in a limited energy range $E_1 < E < E_2$ by an inverse power-law flux:

$$J(E, \Theta) = KE^{-\gamma} P(\Theta) \tag{2.3}$$

where E is the energy of the particles, Θ is the pitch angle and $P(\Theta)$ is the pitch-angle distribution. This distribution has the attractive property that it leads to analytical expressions for integral and half-integral values for γ, while fitting observed and modelled particle energy spectra well, particularly for energies above 10 eV. Depending on the ionospheric conditions, the lower limit of validity for a power law distribution lies between 4 and 6 eV. Below 6 eV, a power law should only be used with some caution, while below 4 eV it should not be used at all. For backscatter measurements with the EISCAT UHF radar, 6 eV is the energy of electrons at the velocity matching the phase velocity of Langmuir waves of ≈ 9 MHz, which again corresponds to a density of $10^{12}\,\mathrm{m}^{-3}$, which we only expect during strong auroral precipitation. Electron energy of 4 eV corresponds to 7.4 MHz Langmuir waves, or $\approx 7 \cdot 10^{11}\,\mathrm{m}^{-3}$. For the VHF radar system, 6 eV corresponds to ≈ 2.2 MHz or $5.8 \cdot 10^{10}\,\mathrm{m}^{-3}$, which is reasonable to expect under any circumstances where observations can be made. We therefore conclude that a power-law distribution should only be used for UHF plasma line modelling at offsets > 7.5 MHz, and even then only with some caution. (The exact offset limit will be different for bistatic measurements.) For VHF radar plasma line observations, modelling suprathermal electrons with a power-law appears to be reasonably accurate.

The pitch angle distribution is modelled by the function $P(\Theta) = |\cos\Theta|^n$, $n \in \mathbb{Z}$ with Θ being the pitch angle. This form contains the important special case of isotropic flux ($n = 0$), while it is capable of modelling increasingly monodirectional fluxes for increasing n. For integral n it allows the analytical calculation of the IS plasma-line spectrum. The case $n = 1$ was employed by *Yngvesson and Perkins* [1968] and justified with physical arguments. *Cicerone and Bowhill* [1971] has achieved similar pitch-angle distributions for outflowing electrons with a Monte Carlo simulation. *Cicerone* [1974] speculates that this model is likely not valid for downflowing electrons.

On the strength of this evidence and the mathematical convenience of the model, for plasma line enhancement purposes we often model suprathermal particles in a limited energy range $E_1 < E < E_2$ by a velocity distribution function

$$f_\alpha^{\mathrm{pl}}(v) = \frac{K}{n_\alpha}\frac{m}{v^2}E^{-\gamma}\,|\cos\Theta|^n \tag{2.4}$$

There is of course a problem with the continuity of this distribution at the lower energy range.

2.1.3 The kappa distribution function

As we noted in the previous section, the power-law distribution is unsuitable for modelling suprathermal electron distributions at some of the ener-

gies influencing plasma lines on the EISCAT UHF system. An alternative is to model the suprathermal particles by a velocity distribution that often arises in the studies of magnetospheric and interplanetary plasmas, namely the *kappa*, or generalised Lorentzian, distribution. The kappa distribution has not been used much in ionosphere modelling, despite its popularity in magnetospheric physics, solar wind/interplanetary plasmas and laboratory plasmas. A recent paper [*Frahm et al.*, 1997] attempts to fit measured energy spectra to a kappa distribution in the ionosphere.

The kappa distribution has many interesting properties. *Vasyliunas* [1968] was probably the first to express the kappa distribution in its general form, and he also noted its relation to the Maxwell distribution. Furthermore, it has been shown [*Hasegawa et al.*, 1985] to be an equilibrium distribution for a plasma immersed in suprathermal electric field fluctuations.

From a theoretical viewpoint, the kappa distribution is interesting in that its dispersion function, Z^*_κ — analogous to the dispersion function Z defined by *Fried and Conte* [1961] for a Maxwellian distribution — has a closed form representation for small integer values of κ, and this allows far more calculations to be carried out analytically than is possible with a Maxwellian. The modified dispersion function Z^*_κ was defined by *Summers and Thorne* [1991].

The three-dimensional kappa distribution is given by

$$f_\kappa(\boldsymbol{v}) = \frac{C_\kappa}{\pi^{3/2}\theta^3}\left(1+\frac{v^2}{\kappa\theta^2}\right)^{-(\kappa+1)}, \tag{2.5}$$

while the one-dimensional kappa distribution is

$$F_\kappa(u) = \frac{C_\kappa}{\sqrt{\pi}\theta}\left(1+\frac{u^2}{\kappa\theta^2}\right)^{-\kappa}, \tag{2.6}$$

In both cases, the normalisation is

$$C_\kappa = \frac{\Gamma(\kappa+1)}{\kappa^{3/2}\Gamma(\kappa-\frac{1}{2})}$$

and the definition (A.7) of temperature defines the thermal velocity for these distributions:

$$T_\alpha = m_\alpha \int v^2 F_\kappa \, d\boldsymbol{v} = \frac{m_\alpha C_\kappa}{\theta\sqrt{\pi}} \underbrace{\int_{-\infty}^{\infty} \frac{u^2\,du}{(1+u^2/\kappa\theta^2)^\kappa}}_{I}$$

The integral I can be found in e.g. [*Rottmann*, 1984]

$$I = \frac{\kappa^{3/2}\theta^3\sqrt{\pi}}{2}\frac{\Gamma(\kappa - 3/2)}{\Gamma(\kappa)}$$

We now arrive at the temperature of the distribution (2.6)

$$T_\alpha = \frac{m_\alpha\theta^2\sqrt{\pi}}{2}\frac{\kappa}{\kappa - 3/2}$$

which again gives us the thermal velocity of the kappa distribution

$$\theta = \sqrt{\frac{2\kappa - 3}{\kappa}}\sqrt{\frac{T}{m}} \tag{2.7}$$

As $\kappa \to \infty$, the kappa distribution tends towards a Maxwellian. In addition, all the definitions and results calculated from these distributions tend toward the familiar Maxwellian results. In this sense, the kappa distribution is a generalisation of the Maxwellian distribution.

A plot of f_κ as a function of normalised velocity $x = v/\theta$ for several values of κ is shown in figure 2.1. The Maxwellian is also plotted for comparison.

An investigation of the properties of the kappa distribution and the modified plasma dispersion function, Z^*_κ, was carried out by *Summers and Thorne* in a series of papers [*Summers and Thorne*, 1991, 1992; *Thorne and Summers*, 1991].

We see how the kappa distribution resembles a Maxwellian distribution at low energies, while it has a high energy tail resembling a power-law distribution. Lower values for κ means more particles at higher energies. This means that the kappa distribution could provide a link between Maxwellian and power-law distributions, avoiding the discontinuity mentioned previously. There is a serious limitation, however. Experimentally determined fluxes tend to decrease more steeply at higher energies, often warranting two or more power-law fluxes with increasing γ, while the kappa distribution will not exhibit this steepening.

We still feel that the kappa distribution is a valuable tool for modelling the ionospheric plasma. The properties of a kappa plasma are readily studied, and incoherent scatter from a kappa plasma should be examined for possible inclusion in the analysis procedure.

2.2 Plasma instabilities

In this section we present the parts of the theory of instabilities in a plasma which we need in order to examine the ionospheric plasma. We present one classification of instabilities, and we develop the analytical expressions for

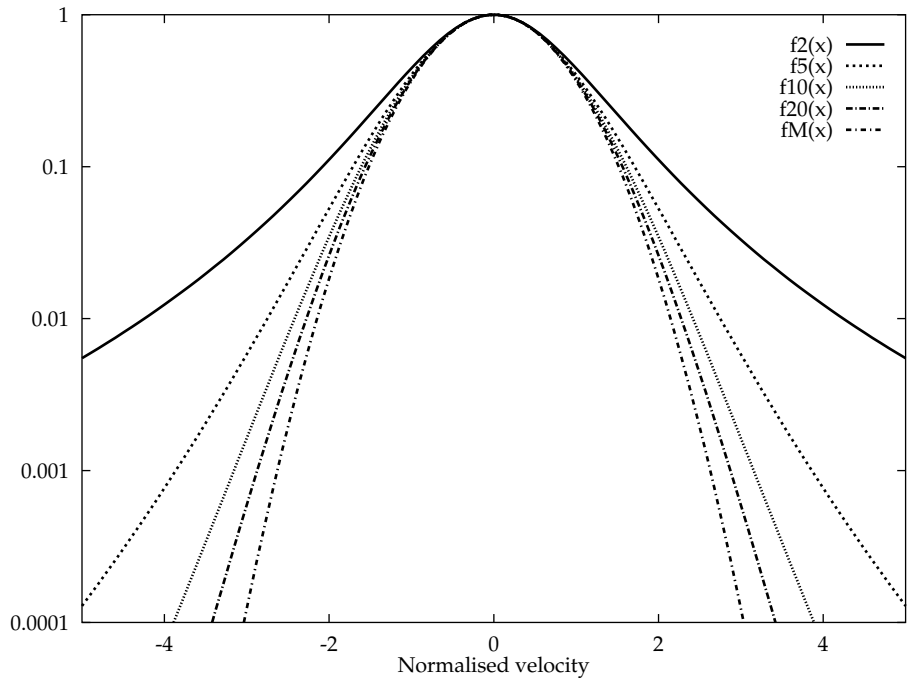

Figure 2.1: A plot of kappa distributions for several values of kappa. The Maxwell distribution function is included for comparison

some relevant special cases in two different descriptions of a plasma. Our description is based on the presentation in *Krall and Trivelpiece* [1973].

For stability analysis, one first needs an equilibrium. This means that the external and internal forces on the plasma, such as pressure, forces due to external electric and/or magnetic fields, gravity etc. must balance. When we have an equilibrium, we can decide whether this equilibrium is stable or not. Stability is achieved when no perturbation of the plasma can cause it to depart significantly from its equilibrium state. If any perturbation causes oscillations to grow, the plasma is unstable.

For our purposes, this is not a very practical definition. At the outset, we're not very concerned with confinement, nor with wavenumber vectors invisible to the radar (e.g. in directions other than directly towards or away from the radar in the case of backscatter; for bistatic measurements the only visible vectors are along the bisection angle) or frequencies that fall outside our filters. Such instabilities might still be indirectly observable, as they can provide an energy input to other forms of collective behaviour at wave vector/frequency ranges that the radar can see.

Because of the wide range of instabilities possible in a plasma, some sort of classification is desirable. There are many possible classifications, and we employ one which is used with some modifications in [e.g. *Krall and Trivelpiece*, 1973; *Cairns*, 1985]. An example of a different classification is the one used by *Chen* [1984], which classifies the instabilities by where the energy driving them comes from.

2.2.1 Classification of instabilities

The simplest plasma stable against all possible perturbations is an infinite, uniform plasma with a Maxwellian velocity distribution. This configuration is, of course, difficult to achieve in practice. Other configurations tend to display a wide range of different behaviours which will let the state of the plasma evolve towards a uniformly distributed plasma with a Maxwellian velocity distribution.

When classifying instabilities, the first distinction we make is between instabilities that are due to the overall macroscopic configuration of the plasma and instabilities due to departure from the Maxwellian velocity distribution. The former are called macroinstabilities, while the latter are called microinstabilities.

Macroinstabilities are due to inhomogenities in the plasma which are not properly balanced and stabilised by other forces. Such instabilities will often cause bulk movement of the plasma causing it to become more homogenous. Typical macroinstabilities are the "kink" and "sausage" instabilities of the Z-pinch and the Rayleigh-Taylor instability. For the description of macroinstabilities, ideal MHD is often sufficient, although sometimes a many-fluid description is necessary.

Microinstabilities, on the other hand, are instabilities which will arise from the velocity distribution of the various particle species in the plasma regardless of the macroscopic configuration. Typical microinstabilities are the loss-cone instability of the magnetic bottle, the "bump-on-tail" instability and the family of streaming instabilities.

Subdividing instabilities further, we classify them as to whether they induce a magnetic field ($\nabla \times \boldsymbol{E}_1 \neq 0$) or not. The instabilities that do will be called electromagnetic instabilities, while the ones that don't will be called electrostatic.

2.2.2 Instabilities in the fluid description

Most instabilities that can be described by a fluid model are macroinstabilities, e.g. the family of pinch instabilities and the Rayleigh-Taylor instability. It is,

however, also possible to describe a class of instabilities called *streaming instabilities*, *drift instabilities* or *two-stream instabilities* in the fluid model. These are configurations in which different species of plasma, treated as different fluids, are flowing relatively to each other. These instabilities include ion-ion two-stream instability, electron-ion two-stream instability and electron-electron two-stream instability. We examine the latter of these in more detail below.

Electron-electron two-stream instability

We consider the case of two uniform electron beams in the z-direction in a uniform, unmagnetised plasma. The ions are assumed to be stationary, restricting our discussion to high-frequency phenomena. Denoting the two beams by the index $s \in \{\alpha, \beta\}$ and assuming a density variation $n_s(z,t) = n_{s0} + \widehat{n}_{s1}\exp\{ikz - i\omega t\}$, and a similar velocity variation, the linearised continuity equation takes the form

$$-i\omega\widehat{n}_{s1} + ik(n_{s0}\widehat{V}_{s1} + \widehat{n}_{s1}V_{s0}) = 0, \tag{2.8}$$

while the momentum equation becomes

$$-i\omega\widehat{V}_{s1} + ik(V_{s0}\widehat{V}_{s1}) = \frac{-e}{m_e}\widehat{E}_1. \tag{2.9}$$

Since we have restricted ourselves to high-frequency phenomena and assume stationary ions, we must use Poisson's equation to determine the electric field. The background ions neutralise everything except the density variations in the beams, so Poisson's equation becomes

$$ik\widehat{E}_1 = \frac{-e}{\varepsilon_0}(\widehat{n}_{\alpha 1} + \widehat{n}_{\beta 1}). \tag{2.10}$$

Solving (2.9) for $\widehat{V}_{s1}$ and inserting this into (2.8), solving the latter for $\widehat{n}_{s1}$ yields

$$\widehat{n}_{s1} = \frac{n_{s0}\widehat{V}_{s1}}{\frac{\omega}{k} - V_{s0}},$$

which we insert into (2.10), and obtain

$$ik\widehat{E}_1 = ik\widehat{E}_1\left[\sum_s \frac{n_{s0}e^2/m_e\varepsilon_0}{(\omega - kV_{s0})^2}\right].$$

When we define the plasma frequency for each beam, $\omega_{ps}^2 = n_{s0}e^2/m_e\varepsilon_0$, this finally gives us the *dispersion relation*

$$1 - \sum_s \frac{\omega_{ps}^2}{(\omega - kV_{s0})^2} = 0. \tag{2.11}$$

The dispersion relation (2.11), cannot generally be solved analytically. Instead of pursuing numeric solutions, we examine the special case when the two beams satisfy

$$\frac{\omega_{p\alpha}^2}{V_{\alpha 0}^2} = \frac{\omega_{p\beta}^2}{V_{\beta 0}^2}.$$

This includes the important special case of counterstreaming beams of equal density and speed.

For mathematical convenience, we define a harmonic average velocity

$$\frac{1}{V_0} = \frac{1}{2}\left(\frac{1}{V_{\alpha 0}} + \frac{1}{V_{\beta 0}}\right), \tag{2.12}$$

and an average plasma frequency

$$\frac{\omega_p^2}{V_0^2} = \frac{\omega_{ps}^2}{V_{s0}^2}, \qquad s \in \{\alpha, \beta\}. \tag{2.13}$$

We further define a dimensionless frequency, x, and wavenumber, y, by the relations

$$x = \frac{\omega}{\omega_p}\frac{V_{\beta 0} - V_{\alpha 0}}{V_{\beta 0} + V_{\alpha 0}}, \qquad k = \frac{\omega}{V_0} + y\frac{\omega_p}{V_0}.$$

These transformations reduce the dispersion relation to the following simple form:

$$\frac{1}{(x+y)^2} + \frac{1}{(x-y)^2} = 1 \tag{2.14}$$

We notice that although this simplified dispersion relation is completely symmetric in x and y, this symmetry does not immediately hold for ω and k due to the ω-dependence of y.

When solving (2.14) for x or y, we obtain complex roots whenever $0 < x^2 < 2$ or $0 < y^2 < 2$. In terms of frequency, this translates to instability whenever

$$0 < \omega < \sqrt{2}\left(\frac{V_{\alpha 0} + V_{\beta 0}}{V_{\alpha 0} - V_{\beta 0}}\right)\omega_p \tag{2.15}$$

For temporal growth, the kinetic treatment of section 2.2.4 is more suited.

2.2.3 Instabilities in the kinetic description

The kinetic equations (i.e. the Liouville equation or the Klimontovich equation) contain all the information necessary to obtain the exact orbit in $(\boldsymbol{x}, \boldsymbol{v})$-space of

every particle in the plasma at every moment in time. The kinetic description is therefore *complete*, in that it contains all the information available about the plasma.

The kinetic description being the most detailed of the plasma descriptions, it is — in theory — always possible to describe and examine an instability in this description.

For all practical purposes, however, this description is far too detailed. The exact orbits of the particles are of no interest to us. We are only interested in the macroscopic behaviour of the plasma. We want to know the local densities, velocities, temperatures, pressures etc.

We separate the kinetic equation into terms from collective and discrete effects and obtain the *Boltzmann equation*

$$\frac{Df}{Dt} \equiv \frac{\partial f}{\partial t} + (\nabla_r \cdot \boldsymbol{v})f + \left(\nabla_v \cdot \frac{\boldsymbol{F}}{m}\right) f = \left(\frac{df}{dt}\right)_{\text{coll}} \tag{2.16}$$

where D/Dt is the *convective derivative* over phase space, and $(df/dt)_{\text{coll}}$ is the change in the distribution function due to collisions. In this equation, all collective effects are collected on the left hand side, while discrete effects are on the right hand side. This means that the force in the acceleration term is only the average experienced force.

If we restrict ourselves to timescales shorter than the typical intercollision time, we can neglect the collision terms, and we arrive at the *Vlasov equation*, or collisionless Boltzmann equation

$$\frac{\partial f}{\partial t} + (\nabla_r \cdot \boldsymbol{v})f + \left(\nabla_v \cdot \frac{\boldsymbol{F}}{m}\right) \cdot f = 0 \tag{2.17}$$

Considering only the electromagnetic forces, the Vlasov equation takes the form

$$\frac{\partial f}{\partial t} + \boldsymbol{v} \cdot \nabla_r f + \frac{q}{m}(\boldsymbol{E} + \boldsymbol{v} \times \boldsymbol{B}) \cdot \nabla_v f = 0 \tag{2.18}$$

Again, the fields appearing in this equation are the macroscopic fields; an average over suitable time and space.

Neglecting the discrete terms when developing the Vlasov equation from the Boltzmann equation is equivalent to a limiting process where the particles are divided into ever smaller parts while keeping the total charge and mass and the charge/mass ratio of each particle. The Vlasov description is therefore also a fluid model in the sense that it has no discrete particles, but one in which the fluid has a velocity distribution.

The dispersion relation

We study the development of an electrostatic disturbance in a uniform and stationary plasma. The reason for presenting such a well-know development here is that the manipulations performed here are similar to the ones we will need in section 2.3.1 on dressed test particles, and writing these out in full with the added complexity of a test charge will only clutter the presentation with unnecessary detail.

The distribution function of particle population α is given by

$$f_\alpha(\boldsymbol{r}, \boldsymbol{v}, t) = n_\alpha f_{0\alpha}(\boldsymbol{v}) + f_{\alpha 1}(\boldsymbol{r}, \boldsymbol{v}, t) \tag{2.19}$$

where $f_{\alpha 0}$ represents the uniform and stationary background plasma which is normalised to unity. The disturbance $f_{\alpha 1}$ is a first-order (small) quantity.

Inserting these distributions into the Vlasov equation, (2.18), the zeroth order terms disappear. Retaining only the first-order terms and electric forces, the linearised Vlasov equation becomes

$$\frac{\partial f_{1\alpha}}{\partial t} + \boldsymbol{v} \cdot \nabla_r f_{1\alpha} = \frac{q_\alpha n_\alpha}{m_\alpha} \nabla_r \Phi(\boldsymbol{r}, t) \cdot \nabla_v f_{0\alpha}$$

Fourier-Laplace transformed, this equation takes the form

$$\begin{aligned} -i(\omega - \boldsymbol{k} \cdot \boldsymbol{v}) f_{1\alpha}(\boldsymbol{k}, \omega) &= f_{1\alpha}(\boldsymbol{k}, \boldsymbol{v}, t = 0) + i \frac{q_\alpha n_\alpha}{m_\alpha} (\boldsymbol{k} \cdot \nabla_v f_{0\alpha}) \Phi(\boldsymbol{k}, \omega) \\ f_{1\alpha} &= -\frac{q_\alpha n_\alpha}{m_\alpha} \frac{\boldsymbol{k} \cdot \nabla_v f_{0\alpha}}{\omega - \boldsymbol{k} \cdot \boldsymbol{v}} \Phi(\boldsymbol{k}, \omega) + i \frac{f_{1\alpha}(t = 0)}{\omega - \boldsymbol{k} \cdot \boldsymbol{v}} \end{aligned} \tag{2.20}$$

where $f_{1\alpha}(t = 0)$ is the initial value for the Laplace transform. Integrating over velocity, we obtain

$$n_{1\alpha}(\boldsymbol{k}, \omega) = -\frac{k^2 \varepsilon_0}{q_\alpha} \chi_\alpha(\boldsymbol{k}, \omega) \Phi + i \frac{f_{1\alpha}(t = 0)}{\omega - \boldsymbol{k} \cdot \boldsymbol{v}} \tag{2.21}$$

where

$$\chi_\alpha(\boldsymbol{k}, \omega) = \frac{\omega_{p\alpha}^2}{k^2} \int \frac{\boldsymbol{k} \cdot \nabla_v f_{0\alpha}(\boldsymbol{v})}{\omega - \boldsymbol{k} \cdot \boldsymbol{v}} \, d\boldsymbol{v} \tag{2.22}$$

is the *susceptibility* of species α.

Poisson's equation relates the perturbation in the electric field to a charge density perturbation

$$\nabla^2 \Phi(\boldsymbol{r}, t) = -\frac{\rho}{\varepsilon_0} = -\sum_\alpha \frac{q_\alpha}{\varepsilon_0} n_{1\alpha}(\boldsymbol{r}, t)$$

Fourier-Laplace transforming this equation yields

$$-k^2\Phi(\boldsymbol{k},\omega) = -\sum_\alpha \frac{q_\alpha}{\varepsilon_0} n_{1\alpha}(\boldsymbol{k},\omega) \tag{2.23}$$

Inserting (2.21) in this expression, we obtain

$$\left[1+\sum_\alpha \chi_\alpha(\boldsymbol{k},\omega)\right]\Phi(\boldsymbol{k},\omega) = \sum_\alpha \frac{iq_\alpha}{\varepsilon_0 k^2}\int \frac{f_{1\alpha}(t=0)}{\omega-\boldsymbol{k}\cdot\boldsymbol{v}}\,d\boldsymbol{v}$$

We define

$$\epsilon = 1+\sum_\alpha \chi_\alpha \tag{2.24}$$

as the *dielectric function* of the plasma. We see how the dielectric function defines the response of the plasma to an electric disturbance. Equating the dielectric function to zero gives us the *dispersion relation* of electrostatic waves in the plasma.

Looking for a solution in the time domain, we try to compute the inverse of the Laplace transform:

$$\Phi(\boldsymbol{k},\omega) = \sum_\alpha \frac{iq_\alpha}{\varepsilon_0 k^2}\frac{1}{\epsilon(\boldsymbol{k},\omega)}\int \frac{f_{1\alpha}(t=0)}{\omega-\boldsymbol{k}\cdot\boldsymbol{v}}\,d\boldsymbol{v}$$

$$\Phi(\boldsymbol{k},t) = \frac{1}{2\pi}\int_L \Phi(\boldsymbol{k},\omega)e^{-i\omega t}d\omega, \tag{2.25}$$

where the contour L in the last integral has to pass *over* all the poles of $\Phi(\boldsymbol{k},\omega)$. The idea in evaluating this integral is to deform the contour according to the prescription given by *Landau* [1946]. Now, the evaluation of $\Phi(\boldsymbol{k},\omega)$ involves integrals of the form $\int(\omega-\boldsymbol{k}\cdot\boldsymbol{v})^{-1}d\boldsymbol{v}$, defined only on the half-plane where $\omega_i > 0$. Therefore, care must be taken that these functions remain analytical when the countour crosses the real ω-axis. The *analytical continuation* of χ, and thus ϵ, from the upper to the lower half-plane is again given by the Landau prescription. Deforming the contour as sketched in figure 2.2, the contribution from the various straight line segments vanish; some immediately, some statistically, and some in a long time limit. The only remaining contribution is from the encircling of the poles of the integrand. Inspecting the integrand, we see that there are two kinds of poles; poles of the integrated initial value, $\int f_{1\alpha}(t=0)(\omega-\boldsymbol{k}\cdot\boldsymbol{v})^{-1}d\boldsymbol{v}$, and zeroes of $\epsilon(\boldsymbol{k},\omega)$. The first kind of pole is transient, and does not convey information on the plasma state in general. The second kind of pole depends on the background distribution of the different species present in the plasma and is independent of the initial value. This is

the kind of pole that gives us information on the macroscopic behaviour of the plasma. Summation over these poles gives us

$$\begin{aligned}\Phi(\boldsymbol{k},t) &= \frac{1}{2\pi}\cdot 2\pi i \sum_j \mathrm{Res}(\Phi(\boldsymbol{k},\omega)\, e^{-i\omega t};\ \omega=\omega_j) \\ &= \frac{q_\alpha}{\varepsilon_0 k^2}\sum_j \frac{1}{\partial\epsilon/\partial\omega|_{\omega=\omega_j}} e^{-i\omega_j t}\int \frac{f_{1\alpha}(t=0)}{\omega_j-\boldsymbol{k}\cdot\boldsymbol{v}}\,d\boldsymbol{v}\end{aligned}$$

where ω_j are the zeroes of $\epsilon(\boldsymbol{k},\omega)$. The behaviour of the plasma after an initial transient period is therefore composed of oscillations at the frequencies $\mathrm{Re}\,\omega_j$, each damped as $\exp\{\mathrm{Im}\,\omega_j t\}$, where ω_j are the normal modes of the plasma. Modes with $\mathrm{Im}\,\omega_j < 0$ are decaying, while modes with $\mathrm{Im}\,\omega_j > 0$ are growing. After a while, the mode with the largest imaginary part of the frequency is dominant.

Any zeroes with large negative imaginary frequency will be heavily damped just like the transients. Albeit zeroes of the dielectric function, these modes will therefore not be called normal modes.

As we can see from the above discussion, the normal plasma response to a disturbance after an initial transient period is composed of oscillations on a limited number of frequencies, each with its own damping rate, where these frequencies are given as solutions to the dispersion relation

$$\epsilon(\boldsymbol{k},\omega) = 1+\sum_\alpha \frac{\omega_{p\alpha}^2}{k^2}\int \frac{\boldsymbol{k}\cdot\nabla_v f_{0\alpha}(\boldsymbol{v})}{\omega-\boldsymbol{k}\cdot\boldsymbol{v}}\,d\boldsymbol{v} = 0 \tag{2.26}$$

Through the definition

$$f(\boldsymbol{v}) = \sum_\alpha \frac{m_e}{m_\alpha} f_{0\alpha}(\boldsymbol{v})$$

the dispersion relation for electrostatic waves becomes

$$1+\frac{\omega_{pe}^2}{k^2}\int \frac{\boldsymbol{k}\cdot\nabla_v f(\boldsymbol{v})}{\omega-\boldsymbol{k}\cdot\boldsymbol{v}}\,d\boldsymbol{v} = 0 \tag{2.27}$$

Integrating over the perpendicular velocity components, we obtain the one-dimensional dispersion relation

$$1-\frac{\omega_{pe}^2}{k^2}\int_{-\infty}^{\infty}\frac{\partial F/\partial u}{u-\omega/k}\,du = 0 \tag{2.28}$$

The linear Vlasov theory leading up to the dispersion relation for electrostatic waves, (2.27), assumes a stable background and a small perturbation of this

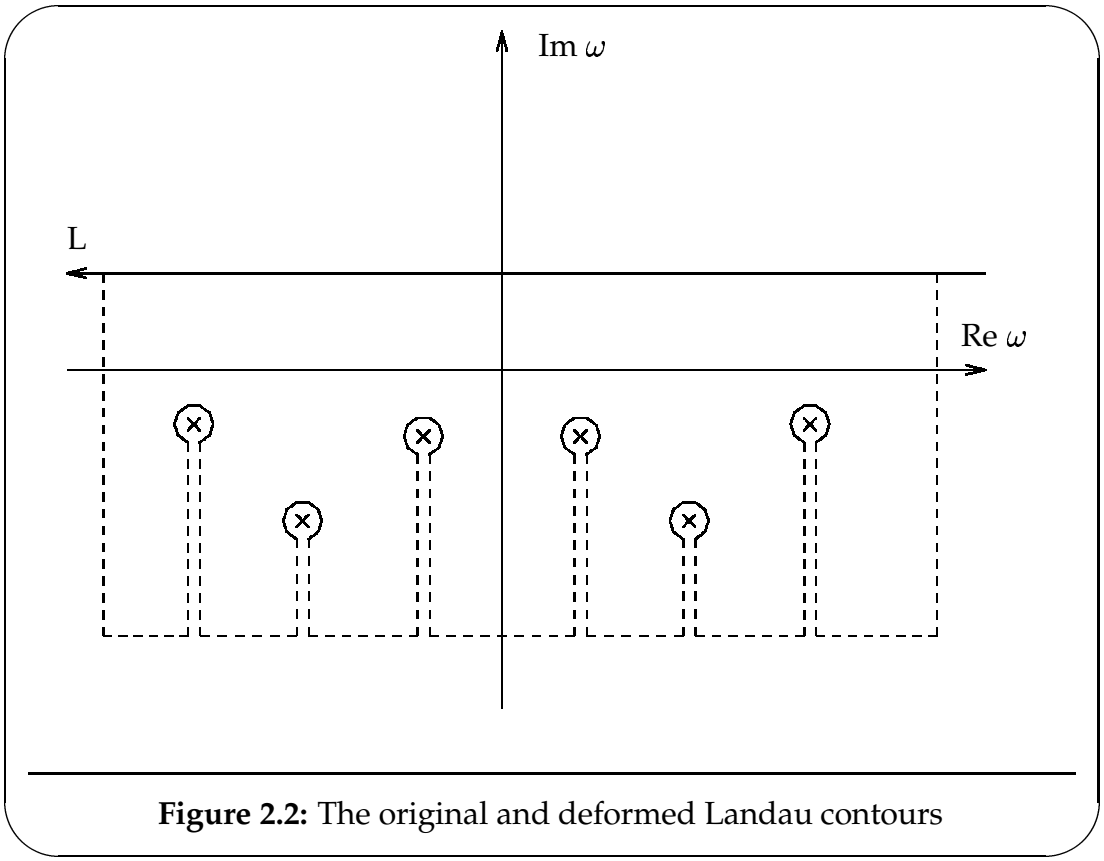

Figure 2.2: The original and deformed Landau contours

background. This means that when applying this theory to instabilities — growing perturbations — the assumption of a small perturbation will break down quite quickly unless there are mechanisms to transport the energy away from the growing mode or limit the energy available for the growth. Such effects are not contained in the linear theory presented here. Consequently, the theory presented here can only be used to identify the initial growth phase of an instability and what frequencies/wave vectors it will appear on. Any saturation and/or damping (which eventually must occur) must be described in a more complete picture than linear Vlasov theory.

The condition for instability and Gardner's Theorem

We investigate the limits of stability as given by (2.27).

If $\omega_i > 0$, then the disturbance described by the first-order term in (2.19) will grow in time, and our plasma is *unstable*. For these cases, the integral in (2.27) can be evaluated directly — the pole is on the correct side of the contour already — and by expressing the frequency as a sum of its real and imaginary

parts;

$$\frac{1}{u-\omega/k} = \frac{(u-\omega_r/k)+i\omega_i/k}{(u-\omega_r/k)^2+(\omega_i/k)^2}$$

we can equal the real and imaginary parts of the dispersion relation to zero separately. This gives us

$$1-\frac{\omega_{pe}^2}{k^2}\int_{-\infty}^{\infty}\frac{u-\omega_r/k}{(u-\omega_r/k)^2+(\omega_i/k)^2}\frac{\partial F}{\partial u}\,du = 0 \tag{2.29a}$$

and

$$\frac{\omega_{pe}^2}{\omega^2}\frac{i\omega_i}{k}\int_{-\infty}^{\infty}\frac{\partial F/\partial u}{(u-\omega_r/k)^2+(\omega_i/k)^2}\,du = 0 \tag{2.29b}$$

By (2.29b), the ω_r/k part of the integral in (2.29a) disappears, and we obtain the following conditions for instability:

$$1-\frac{\omega_{pe}^2}{k^2}\int_{-\infty}^{\infty}\frac{u\partial F/\partial u}{(u-\omega_r/k)^2+(\omega_i/k)^2}\,du = 0 \tag{2.30a}$$

and

$$\int_{-\infty}^{\infty}\frac{\partial F/\partial u}{(u-\omega_r/k)^2+(\omega_i/k)^2}\,du = 0 \tag{2.30b}$$

From the result (2.30), we can at once deduce that any monotonously decreasing distribution ($u\partial F/\partial u \leqslant 0$) is stable.

The result (2.30) can easily be extended to the case of a distribution which is monotonously decreasing in *any* frame of reference. This result is known as Gardner's theorem.

On the stability of isotropic distributions

Of course, the conclusion of the previous section depends on the properties of the *integrated* one-dimensional distribution function. What conclusions can we draw based on the full, three-dimensional distribution?

An often cited result is the stability of any isotropic distribution. The calculations leading to this result are not often carried out, however. We will go through these, since it's a central result, and its development is typical for the calculations done in kinetic stability analysis.

First, we define our distribution as a function of v^2 only:

$$f(\boldsymbol{v}) = \widetilde{f}(v^2)$$

which gives us the following expression for the integrated distribution

$$\begin{aligned} F(u) &= \int f(\boldsymbol{v})\delta\left(u - \frac{\boldsymbol{k}\cdot\boldsymbol{v}}{k}\right) d\boldsymbol{v} \\ &= \int \widetilde{f}(u^2 + v_\perp^2)\, d\boldsymbol{v}_\perp \\ &= 2\pi \int_0^\infty \widetilde{f}(u^2 + r^2) r\, dr \end{aligned}$$

where we've transformed to cylindrical coordinates for the last step. We now proceed to calculate the u-derivative of F

$$\begin{aligned} \frac{\partial F}{\partial u} &= 4\pi u \int_0^\infty \widetilde{f}'(u^2 + r^2) r\, dr \\ &= 2\pi u \int_{u^2}^\infty \widetilde{f}'(x) dx = -2\pi u \widetilde{f}(u^2) \end{aligned}$$

Now, since $\widetilde{f} \geqslant 0$ always, we obtain the desired result:

$$u\partial F/\partial u = -2\pi u^2 \widetilde{f}(u^2) \leqslant 0. \tag{2.31}$$

The result (2.31) makes sense intuitively once we realise that the integration over the perpendicular velocity components carried out in cylindrical coordinates above contains all particles with a perpendicular velocity greater than u^2. These are all the particles *outside* a circle of radius u^2 in $\boldsymbol{v}$-space. The number of particles removed from this integral when moving from u to $u + du$ are expressed by the radius of the circle, $2\pi u^2$, and the density of particles at the circumference, $\widetilde{f}(u^2)$.

As an example of what this looks like for realistic ionospheric electron distribution, we present the calculated distributions used by *Kirkwood et al.* [1995, fig. 7b and 8] in figure 2.3. Although the flux is reduced by more than an order of magnitude in the energy interval between 2 and 4 eV, the one-dimensional distribution is still monotonously decreasing, albeit with an obvious "flattening" in the energy interval of reduced flux.

2.2.4 The electron-ion two-stream instability (cold plasma)

Consider a cold beam of ions drifting through a background of cold electrons with drift velocity $\boldsymbol{V}_0$. The velocity distribution functions are in this case

$$\begin{aligned} f_{i0} &= \delta(\boldsymbol{v} - \boldsymbol{V}_0) \\ f_{e0} &= \delta(\boldsymbol{v}) \end{aligned}$$

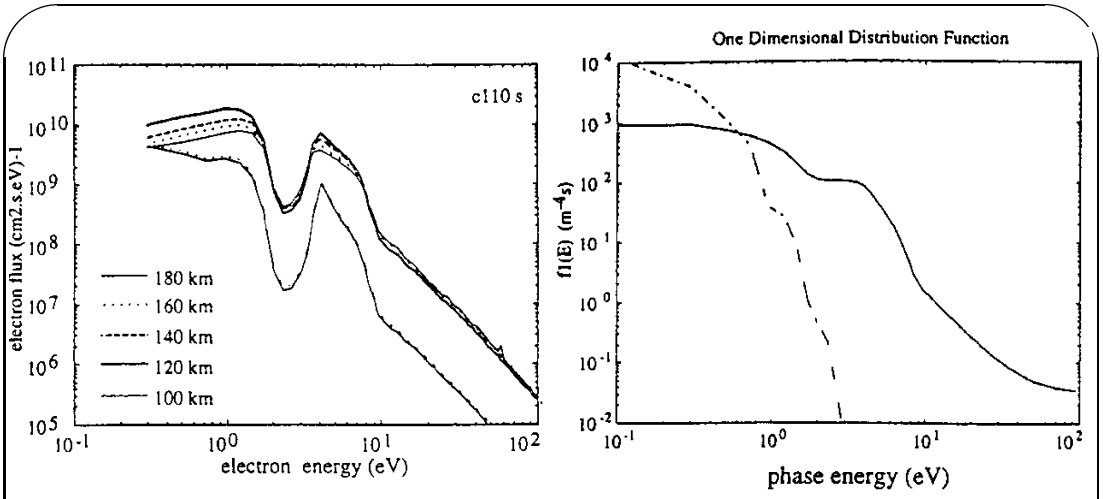

Figure 2.3: The flux-energy spectra of suprathermal electrons used by *Kirkwood et al.* [1995]. The left panel, figure 7b in the original paper, is the one-dimensional upward flux, while the right panel, originally figure 8, is the corresponding one-dimensional distribution for the background (dashed) and suprathermal (solid) populations at 120 km.

inserted in (2.27), this gives

$$1 = \frac{\omega_{pe}^2}{\omega^2} + \frac{\omega_{pi}^2}{(\boldsymbol{k} \cdot \boldsymbol{V}_0 - \omega)^2} \tag{2.32}$$

(note the similarity with (2.11).)

The minimal point for the rhs of this equation is found when $\frac{\partial}{\partial \omega} = 0$, that is

$$-2\frac{\omega_{pe}^2}{\omega^3} - 2\frac{\omega_{pi}^2}{(\boldsymbol{k} \cdot \boldsymbol{V}_0 - \omega)^3} = 0$$

which gives the minimal point

$$\omega_A = \boldsymbol{k} \cdot \boldsymbol{V}_0 \left[\frac{1}{1 + (\omega_{pi}/\omega_{pe})^{2/3}} \right] \tag{2.33}$$

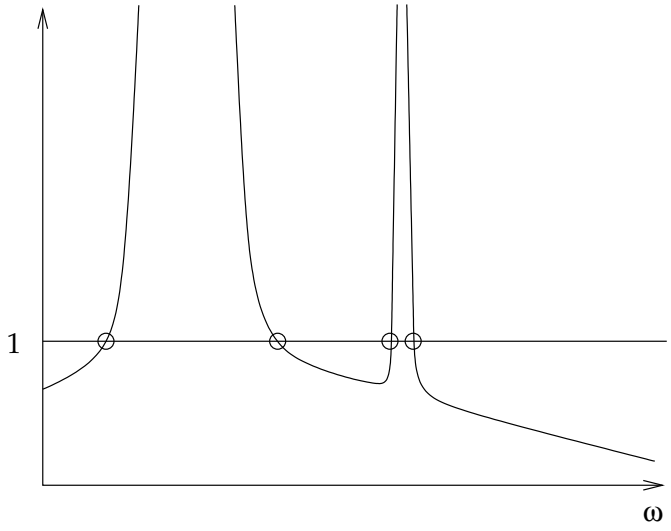

Figure 2.4: The two sides of the dispersion relation for a cold electron-ion beam instability in the kinetic description using cold beams. The figure illustrates a stable configuration.

The condition for instability is that we have complex roots of this equation, i.e. that the minimal point of the rhs is greater than one;

$$1 < \frac{\omega_{pe}^2}{\omega_A^2} + \frac{\omega_{pi}^2}{(\boldsymbol{k}\cdot\boldsymbol{V}_0 - \omega_A)^2}$$

$$(\boldsymbol{k}\cdot\boldsymbol{V}_0)^2 < \omega_{pe}^2\left[1+(\omega_{pi}/\omega_{pe})^{2/3}\right]^2 + \omega_{pi}^2\left(\frac{\omega_{pe}}{\omega_{pi}}\right)^{4/3}\left[1+(\omega_{pi}/\omega_{pe})^{2/3}\right]^2$$

$$|\boldsymbol{k}\cdot\boldsymbol{V}_0| < \omega_{pe}\left[1+(\omega_{pi}/\omega_{pe})^{2/3}\right]^{3/2}$$

The latter expression is now the condition for instability.

A sketch of the two sides of (2.32) for reasonable values of the quantities ω_{pe}, ω_{pi} and $\boldsymbol{k}\cdot\boldsymbol{V}_0$ is given in figure 2.4.

For a warm plasma, the integration of (2.27) is less straightforward. See [e.g. *Krall and Trivelpiece*, 1973].

2.3 The incoherent scattering cross section

In this section we present one of the developments of the incoherent scattering cross section, and we emphasise especially the assumptions of stability and

stationarity, since these are the assumptions invalidated by one of the explanations suggested for the observations described in chapter 4. The expression for the incoherent scattering cross section has been developed by several authors and by many different techniques [e.g. *Dougherty and Farley*, 1960; *Fejer*, 1960; *Salpeter*, 1960; *Hagfors*, 1961; *Rosenbluth and Rostoker*, 1962; *Rostoker*, 1964; *Trulsen and Bjørnå*, 1977]. The fact that all these authors have arrived at the same result by such different methods makes it all the more reasonable that the result is valid under a wide range of conditions. Below, we investigate the limits as defined by a particular development.

We use the presentation by *Trulsen and Bjørnå* [1977] using the principle of dressed test particles originally used for these calculations by *Rosenbluth and Rostoker* [1962], but we have used a different formulation of the Laplace transform. In this presentation, the Laplace transform uses $i\omega$ instead of p, so that the frequency appears more visibly in the results. We give a reasonably detailed presentation of the calculations leading to the expression for the cross section, and we try to look into the consequences of the assumptions of stability and stationarity for our experiment.

As the results presented here are based on linear Vlasov theory, the limitations of that theory also applies to the results in this section. An analysis including nonlinear effects is beyond the scope of this thesis.

Starting from the scattering from a single electron submerged in an external electromagnetic field, the power spectrum per unit frequency of the scattered signal from a plasma volume V per unit infalling power flux has been developed by e.g. *Hagfors* [1977], and this spectrum is given in terms of the ensemble average of the absolute square of the Fourier transformed macroscopic electron density, $N(\boldsymbol{k}, \omega)$. Transforming to macroscopic electron density in space and time, $N(\boldsymbol{r}, t)$, we find the starting point of our discussion, the differential scattering cross section expressing the energy scattered by the plasma per unit volume, per unit angular frequency, per unit solid angle and per unit infalling energy flux. We denote the polarisation of the infalling radiation by $\boldsymbol{p}$, the unit vector from the scattering volume to the receiver by $\boldsymbol{n}$, and the expression becomes

$$\begin{aligned}\frac{d^2\sigma}{d\Omega\, d\omega} = r_0^2 \left|\boldsymbol{n} \times (\boldsymbol{n} \times \boldsymbol{p})\right|^2 \int \left\langle N(\boldsymbol{r} + \boldsymbol{\xi}, t + \tau) \cdot N(\boldsymbol{r}, t) \right\rangle \\ \cdot \exp\left\{i(\omega\tau - \boldsymbol{k} \cdot \boldsymbol{\xi})\right\} d\boldsymbol{\xi}\, \frac{d\tau}{2\pi}.\end{aligned} \tag{2.34}$$

where $\boldsymbol{r}_0$ is the classical electron radius and $\langle\ \rangle$ denote ensemble average.

In this result we have implicitly assumed a homogenous plasma by using the spatial displacement $\boldsymbol{\xi} = \boldsymbol{r}' - \boldsymbol{r}$ between the two points being averaged in the

ensemble average of electron density. In the same way, stationarity has been assumed as we write $\tau = t' - t$. We then integrate over all possible displacements and time shifts.

In the above equation, $\omega = \omega_s - \omega_0$ is the frequency shift in the scattered signal relative to the transmitted frequency, while $\boldsymbol{k} = \boldsymbol{k}_s - \boldsymbol{k}_0$ is the wavevector shift.

The homogeneity assumption is not very restrictive, as it will only influence the reliability of the data across the volume "seen" by the transmitted radar pulse. Homogeneity is therefore only assumed within the scale height (range) resolution of the experiment, and this will not be a problem in well-designed experiments unless extreme situations should arise. (Note that this is not the case for the lower altitudes of the experiment examined in chapters 3 and 4 of this thesis. There, the pulse length is longer than the scale height, leading to ambiguities that cannot be resolved with a standard gated analysis technique.)

The stationarity assumption made here is not very restrictive either. The observed plasma is assumed to be stationary, but this is on the timescale of a single pulse from the transmitter.

Since we don't have any way of assembling an ensemble of ionosphere/radar systems, we can only relate any theoretical expressions we arrive at to measurements by assuming the plasma to be stationary for long enough that we can add a sufficient number of independent observations of identical plasma states. This means that even though the individual observation (pulse) only needs stationarity on the order of the pulse length, the integrated (average) observation (which is what we can compare to theory) requires the plasma to be stationary throughout the integration period.

We express this scattering cross section in terms of the *spectral density* $S(\boldsymbol{k}, \omega)$

$$\begin{aligned} \frac{d^2\sigma}{d\Omega\, d\omega} &= r_0^2 \left| \boldsymbol{n} \times (\boldsymbol{n} \times \boldsymbol{p}) \right|^2 n_e \cdot S(\boldsymbol{k}, \omega) \\ S(\boldsymbol{k}, \omega) &= \frac{1}{n_e} \int d\boldsymbol{\xi}\, \frac{d\tau}{2\pi} \left\langle N(\boldsymbol{r} + \boldsymbol{\xi}, t + \tau) \cdot N(\boldsymbol{r}, t) \right\rangle \cdot e^{i(\omega\tau - \boldsymbol{k}\cdot\boldsymbol{\xi})} \end{aligned} \tag{2.35}$$

In the expression (2.35) above, we need the ensemble average of the product of the microscopic electron density evaluated at different positions and different times. Estimating this average requires knowledge of the two-particle distribution function. *Gordon* [1958] assumed the electrons to be statistically independent scatterers, i.e. that the two-particle distribution function could be expressed as a product of two one-particle distribution functions. With this assumption, the power spectral density becomes

$$S(\boldsymbol{k}, \omega) = \frac{1}{k} F\left(\frac{\omega}{k}\right). \tag{2.36}$$

In other words, the scattered spectrum is proportional to the electron velocity distribution. This spectrum has a width of the electron thermal velocity and the total intensity is proportional to the electron density. As it turns out, this assumption does not hold in the limit $\alpha^2 \ll 1$, where $\alpha^2 = k^2\lambda_D^2$. We will return to this briefly after calculating a closer approximation.

In order to perform the average in (2.35) without investigating the explicit form of two-particle distribution functions, we use the concept of *dressed test particles* [*Rosenbluth and Rostoker*, 1962; *Rostoker*, 1964].

2.3.1 Dressed test particles

Poisson's equation gives us the perturbation in the electrostatic potential due to a test particle with charge q following the straight line orbit $\boldsymbol{r}_0 + \boldsymbol{v}_0 t$:

$$\nabla^2\Phi(\boldsymbol{r}, t) = -\frac{q}{\varepsilon_0}\delta(\boldsymbol{r} - \boldsymbol{r}_0 - \boldsymbol{v}_0 t) - \sum_\alpha \frac{q_\alpha}{\varepsilon_0} n_{1\alpha}(\boldsymbol{r}, t)$$

where the first term is the potential of the test particle itself, while the second term is the charge shielding of all the particle species in the plasma. Fourier transforming this equation yields

$$-k^2\Phi(\boldsymbol{k}, t) = -\frac{q}{\varepsilon_0}\exp\{-i\boldsymbol{k}\cdot(\boldsymbol{r}_0 + \boldsymbol{v}_0 t)\} - \sum_\alpha \frac{q_\alpha}{\varepsilon_0} n_{1\alpha}(\boldsymbol{k}, t)$$

which we Laplace transform, assuming $n_{1\alpha}(t = 0) = 0$,

$$-k^2\Phi(\boldsymbol{k}, \omega) = -\frac{q}{\varepsilon_0} e^{i\boldsymbol{k}\cdot\boldsymbol{r}_0} \int_0^\infty e^{-i\boldsymbol{k}\cdot\boldsymbol{v}_0 t} e^{i\omega t}\, dt - \sum_\alpha \frac{q_\alpha}{\varepsilon_0} n_{1\alpha}(\boldsymbol{k}, \omega)$$

obtaining

$$\Phi(\boldsymbol{k}, \omega) = \frac{1}{k^2\varepsilon_0}\left[\frac{iq\exp\{-i\boldsymbol{k}\cdot\boldsymbol{r}_0\}}{\omega - \boldsymbol{k}\cdot\boldsymbol{v}_0} + \sum_\alpha q_\alpha n_{1\alpha}(\boldsymbol{k}, \omega)\right] \tag{2.37}$$

Substituting the linearised and velocity integrated Vlasov equation, (2.21) with the added assumption $f_{1\alpha}(t = 0) = 0$, in the last equation, the expression becomes

$$\Phi(\boldsymbol{k}, \omega) = -\sum_\alpha \chi_\alpha(\boldsymbol{k}, \omega)\Phi(\boldsymbol{k}, \omega) + \frac{iq}{k^2\varepsilon_0}\frac{\exp\{-i\boldsymbol{k}\cdot\boldsymbol{r}_0\}}{\omega - \boldsymbol{k}\cdot\boldsymbol{v}_0}$$

Isolating Φ, we obtain

$$\Phi(\boldsymbol{k}, \omega) = \frac{iq}{\epsilon(\boldsymbol{k}, \omega)k^2\varepsilon_0}\frac{\exp\{-i\boldsymbol{k}\cdot\boldsymbol{r}_0\}}{\omega - \boldsymbol{k}\cdot\boldsymbol{v}_0}$$

with ϵ defined by (2.24). We insert the last expression back into (2.21). This gives us

$$n_{1\alpha}(\boldsymbol{k},\omega) = -\frac{iq}{q_\alpha}\frac{\chi_\alpha(\boldsymbol{k},\omega)}{\epsilon(\boldsymbol{k},\omega)}\frac{\exp\{-i\boldsymbol{k}\cdot\boldsymbol{r}_0\}}{\omega-\boldsymbol{k}\cdot\boldsymbol{v}_0} \tag{2.38}$$

The inverse Laplace transform is defined by

$$\begin{aligned} n_{1\alpha}(\boldsymbol{k},t) &= \frac{1}{2\pi}\int_L n_{1\alpha}(\boldsymbol{k},\omega)e^{-i\omega t}d\omega \\ &= -\frac{iq}{2\pi q_\alpha}\int_L \frac{\chi_\alpha(\boldsymbol{k},\omega)}{\epsilon(\boldsymbol{k},\omega)}\frac{\exp\{-i\boldsymbol{k}\cdot\boldsymbol{r}_0\}}{\omega-\boldsymbol{k}\cdot\boldsymbol{v}_0}\,e^{-i\omega t}\,d\omega \end{aligned}$$

To evaluate the last integral, we deform the integration contour according to the Landau prescription discussed in section 2.2.3. Hence, the integrals in the susceptibilities χ_α and ϵ must be taken along the Landau contour. With this integration contour, the integral becomes

$$\begin{aligned} n_{1\alpha}(\boldsymbol{k},t) &= \frac{q}{q_\alpha}e^{-i\boldsymbol{k}\cdot\boldsymbol{r}_0}\sum_j \mathrm{Res}\left(\frac{\chi_\alpha}{\epsilon}\frac{\exp\{-i\omega t\}}{\omega-\boldsymbol{k}\cdot\boldsymbol{v}_0};\ \omega=\omega_j\right) \\ &= \frac{q}{q_\alpha}e^{-i\boldsymbol{k}\cdot\boldsymbol{r}_0}\left[\frac{\chi(\boldsymbol{k},\boldsymbol{k}\cdot\boldsymbol{v}_0)}{\epsilon(\boldsymbol{k},\boldsymbol{k}\cdot\boldsymbol{v}_0)}e^{-i\boldsymbol{k}\cdot\boldsymbol{v}_0 t}+\sum_j\frac{\chi_\alpha(\boldsymbol{k},\omega_j)}{\partial\epsilon/\partial\omega|_{\omega_j}}\frac{\exp\{-i\omega_j t\}}{\omega_j-\boldsymbol{k}\cdot\boldsymbol{v}_0}\right] \end{aligned}$$

i.e. the sum over the residues of all the poles of the integrand. In a stable plasma, all the poles from the zeroes of ϵ, the normal modes of the plasma, are damped, so after some time, only the pole at $\omega = \boldsymbol{k}\cdot\boldsymbol{v}_0$ needs to be taken into account. The result is

$$n_{1\alpha}(\boldsymbol{k},t) = \frac{q}{q_\alpha}\frac{\chi_\alpha(\boldsymbol{k},\boldsymbol{k}\cdot\boldsymbol{v}_0)}{\epsilon(\boldsymbol{k},\boldsymbol{k}\cdot\boldsymbol{v}_0)}\exp\left\{-i\boldsymbol{k}\cdot(\boldsymbol{r}_0+\boldsymbol{v}_0 t)\right\} \tag{2.39}$$

where we recognise $\boldsymbol{r}_0 + \boldsymbol{v}_0 t$ as the position of the test particle at time t. This expression gives us the perturbation in the density of particle species α caused by a test particle of charge q. We are now ready to calculate the perturbation in the *electron* density due to a test particle of species α with velocity $\boldsymbol{v}_1$ in position $\boldsymbol{r}_1$ at time t:

$$n^\alpha_{1e}(\boldsymbol{r}_1,\boldsymbol{v}_1,\boldsymbol{r},t) = \int\frac{d\boldsymbol{k}}{(2\pi)^3}\frac{q_\alpha}{e}\frac{\chi_e(\boldsymbol{k},\boldsymbol{k}\cdot\boldsymbol{v}_1)}{\epsilon(\boldsymbol{k},\boldsymbol{k}\cdot\boldsymbol{v}_1)}\exp\left\{i\boldsymbol{k}\cdot(\boldsymbol{r}-\boldsymbol{r}_1)\right\}$$

with the dressed test particle contribution to the electron density now expressed as

$$\widehat{n}_\alpha(\boldsymbol{r}_1,\boldsymbol{v}_1,\boldsymbol{r},t) = \delta_{e,\alpha}\delta(\boldsymbol{r}-\boldsymbol{r}_1) + n^\alpha_{1e}(\boldsymbol{r}_1,\boldsymbol{v}_1,\boldsymbol{r},t)$$

where $\delta_{e,\alpha}$ is one for electrons and zero otherwise. This reflects the fact that a test particle contributes to the electron density directly if it happens to be an electron.

On the other hand, if our plasma is only marginally stable, i.e. one or more of the wave modes of the plasma has zero damping, we expect the result (2.39) to have an additional term for each marginally stable mode. This introduces terms without the convenient $\exp\{i\boldsymbol{k}\cdot\boldsymbol{r}\}$ dependency that turns the $\boldsymbol{r}$-integrations below into $\delta(\boldsymbol{k}'-\boldsymbol{k})$, making the resulting expressions as straightforward as they appear.

In an unstable plasma, i.e. at least one normal mode is growing, the pole from this mode will dominate the result (2.39). Similarly to the marginally stable case, this cannot be integrated analytically. Since the calculated expression is an ensemble average, which we can only compare to a sum of several individual measurements under similar conditions and an unstable plasma will not have a stationary state, the above calculation cannot be applied to predict the scattering from an unstable plasma.

2.3.2 The test particle principle

The test particle principle tells us that we can express the ensemble average of the electron density as

$$\begin{aligned}\langle N(\boldsymbol{r}+\boldsymbol{\xi},t+\tau)\cdot N(\boldsymbol{r},t)\rangle &= n_e^2 \\ &+\sum_\alpha n_\alpha\int d\boldsymbol{r}_1\,d\boldsymbol{v}_1 f_{0\alpha}(\boldsymbol{v}_1)\widehat{n}_\alpha(\boldsymbol{r}_1+\boldsymbol{v}_1\tau,\boldsymbol{v}_1,\boldsymbol{r}+\xi,t+\tau)\cdot\widehat{n}^*_\alpha(\boldsymbol{r}_1,\boldsymbol{v}_1,\boldsymbol{r},t)\end{aligned} \tag{2.40}$$

where the n_e^2 term is the contribution from the uncorrelated electrons and the summation in the other term is over all particle species present in the plasma, since electrons will try to shield them all.

The integration in (2.40) becomes

$$\begin{aligned}\int d\boldsymbol{r}_1\,d\boldsymbol{v}_1 f_{0\alpha}(\boldsymbol{v}_1)\int\frac{d\boldsymbol{k}}{(2\pi)^3}\left[\delta_{e,\alpha}+\frac{q_\alpha}{e}\frac{\chi_e(\boldsymbol{k},\boldsymbol{k}\cdot\boldsymbol{v}_1)}{\epsilon(\boldsymbol{k},\boldsymbol{k}\cdot\boldsymbol{v}_1)}\right]e^{i\boldsymbol{k}\cdot(\boldsymbol{r}+\boldsymbol{\xi}-\boldsymbol{r}_1-\boldsymbol{v}_1\tau)}\\ \int\frac{d\boldsymbol{k}'}{(2\pi)^3}\left[\delta_{e,\alpha}+\frac{q_\alpha}{e}\frac{\chi_e(\boldsymbol{k}',\boldsymbol{k}'\cdot\boldsymbol{v}_1)}{\epsilon(\boldsymbol{k}',\boldsymbol{k}'\cdot\boldsymbol{v}_1)}\right]^* e^{-i\boldsymbol{k}'\cdot(\boldsymbol{r}-\boldsymbol{r}_1)}.\end{aligned}$$

Collecting the $\boldsymbol{r}_1$ terms and performing the $\boldsymbol{r}_1$ integration, obtaining $\delta(\boldsymbol{k}'-\boldsymbol{k})$ this becomes

$$\int d\boldsymbol{v}\frac{d\boldsymbol{k}}{(2\pi)^3}f_{0\alpha}(\boldsymbol{v})\left|\delta_{e,\alpha}+\frac{q_\alpha}{e}\frac{\chi_e(\boldsymbol{k},\boldsymbol{k}\cdot\boldsymbol{v})}{\epsilon(\boldsymbol{k},\boldsymbol{k}\cdot\boldsymbol{v})}\right|^2 e^{i\boldsymbol{k}\cdot(\xi-\boldsymbol{v}\tau)}$$

Recalling the integrations in (2.35) — once again ω and $\boldsymbol{k}$ are the frequency and wave vector shifts —

$$\int d\boldsymbol{\xi}\frac{d\tau}{2\pi}\int d\boldsymbol{v}\frac{d\boldsymbol{k}'}{(2\pi)^3}f_{0\alpha}(\boldsymbol{v})\left|\delta_{e,\alpha}+\frac{q_\alpha}{e}\frac{\chi_e(\boldsymbol{k}',\boldsymbol{k}'\cdot\boldsymbol{v})}{\epsilon(\boldsymbol{k}',\boldsymbol{k}'\cdot\boldsymbol{v})}\right|^2 e^{i\boldsymbol{k}'\cdot(\boldsymbol{\xi}-\boldsymbol{v}\tau)}e^{i(\omega\tau-\boldsymbol{k}\cdot\boldsymbol{\xi})}$$

which we integrate over $\boldsymbol{k}'$ and then τ, obtaining

$$n_\alpha\int d\boldsymbol{v}\left|\delta_{e,\alpha}+\frac{q_\alpha}{e}\frac{\chi_e(\boldsymbol{k},\boldsymbol{k}\cdot\boldsymbol{v})}{\epsilon(\boldsymbol{k},\boldsymbol{k}\cdot\boldsymbol{v})}\right|^2 f_{0\alpha}(\boldsymbol{v})\delta(\omega-\boldsymbol{k}\cdot\boldsymbol{v})$$

Defining $z_\alpha = q_\alpha/e$, the power spectral density thus becomes

$$\begin{aligned}S(\boldsymbol{k},\omega) = &\left|1-\frac{\chi_e}{\epsilon}\right|^2\int d\boldsymbol{v}f_{0e}(\boldsymbol{v})\delta(\omega-\boldsymbol{k}\cdot\boldsymbol{v})\\ &+\left|\frac{\chi_e}{\epsilon}\right|^2\sum_\alpha\frac{n_\alpha}{n_e}z_\alpha^2\int d\boldsymbol{v}f_{0\alpha}(\boldsymbol{v})\delta(\omega-\boldsymbol{k}\cdot\boldsymbol{v})\end{aligned} \tag{2.41}$$

where $\epsilon = 1+\chi_e+\sum_\alpha\chi_\alpha$ is the plasma dielectric function and χ_e and χ_α are the electron and ion susceptibilities.

When calculating the incoherent scattering from a plasma where the electrons are described by a kappa-distribution, we need to calculate the electron susceptibility, χ_e, using the modified plasma dispersion function, Z^*_κ, where Z is ordinarily used. The dielectric function will contain Maxwellian-like terms from the ion species and a kappa-like term from the electrons.

As pointed out several times in the presentation, the equation (2.41) depends on the plasma being stable, uniform and stationary. *Weinstock* [1967] has explored the scattering cross section for nonstationary and inhomogenous plasmas by separating the scattering into "coherent" and "incoherent" parts, corresponding to scattering from correlated and uncorrelated electrons in our presentation. The discussion is somewhat slanted towards laboratory situations, and the results are (in particular) discussed for inhomogenous and exponentially decaying plasmas (predicting a broadening of the scattered spectrum in both cases), while for growing (unstable) plasmas, he simply notes that "The incoherent scatter becomes complicated". He is optimistic about using incoherent scattering to examine turbulent plasmas, since the quantity $\langle N_e N_e\rangle$ which appears so prominently in (2.35) is a fundamental quantity in the theory of plasma turbulence.

We will discuss the result (2.41) in the two limits $\alpha^2 \gg 1$ and $\alpha^2 \ll 1$.

$\alpha^2 \gg 1$ In this limit, the susceptibilities χ_α become small ($\ll 1$). The dielectric function ϵ approaches unity, and the scattering cross section is approximately

$$S(\boldsymbol{k}, \omega) \approx \int d\boldsymbol{v} f_{0e}(\boldsymbol{v}) \delta(\omega - \boldsymbol{k} \cdot \boldsymbol{v}).$$

This is the same result as obtained by assuming statistically independent scatterers. This result has a simple physical interpretation. The wavelength of the infalling radiation is very short, much shorter than the Debye length of the plasma. The number of particles available for shielding a particle is therefore small, and the shielding effects become unimportant. The particles are uncorrelated at these wavelengths.

$\alpha^2 \ll 1$ In this limit, the susceptibilities are not necessarily small. The significant contributions to the scattering are now where the dielectric function of the plasma vanishes, i.e. the normal modes of the plasma. The scattering is further modified by the distribution function of the various particle species at velocities matching the phase velocities of the different modes. In a broad sense, the central part of the spectrum, the ion spectrum, has a width comparable to the thermal velocity of the dominant ion species. The plasma line occurs at the Langmuir frequency, and its width is determined by the Landau damping of this mode.

2.3.3 Extensions of the theory

Several authors have examined the effects on the incoherent scattering cross section under other physical conditions. *Farley et al.* [1961] extended the calculations of [*Dougherty and Farley*, 1960] to cover the case of a uniform magnetic field, *Dougherty and Farley* [1963] extended the calculations to a theory for incoherent scattering from a partly ionised gas, and *Farley* [1966] incorporated the effect of unequal electron and ion temperatures. *Fejer* [1961] also examined the effect of a uniform magnetic field, *Salpeter* [1963] examined the density fluctuations in a nonequilibrium plasma, and *Hagfors and Brockelman* [1971] examined the density flucutations in a collision dominated plasma.

2.4 Enhancement mechanisms for plasma lines

Plasma lines have been observed in several of the world's incoherent scatter facilities. Even so, the observation of plasma lines is not part of the regular observation schedule in any of these facilites. For instance, none of the common programmes run at EISCAT include observation of plasma lines. The interpretation of plasma line data is also far from being fully understood.

As we saw in the previous section, the incoherent scattering mechanism gives very weak signal returns. Observing even the ion spectrum requires powerful transmitters, big antennas, sensitive receivers and low-noise electronics.

Thermal plasma lines are each a factor $\frac{1}{2}\alpha^2$ weaker than the ion spectrum, weak enough that their observation was long thought impossible. It has turned out that there are several mechanisms that enhance the power scattered at the Langmuir frequency up to several orders of magnitude over the thermal level.

Enhancement mechanisms described in the literature include suprathermal electrons, first suggested by *Perkins and Salpeter* [1965]; precipitating protons [*Bjørnå et al.*, 1982]; reduced Landau damping of Langmuir waves due to depletion of suprathermal particles at particular energies [*Kirkwood et al.*, 1995]; a turbulence layer [*Mishin and Schlegel*, 1994]. Below, we give a short review of some of these enhancement mechanisms. A common, and unfortunate, feature of these studies is their focus on plasma lines only. It is well known that even moderate beams of ions can severely deform the incoherent scattering spectrum, and if the effects producing the plasma line enhancement can be expected to influence the ion spectrum, the ion spectrum should be examined, as it could help distinguish between different enhancement models. (Conversely, studies of strong, asymmetric or otherwise strange ion spectra rarely, if ever, discuss what effects the mechanisms suggested could have on plasma lines.) This omission can help explain why plasma line observations are not made on a regular basis.

Although weak (even when enhanced), plasma lines have interesting applications in diagnosing the ionospheric plasma. Probably the first application of plasma lines was to measure suprathermal electron fluxes [*Perkins and Salpeter*, 1965; *Perkins et al.*, 1965]. The intensity of the plasma line is proportional to the logarithmic derivative of the electron velocity distribution at the phase velocity of the plasma wave seen by the radar. One point of the distribution can therefore be determined at every height examined. Through some assumptions regarding the shape of the distribution, a more complete picture could be obtained [*Yngvesson and Perkins*, 1968]. A review of the different methods and comparison with measurements is given by *Cicerone* [1974]. As pointed out by *Carlson et al.* [1977], these methods, through their assumptions, introduce potentially significant uncertainties, and that better understanding of heat transfer is necessary. The effect of heat flow on plasma line frequency was examined by *Kofman et al.* [1993]; *Mishin and Hagfors* [1994], and later by *Guio et al.* [1996].

Most plasma line studies are concerned with *F*-region plasma lines, particularly near the peak of the *F* layer. Plasma lines are more easily observed at such altitudes, due to lower collisional damping and higher suprathermal fluxes.

Indeed, *Heinselman and Vickrey* [1992] uses the shape of the plasma line spectrum to determine the *F* layer peak altitude with greater accuracy than possible through other diagnostics. Observations of *E* region plasma lines were made at Chatanika [*Wickwar*, 1978; *Kofman and Wickwar*, 1980] and *Oran et al.* [1981] compared the theory with these observations. *Valladares et al.* [1988] made *E*-region plasma line observations with the same radar after its relocation to Søndre Strømfjord.

Plasma lines have very well defined frequency; their spectral width can be as small as some kHz; and thus their offsets can be determined very accurately. The offset of one line can be used for calibrating the electron density measurements of the ion spectrum, as in the present study. Plasma line measurements have also been used together with the ion spectrum data to determine ion composition by *Bjørnå and Kirkwood* [1986], using data from the quiet periods of the same experiment examined in this thesis. Using a similar analysis technique, *Bjørnå* [1989*a*] determined the ion-neutral collision frequency in the *E*-region. When monitoring up- and downshifted plasma lines simultaneously, the differences in the offsets of the two lines can tell us something about bulk motion of the electrons, [*Hagfors et al.*, 1984]; with bistatic measurements, we can determine electron temperature [*Hagfors and Lehtinen*, 1981]; or heat flow [*Kofman et al.*, 1993; *Guio et al.*, 1996]. With two radars at different frequencies (and thus different $\boldsymbol{k}$) observing the same volume, the techniques of *Hagfors and Lehtinen* [1981] could again be applied to measure electron temperature. This was confirmed by *Fredriksen et al.* [1989], who measure electron temperature and density independently of the ion spectrum by plasma line measurements using the EISCAT UHF and VHF radar systems together. Combining this with bistatic measurements might be used to determine electron temperature anisotropy.

The calculation of the enhancement due to a particular mechanism usually consists of a numerical integration of the enhanced scattered spectrum over the width of the plasma line, and a comparison with the power of thermal plasma lines — i.e. the intensity of plasma lines from a Maxwellian background plasma alone. It is customary to present the intensity of the plasma line as a plasma line "temperature", that is, the electron temperature necessary to produce a thermal plasma line of the same intensity. Through the radar equation for the plasma line, the plasma line temperature is defined by

$$T_p^{\text{ant}} Bw = \frac{P_t}{R^2} r_0^2 \sigma_p \frac{c\tau}{2} A(\nu_p), \tag{2.42}$$

where T_p^{ant} is the equivalent noise temperature of the plasma line at the antenna, Bw is the bandwidth of the signal, P_t is transmitted power, R is range,

$c\tau/2$ is the range contributing to the scattering, $A(\nu_p)$ is gain at the plasma line frequency ν_p and σ_p is the scattering cross section of the plasma line, given by

$$\sigma_p = \frac{T_p}{T_e}\frac{1}{2}n_e k^2 \lambda_D^2 \tag{2.43}$$

The enhancement can then be expressed as a ratio of plasma line temperature to electron temperature.

$$I_p = \frac{T_p}{T_e} \tag{2.44}$$

2.4.1 Suprathermal electron enhancement

This mechanism, summarised in [*Bjørnå and Trulsen*, 1986], is essentially an addition of high-energy particles described e.g. by a power-law distribution in the tail of the electron distribution. The power-law distribution is limited to an energy range $E_1 < E < E_2$, which includes the "phase energy" of the Langmuir waves. This enhancement mechanism is the basis for using the intensity of the plasma line for estimating the suprathermal velocity distribution [*Perkins and Salpeter*, 1965; *Yngvesson and Perkins*, 1968; *Cicerone*, 1974].

In the neighbourhood of the Langmuir frequency, the incoherent scattering spectrum can be approximated by [*Perkins and Salpeter*, 1965]

$$S(\omega) = \frac{F_{e0}(v_\phi)/k}{\frac{4}{\omega_{pl}^2}(\omega - \omega_{pl})^2 + \left[\pi(\omega_{pe}/k)^2 \left(\frac{\partial}{\partial v}F_{e0}(v)\right)_{v_\phi}\right]^2} \tag{2.45}$$

where ω and $\boldsymbol{k}$ are the frequency and wave vector shift like before and $v_\phi = \omega/k$ is the phase velocity of the Langmuir wave. Assuming the background to be Maxwellian, this expression can be integrated over the spectral width of the plasma line, giving

$$I_p = \frac{1}{2}\alpha^2 \frac{F_{e0}(v_\phi) + F_{es}(v_\phi)}{F_{e0}(v_\phi) - \frac{v_{\text{th}}^2}{v_\phi}\frac{d}{dv}F_{es}\big|_{v_\phi}} \tag{2.46}$$

By including the effect of collisions, the expression becomes

$$I_p = \frac{1}{2}\alpha^2 \frac{F_{e0}(v_\phi) + F_{es}(v_\phi) + \chi}{F_{e0}(v_\phi) - \frac{v_{\text{th}}^2}{v_\phi}\frac{d}{dv}F_{es}\big|_{v_\phi} + \chi} \tag{2.47}$$

where χ is the collision term

$$\chi = \frac{v_{\text{th}}^2}{v_\phi^4}\frac{\nu_e}{\pi k}$$

and ν_e is the collision frequency between electrons and massive particles (i.e. ions and neutrals).

The terms in the numerator of (2.46) and (2.47) represent the excitation of Langmuir waves by resonant particles, while the denominator terms represent the Landau damping from the same particles. Enhancement arises when the suprathermal particles are dominant in the numerator (i.e. many particles at an energy matching the "phase energy" of the Langmuir wave) while they don't contribute significantly to the damping; i.e. the slope of the suprathermal distribution is small at the phase velocity of the Langmuir wave.

The power law distribution has relatively many particles at high energies, while the slope of the distribution is small, leading to enhancement. Up to 50 times enhancement over thermal level is predicted by this mechanism.

On the EISCAT UHF radar system, using a power-law distribution to model suprathermal electrons for enhancing plasma lines below 7.5 MHz is questionable. See section 2.1.3. It would be interesting to calculate the plasma line enhancement one could expect to obtain using a kappa distribution to model the electrons. This has not been pursued in the present study.

2.4.2 Proton precipitation enhancement

Although precipitating protons, like any ions, do not contribute directly to incoherent scattering, the electron shielding of protons at energies matching the phase velocity of Langmuir waves can enhance incoherent scatter plasma lines above thermal level in a similar way that precipitating electrons do [*Bjørnå et al.*, 1982; *Bjørnå*, 1989*b*]. Furthermore, the secondary electrons produced by proton precipitation can also contribute to the enhancement or damping of these lines.

Plasma line enhancement were calculated for EISCAT VHF and UHF systems, at altitudes of 200 and 500 km, taking secondary electron fluxes into account when appropriate. Enhancement factors up to 75 were calculated for the VHF at 500 km when not taking secondary electrons into account, i.e. for the upshifted plasma line. For the UHF, the enhancements were more modest, 20 times thermal level or less.

2.4.3 Plasma Turbulence Layer

Mishin and Schlegel [1994] reviews the observation of strongly enhanced plasma lines by *Valladares et al.* [1988] and the suprathermal electron precipitation model presented above. They conclude that this model is incapable of explaining the enhancement levels observed by *Valladares et al.* [1988]. In addition to

this model, they propose that an electron beam in the auroral ionosphere triggers ion-acoustic waves in a relatively thin layer called the *plasma turbulence layer*, where long-scale Langmuir waves are converted to short-scale Langmuir waves. There is also an increase in electron temperature within the layer.

2.4.4 Enhancement by reduced Landau damping

The plasma line enhancement mechanism described by *Kirkwood et al.* [1995] is based on the same expression for total plasma line power as for suprathermal electrons, (2.45). In this case, the electron density profile is used as input to a numerical model of the ionosphere which calculates an electron flux [*Lummerzheim and Lilensten*, 1994]. The calculated electron flux, shown in figure 2.3, has a strong minimum at phase energies between 2 and 4 eV, an energy corresponding to a vibrational level in N_2, which then absorbs electrons at these energies. The corresponding one-dimensional distribution has an almost flat shape in the same energy range, cf. equation (2.31). The corresponding minimum in Landau damping at these frequencies lead to strongly enhanced plasma lines.

The authors report observations of plasma lines with temperatures above 5 eV (corresponding to 55000 K) at frequencies between 5 and 7 MHz and at altitudes between 120 and 190 km with a maximum intensity of 20 eV observed at 6.2 MHz offset and at 145 km altitude. The observed intensities are reported to be 200 times above the thermal level.

The corresponding calculations based on the calculated flux, predict intensities up to 15 eV at 6 MHz.

2.5 Explanations for strong and unusual ion spectra

2.5.1 Skewed spectra

Ion spectra of tremendous power and with very asymmetric shapes have been reported by several authors [e.g. *Foster et al.*, 1988; *Collis et al.*, 1991; *Rietveld et al.*, 1991; *Wahlund et al.*, 1992; *Forme*, 1993] and a great statistical survey of over 5000 hours of EISCAT CP data have been performed by *Rietveld et al.* [1996]. Different explanations for these spectra have been suggested, and there seems to be no general consensus yet on their explanations.

- *Foster et al.* [1988] talks about current driven instabilities and *Rietveld et al.* [1991] are on a similar trail, exploring the effects of ion-electron two-stream instabilities on the scattered spectrum. This is the instability we investigated in section 2.2.4.

- *Wahlund et al.* [1992] points out that the currents needed for *Rietveld et al.*'s explanation is an order of magnitude larger than those measured by any other instruments, and suggests that ion-ion drift instability is the correct explanation. The onset of this instability requires a temperature ratio T_e/T_i in excess of 3 and ion drift velocities larger than the thermal velocity of ions. This implies an almost or fully collisionless medium and low neutral density, which puts us well inside the *F* layer, high above the phenomena of the present study.

- *Forme* [1993] explains the spectra through Langmuir wave decay, where streaming low-energy electrons trigger a beam instability which again excites Langmuir waves.

As pointed out by *Rietveld et al.* [1996], none of these theories are presently capable of explaining all the features of the different observations.

2.5.2 Non-thermal ion velocity distributions

It has been established by several authors [e.g. *Schunk and Walker*, 1972; *St.-Maurice and Schunk*, 1974] that ions in crossing $\boldsymbol{E}$- and $\boldsymbol{B}$-fields can develop velocity distributions that are far from Maxwellian, sometimes even toroidal in shape. The effects of such distributions on the standard analysis of incoherent scatter data has been investigated by *Løvhaug* [1985].

The incoherent scatter cross section has been calculated for such distributions [*Venkat Raman et al.*, 1981; *Hubert*, 1984; *Kikuchi et al.*, 1989] and consists of a peak at zero real frequency in addition to the usual ion-acoustic shoulders.

An explanation for this peak at zero frequency was provided by *Buchert and La Hoz* [1996] in terms of an instability at or close to zero frequency.

We have not investigated this model in detail. Because significantly non-thermal ion velocity distributions only occur for low ion-neutral collision frequencies, it can only be applied to *F*-region altitudes. Furthermore, from a brief investigation, the observation of this mode seems to be possible only at significant angles with the magnetic field.

2.5.3 Collapsing Langmuir turbulence

The theory of weak turbulence has been applied to explain the enhancement of plasma lines in artificial ionospheric heating experiments. *Hanssen et al.* [1992] have predicted narrow, single-peaked ion-acoustic spectra in conjunction with strongly enhanced plasma lines for some choice of parameters in this situation.

We are currently pursuing an investigation of whether using an impinging electron beam can excite similar turbulence and produce such strong, narrow spectra in conjunction with strongly enhanced plasma lines. The results will be presented at the EGS assembly in Nice this spring.

A review of the recent results in turbulence theory is given in [*Robinson*, 1997]

Chapter 3

The experiment

3.1 A Technical description

The experiment was run with the EISCAT UHF radar. The properties of the EISCAT radar system is described in [*Folkestad et al.*, 1983]. The experiment was designed and conducted in a campaign to detect the offset of plasma lines in order to improve the analysis of the ion spectrum, especially to deduce the ion composition $[O^+]/n_e$ during the quiet periods rather than using a predefined standard ionosphere. The experiment was run from July 4th, 08:00 UT to July 5th, 08:00 of 1985. The results of that work have previously been published by *Bjørnå and Kirkwood* [1988].

The signals were transmitted from the Tromsø site and received at the sites in Tromsø and in Sodankylä. The transmitted beam was set up to be field-aligned at 210 km altitude. The basic time resolution of the experiment was one minute.

The experiment consisted of two long pulses; one of 210 μs at 936.5 MHz followed by a pulse of 105 μs at 937 MHz with a gap of 10 μs between the pulses. The former is called long pulse 2 (LP2) and was used for ion spectrum ACFs at 14 range gates from 122.8 km to 502.6 km with a gate separation of approximately 30 km. The latter is called long pulse 1 (LP1) and was used for ion spectrum ACFs at 14 range gates from 76.9 km to 266.6 km with a gate separation of approximately 15 km, and for ion spectrum and plasma line power profiles over 80 range gates from 58 km to 235 km with a gate separation of approximately 2.3 km. The pattern was repeated every 8000 μs. The timing diagram for the experiment is given in figure 3.1.

Two of the eight receiver channels in Tromsø were used for the ion spectrum ACFs and power profiles, one for each transmitted frequency. The other six channels were used for plasma line power profiles. Only downshifted

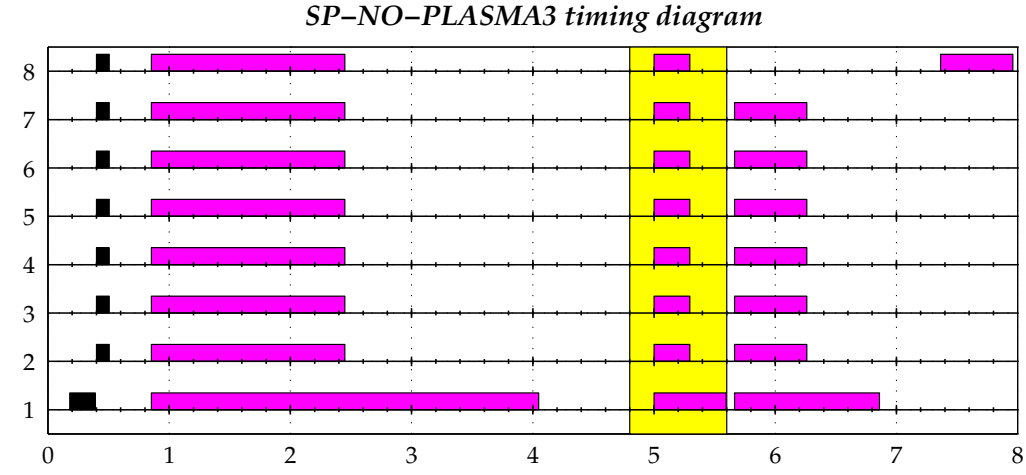

Figure 3.1: Timing diagram for sp-no-plasma3. Channels 1 and 8 are the ion spectra LP2 and LP1, respectively, while channels 2 through 7 are the plasma line power profiles

plasma lines were monitored. The filters had a bandwidth of 100 kHz and were positioned at offsets from −2.5 to −3.0 MHz with regard to the transmited frequency in steps of 0.1 MHz with regard to LP2, and offsets from −3.0 to −3.5 MHz with regard to LP1 for the first ten minute period. Then the entire filter bank was moved down 1 MHz for the next ten minutes, (offsets from −3.5 to −4.5 MHz) and another 1 MHz for another ten minute period before the pattern was repeated. Thus, at any one time, 11 different offsets were monitored, with 31 different offsets monitored in all. The offsets are tabulated in table 3.1.

With two pulses transmitted on frequencies just 500 kHz apart, we will inevitably receive plasma lines from both pulses at different offsets and altitudes. After reception, the problem is then to determine which offset and altitude the received signal corresponds to. Once this has been determined, the offset, range and range corrected power can easily be calculated.

The lowest frequency pulse is transmitted first. As long as the electron density, and hence the Langmuir frequency, increases with height, this means that downshifted plasma line signals from this pulse will be scattered first, causing the plasma lines received from the two pulses to have a greater separation than the delay between transmission of the pulses would indicate. This also means that if the Langmuir frequency should *decrease* with height locally, the two pulses will be received with a *shorter* gap than the delay between the transmission of the two pulses. This effect is illustrated in figure 3.2

All eight receiver channels in Sodankylä were used for power measurements, one for each of the ion spectra (positions 936.5 MHz and 937.0 MHz, 250 kHz

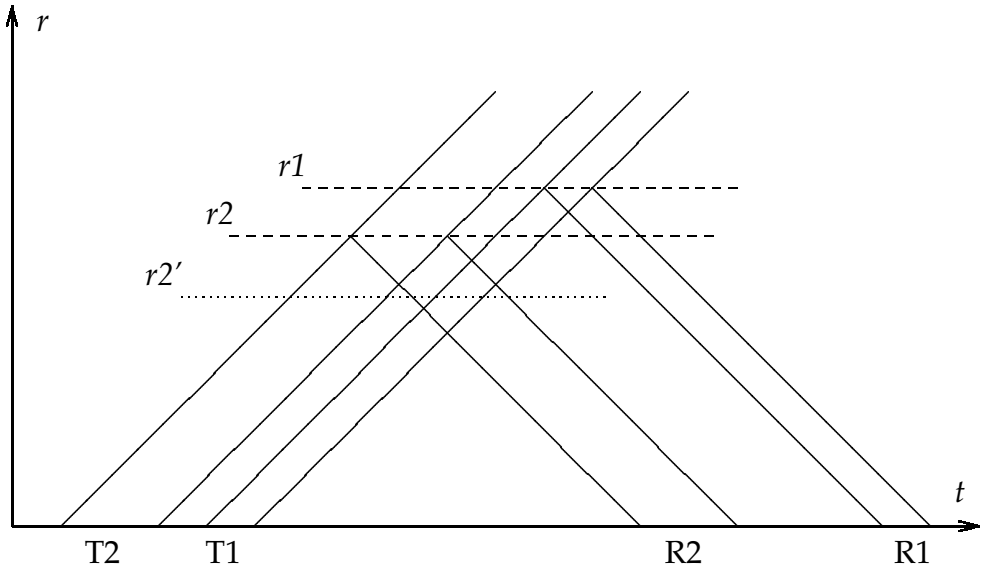

Figure 3.2: A range-time diagram for one of the plasma line channels used in the experiment. The vertical axis is range while time advances along the horizontal axis. T2 and T1 denote the transmission of LP2 and LP1, respectively, and we can see these moving up as time advances. *r2* and *r1* are the ranges at which the local plasma line resonance frequency matches the offset from each of the pulses to the receiver channel in the figure. The signal is received at R2 and R1. Since altitudes are calculated with regard to LP1, the plasma line from *r2* appears at the fictuous range *r2′* which is lower than the actual height. This height difference corresponds to the difference between the center height of the two pulses, in our case this difference is 162.5 μs, or $\approx$ 25 km.

bandwidth), one on each of the offsets -4.2 MHz and -4.4 MHz (against LP1) with a bandwidth of 250 kHz, while the remaining four channels' filters were centered at -3.5 MHz offset (again to LP1) with bandwidths of 250, 125, 500 and 1000 kHz. The antenna was pointing to a common volume in the heights 140.0, 142.0, 144.0, 146.0, 148.0 and 160.0 km, with the pointing changing every five minutes.

The reception scheme was a bit uncommon; 30 different gates sampled at 20 μs for each of the channels, so that we can observe the plasma before, during and after the passing of the pulses. This makes it easy to distinguish returns from each of the pulses, since they are located in completely different gates. It also makes it possible to distinguish signal from noise. It was known that the probability of finding plasma lines at the remote sites was low, so the idea was

	00 – 10 30 – 40	10 – 20 40 – 50	20 – 30 50 – 00
Ch.1	-0.5 0	-0.5 0	-0.5 0
Ch.2	-3.0 -2.5	-4.0 -3.5	-5.0 -4.5
Ch.3	-3.1 -2.6	-4.1 -3.6	-5.1 -4.6
Ch.4	-3.2 -2.7	-4.2 -3.7	-5.2 -4.7
Ch.5	-3.3 -2.8	-4.3 -3.8	-5.3 -4.8
Ch.6	-3.4 -2.9	-4.4 -3.9	-5.4 -4.9
Ch.7	-3.5 -3.0	-4.5 -4.0	-5.5 -5.0
Ch.8	0 0.5	0 0.5	0 0.5

Table 3.1: The reception pattern of the Tromsø site. Each cell contains the offset from LP1 to the center frequency of the filter on top and the offset from LP2 on the bottom. All offsets are in MHz. The offsets of ± 0.5 MHz in channels 1 and 8 will not result in any signal, while channels 2–7 will contain plasma lines from both pulses in the general case.

to use several different settings for the oscillators and see if one could get any signals at all. The center frequencies of the filters were also changed while the experiment was running, again to see whether any plasma lines could be seen.

No plasma lines were observed from Sodankylä for the entire experiment.

3.2 The analysis

The experiment has been analysed using GUISDAP version 1.6, gated analysis. Only the shorter of the two pulses has sufficient range resolution to be used below ≈ 180 km. The correlation time of the *E*-region plasma is longer than this, often of the order of 300 μs. Inspecting the ACFs obtained from this pulse in this region, figure 3.3, we see that we have obtained only the first zero crossing; for the first four gates (76.8 to 120.6 km) not even that. The results of this analysis should therefore not be emphasised, particularly at low altitudes. As

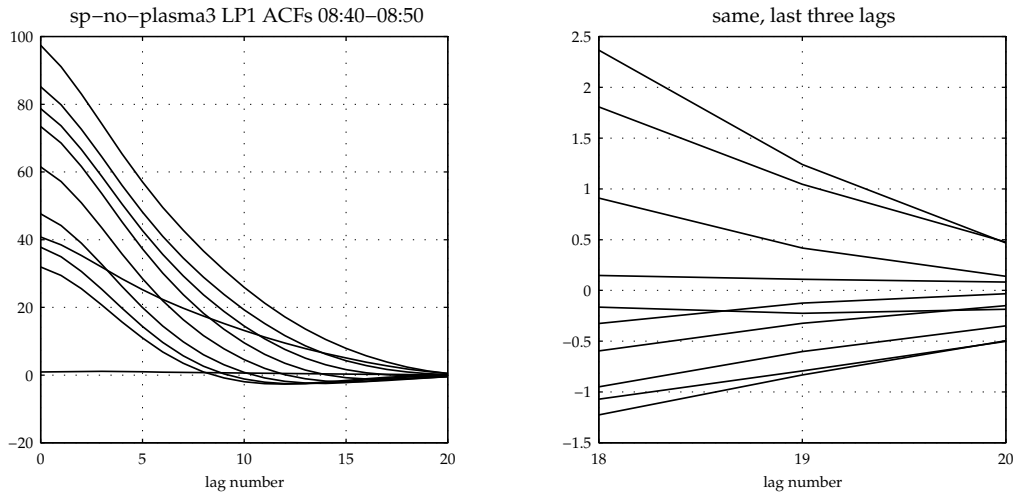

Figure 3.3: ACFs (real part) from the ten first range gates of LP1 (76.8 to 208.2 km) in ten minute integrated data from a quiet period. The left panel has the entire recorded ACFs, while the right panel shows just the last three lags.

In the left panel, the lowermost line, almost zero, is the first range gate, the line cutting diagonally through the figure is the second range gate and the rest of the range gates come in order, lowermost range gates on the top. In the right panel, the ACFs of range gates 3, 2, 4 and 1 (in that order from the top at lag 18) are still positive at the last lag — no zero crossings have been recorded. The ACFs which have one zero crossing are (ordered top down at lag 18) gates 5, 10, 9, 8, 6 and 7.

an example, notice how the electron density given by the analysis (circles) fails to match the electron density calculated from the power profile (solid line) in the upper left hand panel of figure 4.1, except between 150 and 180 km. The small error flags on these points are just based on the quality of the fit made, not on the quality of the parameters obtained.

Above 180 km, the correlation between the two estimates again diverge. Here we suspect that the short pulse has too little power to obtain sufficient signal for analysis. We therefore conclude that the analysis of the longer pulse should be used above 180 km.

3.3 Supporting instruments

For a more complete description of the atmospheric conditions during the experiment, we have produced observations from the following instruments situated close to the EISCAT site in Ramfjordmoen.

- An Ionosonde situated in Ramfjordmoen, 69° 59′ N, 19° 23′ E. This is a wide angle instrument (approx. 60° angle of vision) which can give some indication of electron density distribution throughout the ionosphere (up to approx. 800 km, and can be a useful independent control of EISCAT data. The ionosonde transmits at frequencies from 1 to 12 MHz, and measures the reflected power as a function of time. Due to the slowdown of the radio wave before reflection, the time is not exactly proportional to the distance to the reflecting layer. The distance calculated without correcting for this effect is called *virtual height* and is slightly higher than the actual height. An entire scan takes between 2 and 2 1/2 minutes.

  Ionosonde measurements have been made every 20 minutes throughout the duration of the experiment. Ionograms from quiet and disturbed conditions are reproduced in figure 3.4

- A riometer situated in Lavangsdalen, 69° 24′ N, 19° 18′ E. This is an instrument monitoring radiation from space at 32.0 MHz. Here we can observe the diurnal variation of incoming radiation, and, superimposed on this, absorption due to enhanced ionization in the lower ionosphere caused by 'hard' particle (> 10 keV) precipitation.

  The riometer also makes continuous measurements, and we have data from the duration of the experiment, apart from the period from 12:00 and 12:30 UT, where the instrument is being calibrated. In figure 3.5, the data from 12:30 UT to midnight 1985/07/04 is plotted.

3.4 A short résumé of the results

In this section we will summarise the entire 24 hours of the experiment. This is done for the overview, for a detailed description of the interesting events, see chapter 4. It might be helpful to refer to the colour plates during this presentation.

The ion spectrum shows us a reasonably normal day. From the start of the experiment until about 12:30, we have quiet conditions with a photoionised E

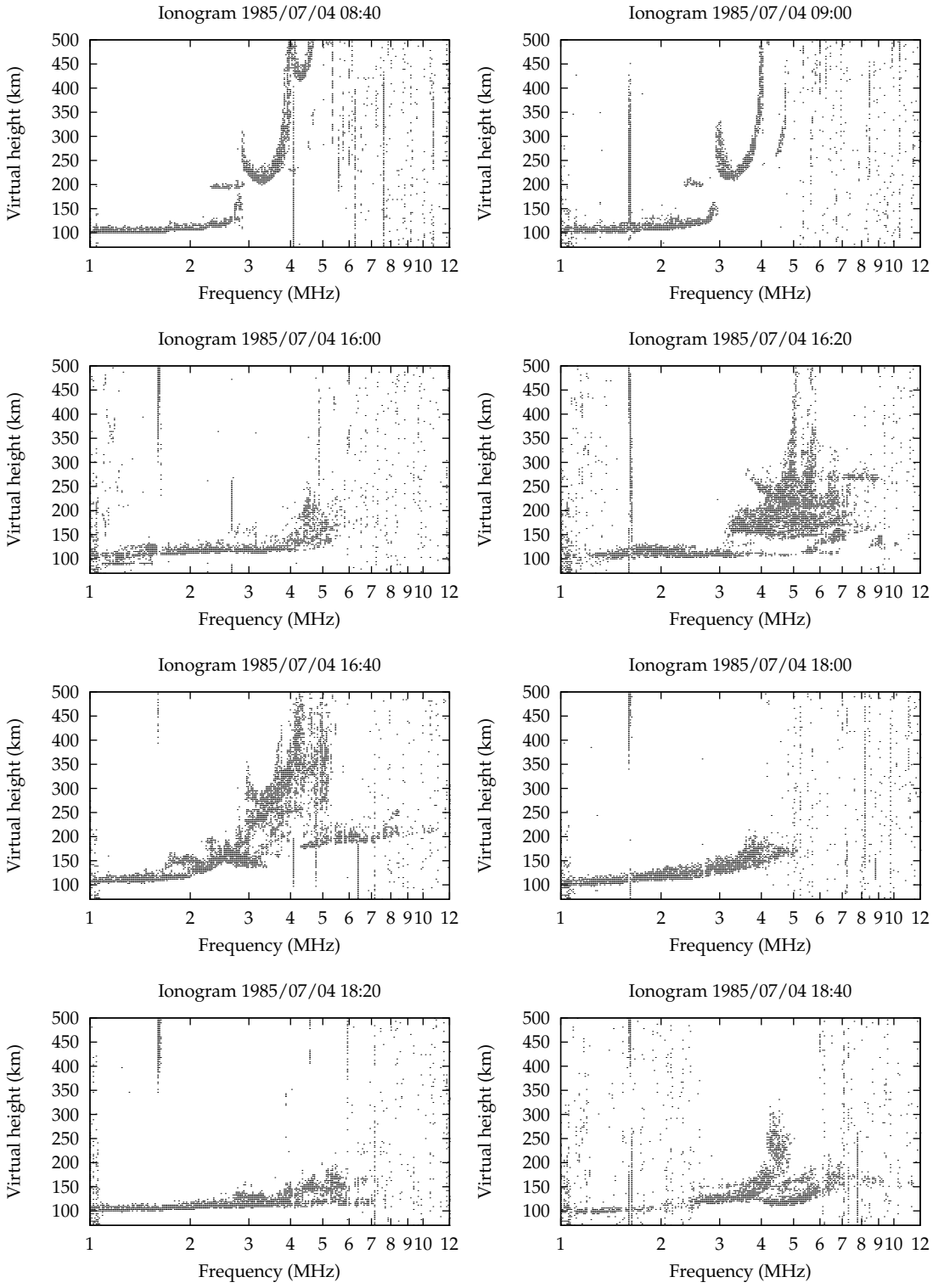

Figure 3.4: Some ionograms from the day of the experiment. Quiet-time ionograms are in the two uppermost panels, and three ionograms from around the time of the events are in the next six panels.

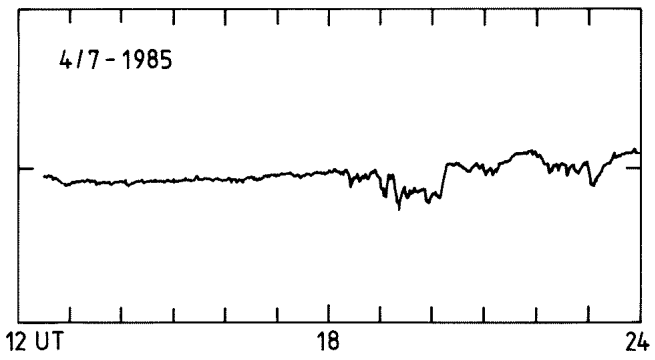

Figure 3.5: Riometer data from the day of the experiment 12:30 – midnight. The riometer measures influx of cosmic radiation at 32 MHz, a radiation which is absorbed by ionisation in the lower ionosphere, which is caused by energetic particle precipitation. Negative spikes in this figure is therefore an indication of high-energy particles entering the ionosphere.

layer at approximately 125 km, and plasma line echoes in all the channels in Tromsø with a reasonable intensity and range distribution.

At 12:45 we have an influx of 'soft' particles, indicated by an increased electron density in the E layer, and subsequent heating of the ions and then the electrons from the bottom of the E layer up to the topside. We also see an outflow of ions in the F layers (200–400 km) at about the same time. We observe a moderate intensification of the plasma lines with offsets of -5.0 and -5.1 MHz at 110–140 km during this event. This situation persists until about 14:15 UT.

We then have another quiet period, followed by another period of soft precipitation from 15:30 to 16:20 UT with enhanced plasma lines at -4.0 MHz at altitudes of 120–140 km. These can be seen in channels 2 and 7, being returns from LP1 and LP2, respectively. The apparent difference in altitude is due to the phenomenon illustrated in figure 3.2.

The precipitation seems to change abruptly from soft to hard particles in the integration periods initiated at 16:21 and 16:22. We have enhanced scattering which penetrates to below 100 km, indicating particle energies on the order of ~ 10 keV. In these two minutes, the peak received power (raw electron density) is increased by a factor of between 6 and 9, while the altitude of strongest scattering is lowered to an altitude of less than 100 km. The scattering then relaxes to more ordinary values and altitudes over a period of 6–7 minutes. Simultaneously, in the plasma line channels, we see strongly enhanced returns from *all* of the plasma line channels and in altitudes ranging from 100 to 175 km

during the 10 min period in which the plasma line channels are monitoring offsets from -4.5 to -5.5 MHz. The power contained in these plasma lines is comparable to the power from ion spectra during the quiet periods!

One should note, however, that the riometer gives *no indication whatsoever* of hard particle precipitation. If precipitating electrons are the cause for the enhanced scattering, these are not accompanied by high-energy electrons.

The same level of increased signal returns occurs again in the integration periods initiated at 16:36 and 16:37, although this time the filters in the plasma line channels are in a different position, and no plasma lines are observed. The power in the ion spectra during this event is plotted in figure 4.3.

After these spectacular events, we have a more quiet period with little or no observable precipitation and, apart from one integration period, no particularly strong ion spectra or plasma lines.

At 18:13 we have indications of a substorm onset. The riometer indicates an onset of high-energy particle precipitation, also confirmed by the ion spectrum power profile (see figure 4.10.) During the substorm we also see strong plasma lines on several occasions, and on one occation, we see the strongest plasma line echo of the entire experiment. Looking at the ion spectrum power, the event appears to last until 18:42.

The hard precipitation ends abruptly at 20:12 while soft precipitation persists at various intensities for most of the remainder of the experiment, dying away only close to 7 o'clock in the morning. This is consistent with the measurements done by the riometer.

3.5 Estimating the system constant

One of the first obstacles encountered in analysing the EISCAT data is the system constant. Usually one is only interested in the ion spectra, and for these measurements and the standard analysis, the dependency on the system constant is not too great, and a variation of some 20–30 % is tolerable as long as it does not change over the duration of the experiment. In this experiment we will have the situation where the plasma line frequency profile is inverted (i.e. decreasing with height) in the height region where we have strong plasma lines, so the ordering of the pulses will *decrease* the apparent distance of the two pulses instead of increasing it as intended. Since the exact frequency of the plasma line can be critically important in deciding which explanations are acceptable and which are not, finding out what pulse we see plasma line echoes from is important. We therefore need a reliable plasma line frequency profile. The single most important contribution to the plasma line frequency is the

electron density, which again is close to proportional to the received power which, of course, is proportional to the system constant. We therefore need to estimate this constant as well as possible. Fortunately, the fact that we have the plasma lines gives us an independent estimate of the Langmuir frequency, and this can be used to calibrate the system constant.

We used the quiet period between 08:00 and 12:40 for this calibration. To ease the calculation, we only used the first ten-minute period of every half-hour interval, ten such intervals in all. In these intervals we see clearly defined plasma lines from both pulses in all six channels, and there is no problem seeing which is which and at what range. We designed a MATLAB program to get each of the ten-minute integrations and perform the following series of steps:

- truncate the plasma line power profile to the lowest 40 range gates to eliminate the noisy upper ranges.
- determine the center height of the maximum of the plasma lines
- find T_e, T_e/T_i and $n_{e,\mathrm{raw}}$ as given by the standard (ion spectrum only) analysis, interpolated to the plasma line heights
- calculate the electron density as given by the ion spectrum data at the plasma line heights
- calculate the electron density as implied by the plasma line frequency (and the temperatures given from the analysis) at the same heigts
- determine the ratio of the two electron densities

This gives in all 120 estimates for the ratio, and these should be as close to unity as possible. We multiply the system constant used in the analysis with the mean of the ratios observed and repeat the procedure until we are satisfied. We found that after only three iterations, the mean of our ratios were within half of a percent of unity, with a standard deviation of 3.6 %.

For the practical implementation of this procedure, we didn't actually touch the definition of the system constant in the analysis program. Instead, we used a "magic constant" that our data was multiplied with before the analysis.

3.6 Estimating the temperatures

As it turned out, the signal in the plasma line channels was still too ambiguous for a definite identification after the calibration of the system constant. The

next factor significantly influencing the Langmuir frequency was the Debye length, since the Langmuir frequency is related to the plasma frequency by

$$\omega_{pl} = \omega_p \sqrt{1 + 3\alpha^2}. \tag{3.1}$$

where $\alpha^2 = K^2 \lambda_D^2$. The Debye length is dominated by the electrons, and is given as

$$\lambda_D = \sqrt{\frac{\varepsilon_0 T_e}{n_e e^2}} \tag{3.2}$$

where the electron density is related to the "raw" electron density through

$$n_e = n_{e,\text{raw}} \cdot \frac{1}{2}(1 + \alpha^2)(1 + T_e/T_i + \alpha^2) \tag{3.3}$$

Clearly, a good estimate of the electron temperature and the temperature ratios is necessary to obtain an accurate estimate of the plasma line profile.

3.6.1 What's a temperature?

As discussed in chapter 2, "temperature" is a concept that requires careful consideration when the plasma being studied is not described by a Maxwellian.

Within the framework of the standard analysis, this is not a problem. The analysis requires that our particle species are described by Maxwellian velocity distributions, and thus their temperatures are well defined. Even during the particle precipitations that produce "normally" enhanced plasma lines (30-40 times enhancement), the ratio of thermal particles to precipitating particles is so large that the Maxwellian temperature of the background distribution characterises the plasma.

The situation is nowhere near as clear-cut during the most interesting periods of this experiment, though. As we discussed in section 3.2, the results from the standard analysis of the ion spectra do not necessarily make very much sense even in the quiet periods, and during the disturbed events, they should not be trusted. The raw data and the errors in the standard analysis indicate that the plasma is far from Maxwellian. This makes the temperatures from the analysis even more dubious, and generally, the concept "temperature" must be applied carefully.

In order to calculate a Langmuir frequency profile we can compare to our observed plasma lines, we need to calculate the Debye length squared, which is proportional to electron temperature. Because of the uncertainity of the standard analysis during the disturbed events, we will not use the results of the analysis from the events themselves, but we will use an average of the temperatures from the analysed periods immediately before and after the events.

This average over surrounding time slices is probably the best we can do to estimate a temperature. Since these temperatures are used only in a correction term (on the order of α^2), the error from the temperature estimation shouldn't be too grave.

3.6.2 Identifying the plasma lines

As can be seen by e.g. figure 4.8, first panel, the plasma line signals are still indistinguishable after all these preparations; indeed, it's perfectly possible that the signal we observe is the sum of plasma lines at two different frequencies, some 25 km apart. Incidentally, this could account for up to a factor of two in the enhancement.

Chapter 4

Results

In this chapter, we will present in some detail the observations made in the experiment and try to draw some conclusions from them. This presentation will include more than a few graphs and full-page plots, and these will be described as they appear.

4.1 Short description of the plots

4.1.1 The power profile colour plates

The first six colour plates, numbers *i*–*vi*, show the received power, untouched except for R^2 correction, of the seven channels where power profiles were measured. Range, from 58 to 235 km, is on the vertical axis, and time (UT) on the horizontal, as is customary in ionospheric physics. The colour scale indicates the power, normalised such that 1 is the power of the scatter expected from a "cold" — i.e. $T_e = T_i$, $\alpha^2 = 0$ — $10^{11}\,\mathrm{m}^{-3}$ thermal plasma. (This is what is sometimes referred to as the "raw" electron density, here in units of $10^{11}\,\mathrm{m}^{-3}$.) The first panel is the power profile taken from LP1, the shorter of the two long pulses. The six other panels are identical plots for the six channels used for plasma line measurements. The ranges reported for these channels are assuming plasma lines from LP1. The plasma lines from LP2 are, as mentioned in the previous chapter, in fact some 25 km higher up than the range scale indicates. The normalisation of power in the plasma line channels is identical to the one used in the ion spectrum power profile, and the first two plates, covering the first eight hours of the experiment, demonstrate the $\frac{1}{2}\alpha^2$ ratio of plasma line power to ion spectrum power which is expected from a thermal plasma. The offsets of these six channels are given in table 3.1.

During the quiet time of the first eight hours we can immediately identify the changing of the filter settings by the distance to the plasma lines. Where we see two plasma lines simultaneously in one channel, the lower one is the LP2 plasma line, and it is thus 25 km above the indicated range.

One more feature of these observations worth noting is that we observe plasma lines throughout the 24 hours of the experiment.

4.1.2 The analysed long pulse colour plates

The next six colour plates, numbers *vii–xii*, show the results of the standard analysis of the LP1 ion spectra. (GUISDAP 1.6, gated.) Features worth noting here are the apparent enhanced electron densities around 16:30 and 18:30, and also the increased ion temperature around 16:30.

For completeness, the results of the analysis of LP2 has also been included in colour plates *xiii-xviii*. Since the range gates of these ACFs start at 126 km, they are of less interest for our purposes here. The observations of the topside of the ionosphere can make some of the features observed further down easier to explain in some cases.

4.1.3 The plasma line plots

These plots are rather complex, and need a detailed explanation. Please refer to figure 4.1 during the explanation.

- In the upper left hand corner, the dashed line represents the raw electron density. As noted above, this is simply proportional to the range corrected power at the receiver.
- In the middle right hand panel, the electron and ion temperatures are plotted with errorbars. The points are from the analysis of LP1, and the lines (solid and dashed) are linear interpolations of these points to the power profile grid. The interpolation has been truncated when any of the temperatures went below 100 K. As pointed out in section 3.2, the analysis is based on ACFs from a too short pulse. Continuing the interpolation down to 100 K is therefore more a formality to complete the picture given by the analysis than an attempt to assign meaningful physical parameters to the plasma at these altitudes.

  During our special events, when we don't trust the results of the standard analysis, the temperatures given in these plots will be a mean value of temperatures before the period of unreliable analysis. In these cases, the

period from which the temperature is taken is indicated in the figure caption. The errorbars on the temperature graphs is a maximum of the errors as given by the analysis and the standard deviation of the results.

- In the upper right hand corner, $\alpha^2 = K^2\lambda_D^2$ estimated on the power profile grid is plotted. This estimation is based on the raw electron density and the temperatures in the previously discussed panels. Since incoherent scattering assumes $\alpha^2 \ll 1$, this estimation is considered invalid and not plotted whenever $\alpha^2 > 0.25$.

- based on α^2, T_e and T_i, the correction to the raw electron density is calculated. The corrected electron density, as given by (3.3), is plotted as a solid line in the upper left hand panel. For a greatly disturbed plasma, this can be thought of as an "equivalent" electron density; the electron density necessary to produce a thermal scattering of the same intensity.

  The points with errorbars in this panel are the electron densities given by the standard analysis; the same analysis that gives the temperatures mentioned previously. Ideally, these points should all lie on the solid line. We will see that even in the thermal situation, there is quite some discrepancy at the lower and higher ends of the range. As discussed in section 3.2, this is believed to be due to the length of the pulse (30 km) being greater than the scale height of the ionosphere at these altitudes and the length of the pulse leaving it incapable of resolving the shorter correlation time of the plasma at the lower altitudes, while we suspect that insufficient signal strength causes the discrepancy at higher altitudes.

- The plasma frequency, (A.3), and the Langmuir frequency, (3.1), are plotted in the middle left hand panel. The vertical dotted lines every 100 kHz indicate the center frequency of the plasma line channels. The intersection of these lines and the solid graph therefore indicate the altitude and channel where we can expect to observe plasma lines.

- The lower six panels are again the plasma line power profiles. Now, the power is represented as the equivalent plasma line temperature. As explained in section 2.4 and expressed through equation (2.44), this is the electron temperature required to produce a *thermal* plasma line of the same power. By comparing the plasma line temperature with the electron temperature at the same altitude, we can easily determine the enhancement.

  As previously noted, the range of the plasma line is ambiguous, since we can have plasma lines from both pulses in each channel. In these plots, this is indicated by *two* height scales, one on each side. The left hand scale applies to plasma lines from LP1 — the largest frequency offset — while

the right hand scale applies to plasma lines from LP2. In each plot, the two offsets that are seen in each channel are indicated, in MHz, below the panel. Please note that the smallest of these offsets, the first value, corresponds to the right hand side height scale, curiously enough.

The signal strength range dependence has been corrected for relative to LP1. This means that plasma lines resulting from LP2 are more powerful than the figures would indicate. The difference is greatest at lower ranges. As an attempt to indicate the significance of this effect, we have also plotted the power corrected for range relative to LP2 in the lower of the two plasma lines in figure 4.1. The range relative to LP2 is greater, therefore the most intense of the two plasma lines from LP2 is the correct one. For the disturbed situations treated subsequently, such immediate identification is impossible.

For each event, the plots after the first, complete plot consist of only the plasma and Langmuir frequency profiles and the plasma line panels.

4.2 A Thermal situation; 08:40 – 08:50

For comparison, we will first present the thermal situation. The first four hours of the experiment are quiet times. The ionisation is photoionisation, and there are no significant disturbances. Colour plate *i* illustrates this. There is no change in the ionosphere during these first four hours. This sedate impression is confirmed by the analysis of the same period, plates *vii* and *xiii*.

Figure 4.1 is typical plasma line data from the same period. The increase of electron density and temperature with altitude ensures a Langmuir frequency which steadily increases with height, just as anticipated by the designers of the experiment. In the plasma line channels, we can see two clearly separated plasma lines in each channel, and there is no problem separating and identifying the two lines. Indeed, this straightforward separation is the reason this period is one of the periods used for the calibration described in the previous chapter.

The ion spectrum plot for the same period, figure 4.2, is also without surprising features. At lower altitudes wee see the Gaussian spectrum of a collision-dominated plasma, increasing in power with height, and evolving into the familiar double-humped spectrum from about 180 km.

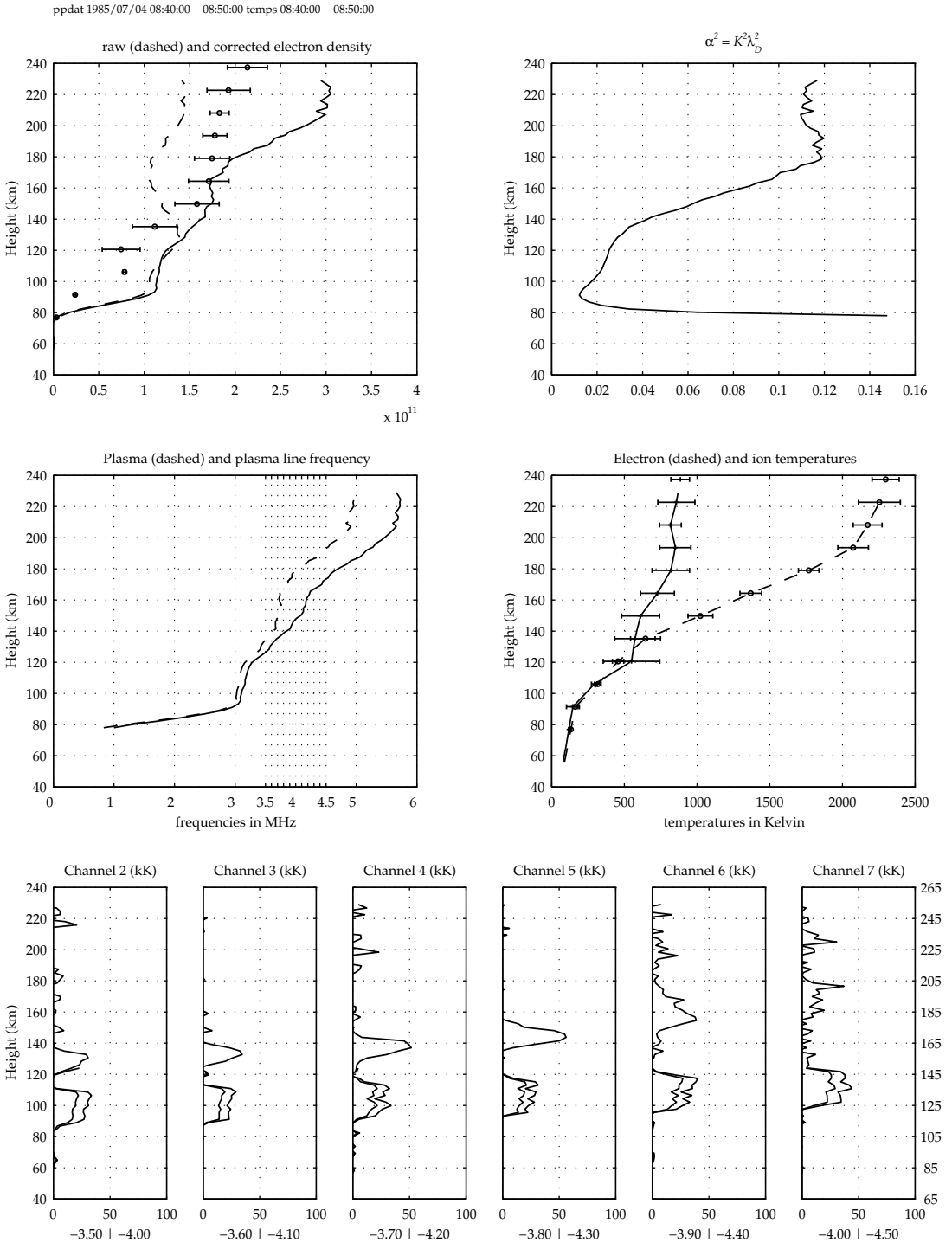

Figure 4.1: Plasma line Power Profile data 08:40–08:50 UT. As we have written in the text, continuing the interpolation of the temperatures as far down as we have done is not an attempt to assign physical parameters to the plasma at these altitudes, but more of a formality

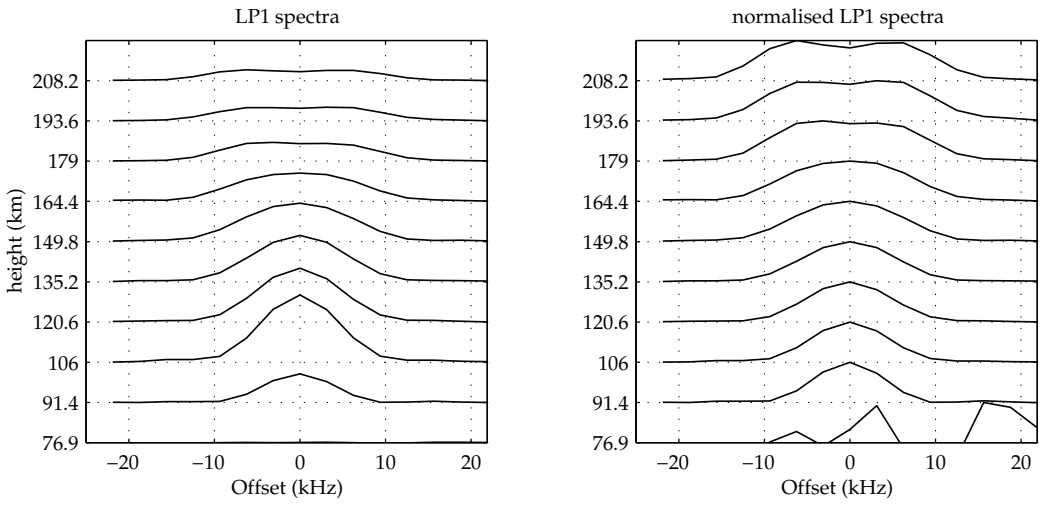

Figure 4.2: Ion spectra from 08:41 – 08:42. The left panel shows the spectra on the same scale, while the right panel shows the self-normalised spectra.

4.3 Event 1; 16:18 – 16:23

The temperatures used throughout this event are taken from the period 16:10 – 16:18, the relatively quiet period immediately preceding the event. From the analysed data, colour plate *ix*, we can verify that the temperature profiles are similar before and after the event. The event comprises plasma lines from the 4.5 to 5.5 MHz downshifted frequency interval, the interval monitored from 16:20 to 16:30; and most likely the upper half of these offsets. In figure 4.3, we have plotted the power of the lowermost ten renge gates of LP1 as a function of time before, during and after this event.

The integration period 16:18 – 16:19 is a fairly normal precipitation situation. The power profile data, figure 4.6, indicate a maximum in electron density at about 105 km. This is not consistent with the analysed data, which shows maximum electron density at 137 km. This discrepancy was touched upon briefly above.

The next integration period, 16:19 – 16:20, shows the onset of the event. If we interpret the ion spectrum total power in terms of electron density, we have an increase in electron density from $2.7 \cdot 10^{11}\,\mathrm{m}^{-3}$ to $4.0 \cdot 10^{11}\,\mathrm{m}^{-3}$ in just one minute. There are no plasma lines observed in this period, as we can see from the uppermost panels in figure 4.7. In this integration period, the filters are in the -3.5 to -4.5 MHz range.

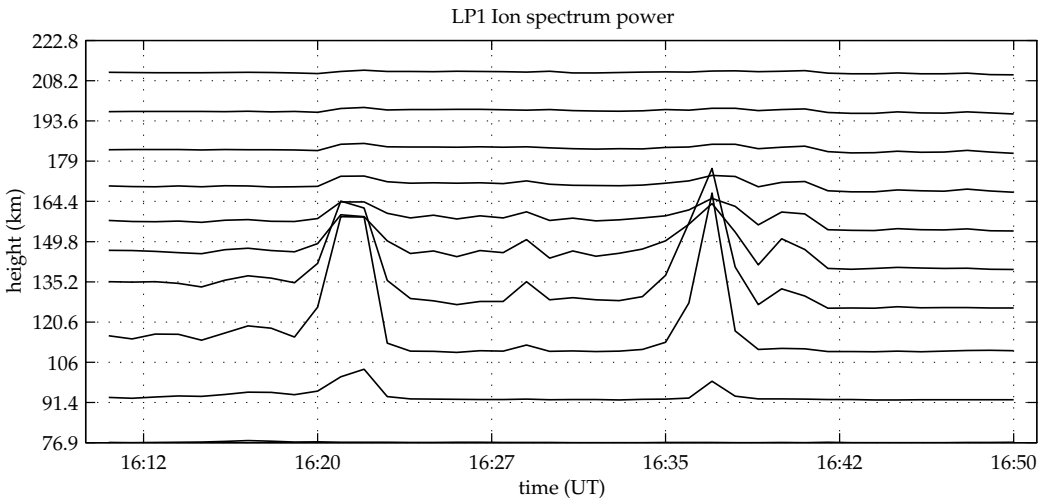

Figure 4.3: Ion spectrum power (lag zero from LP1 ACFs) as a function of time for the ten lowermost range gates of LP1. We can see that we have another period of enhanced scattering after the plasma line filters have been moved to a different position.

The next integration period witnesses a further enhancement of equivalent electron density to $\approx 9.5 \cdot 10^{11}\,\mathrm{m}^{-3}$. At the same time, the filters in the plasma line channels are moved to the -4.5 to $-5.5\,\mathrm{MHz}$ range, and we new observe plasma lines of strong to extremely strong enhancements in four of the channels. From the plasma line plot, the middle line of figure 4.7, we see the previously mentioned reversal of plasma line frequency profile, now very pronounced. There are several reasons to believe that these plasma lines are from the shorter pulse, and thus corresponds to the higher of the two offsets monitored in each channel:

1. The plasma line is too limited in height to be from the $210\,\mu\mathrm{s}$ pulse
2. The power in the plasma line increases with higher offsets in channels 4–7, and
3. We have an extremely strong plasma line in channel 7 and absolutely nothing in channel 2, the highest offset of which matches the lower of the offsets in channel 7.

From this we conclude that the plasma lines we see in channels 4–7 are from offsets of -5.2 to $-5.5\,\mathrm{MHz}$, and at altitudes of 180 to 145 km, correspondingly. It would seem that despite our efforts to calibrate these measurements, there is still improvement possible. For the best correspondence, the plasma line graph

		Ch. 2	Ch. 3	Ch. 4	Ch. 5	Ch. 6	Ch. 7
16:20	$T_{\max}$	55.64	62.32	92.94	237.04	427.28	531.61
	Alt.	198.37	187.43	183.05	165.54	152.41	145.85
16:21	$T_{\max}$	71.16	58.55	44.14	148.56	378.56	214.40
	Alt.	215.89	196.19	185.24	152.41	132.72	126.15
16:22	$T_{\max}$	54.91	266.70	630.58	594.90	460.81	358.23
	Alt.	196.19	134.90	132.72	123.97	121.78	119.59
16:23	$T_{\max}$	117.82	81.16	72.54	95.63	175.77	153.38
	Alt.	176.48	119.59	113.03	130.53	132.72	152.41
16:24	$T_{\max}$	202.41	234.07	115.89	95.10	123.69	308.52
	Alt.	143.66	126.15	119.59	123.97	126.15	126.15
16:25	$T_{\max}$	126.14	78.53	88.38	138.64	156.16	167.62
	Alt.	156.79	167.73	115.21	119.59	126.15	143.66
16:26	$T_{\max}$	123.73	267.95	394.06	191.90	146.91	171.06
	Alt.	139.28	130.53	148.03	121.78	117.40	121.78
16:27	$T_{\max}$	179.04	214.66	139.79	82.24	153.80	238.08
	Alt.	145.85	150.22	158.98	113.03	108.65	119.59
16:28	$T_{\max}$	62.62	115.63	95.51	61.53	157.71	178.61
	Alt.	148.03	126.15	185.24	132.72	117.40	130.53
16:29	$T_{\max}$	129.16	79.41	86.92	76.91	101.57	141.43
	Alt.	165.54	128.34	123.97	128.34	137.09	148.03

Table 4.1: The temperature and altitude of the peak of the plasma line channels during event 1, assuming that the prominent plasma lines are from LP1. The maximum is just the maximum point, no convolutions or weightings have been made. The temperatures are in units of 1000 K, and the altitudes are in km.

should intersect the -5.5 MHz line at about 145 km. If we believe the plasma density (and thus the plasma frequency) at this altitude, we need $\alpha^2 \approx 0.055$ here to achieve the desired intersection. This is some 50 % above the measured value. If there are processes in the plasma that have the effect of locally increasing the Debye length, such as an increase in electron temperature, this could make up the difference between the calculated and observed frequencies. The most intense of these plasma lines show a plasma line temperature of $530 \cdot 10^3$ K, corresponding to 45 eV. This is 2-4 times more intense than previously reported enhanced plasma lines [*Kirkwood et al.*, 1995; *Valladares et al.*, 1988]. Compared to the electron temperature used during this event, ≈ 1000 K at this altitude, this is an enhancement of more than 500 times over the thermal level. In channel 6 the enhancement is 375 times, and in channel 5 we have a power ≈ 160 times higher than predicted from electron temperature

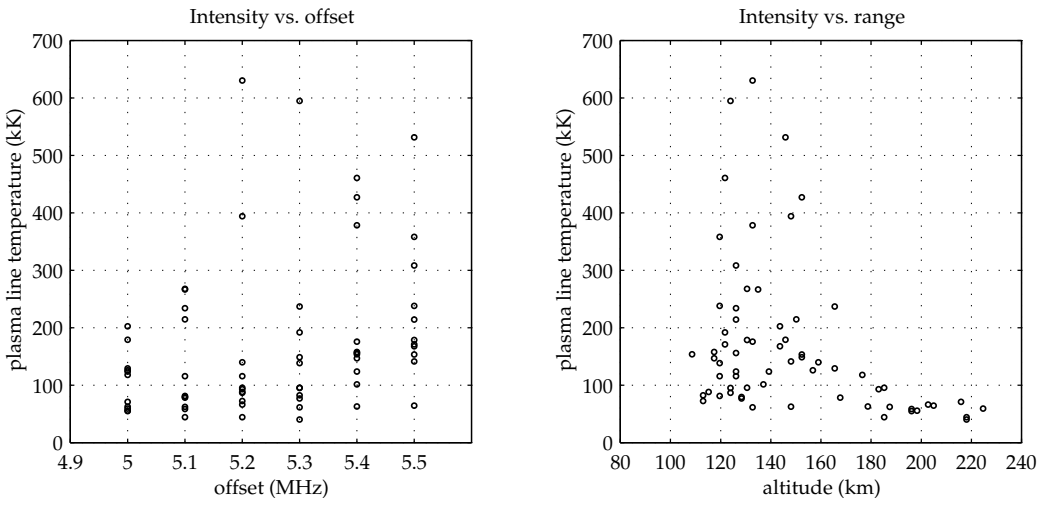

Figure 4.4: The maximum points from each of the plasma line channels for the period 16:20 to 16:30 are plotted against offset frequency in the left panel and against altitude in the right panel. This figure corresponds to figure 5 in [*Kirkwood et al.*, 1995] except that we are using Kelvin for the temperatures.

alone. The plasma line temperatures and altitudes from this and the following integration periods is summarised in table 4.1. In figure 4.4, the maximum points from each of the plasma line channels for the entire ten-minute period are plotted against offset frequency and altitude.

For the period 16:21 – 16:22, the ion spectrum power profile looks almost unchanged from the previous minute. The plasma lines are radically different, though. Where we had lines at sharply defined altitudes in the previous minute, we now have, in channel 7, a temperature of more than 100 kK from 120 to 180 km, a peak at 130 km with features extending up to 180 km in the neighbouring channel as well, and a peak at much lower power (but still some 10 eV) in channel 5. Another feature we could point out is the weak signal in channels 3 to 5 between 100 and 120 km. Assuming this is the bottom of the *E* layer, this is a further indication that the increase in raw electron density is not really due to increased electron density after all.

The next minute, the plasma lines of sharply defined altitudes are back and even stronger than previously. The received power is the highest of this event, 595 and 630 kK or 55 eV in two of the channels, and not much less in two of the other channels. This time, all the lines are from altitudes between 120 and 140 km, some 20 km lower than two minutes ago. Again comparing to the electron temperatures measured before the event, the enhancement is now a

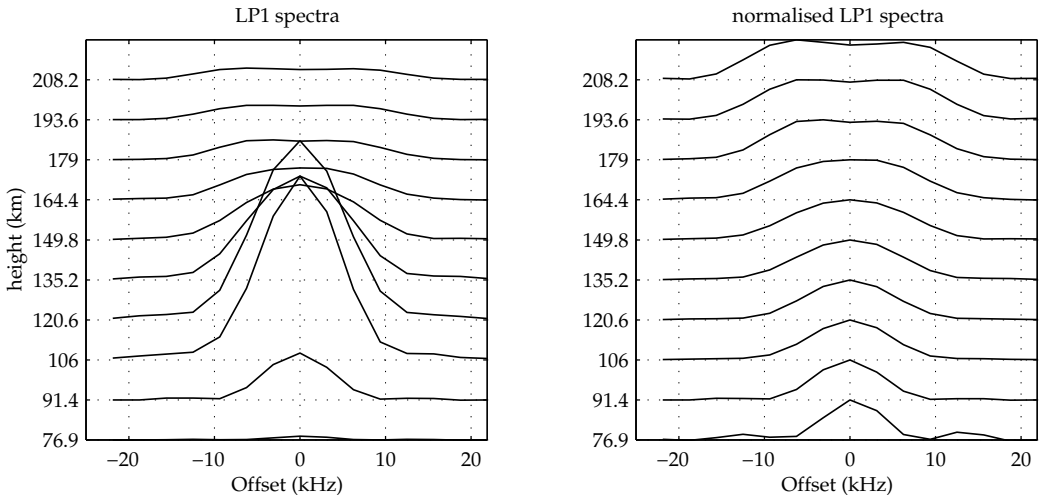

Figure 4.5: Ion spectra from 16:20 – 16:21. The left panel shows the spectra on the same scale, while the right panel shows the self-normalised spectra. By comparing with figure 4.2, we see that the spectra are of approximately the same shape, while the power at zero frequency has been tripled or more at 106 and 135.2 km, and we now have a signal of a distinct shape even down at 76.9 km.

thousand times the thermal level! At the same time, the electron density, as given by the power profile is down to some 40 % of the value from the previous minute and the maximum altitude has climbed to the more moderate value of 115 km.

The next minute from 16:23 to 16:24, presents a new puzzle. Our event is all but over. The plasma line power is back to normal magnitudes; as is the ion spectrum power profile. Although the electron density still decreases, now slowly, with altitude above 120 km, we now have a Langmuir frequency profile which is flat or weakly increasing with altitude. This is confirmed in the plasma line channels 3 – 6. The curious part appears in channels 2 and 7, which both display two plasma lines. Even with the different ways of choosing offsets and altitude scales, there is no obvious way to make these observations fit a single Langmuir frequency profile. Of course, the two lines could be from different pulses at the same offset in the two channels (LP1 in channel 2 and LP2 in channel 7), but then it becomes more difficult to explain the lines in channels 3–6.

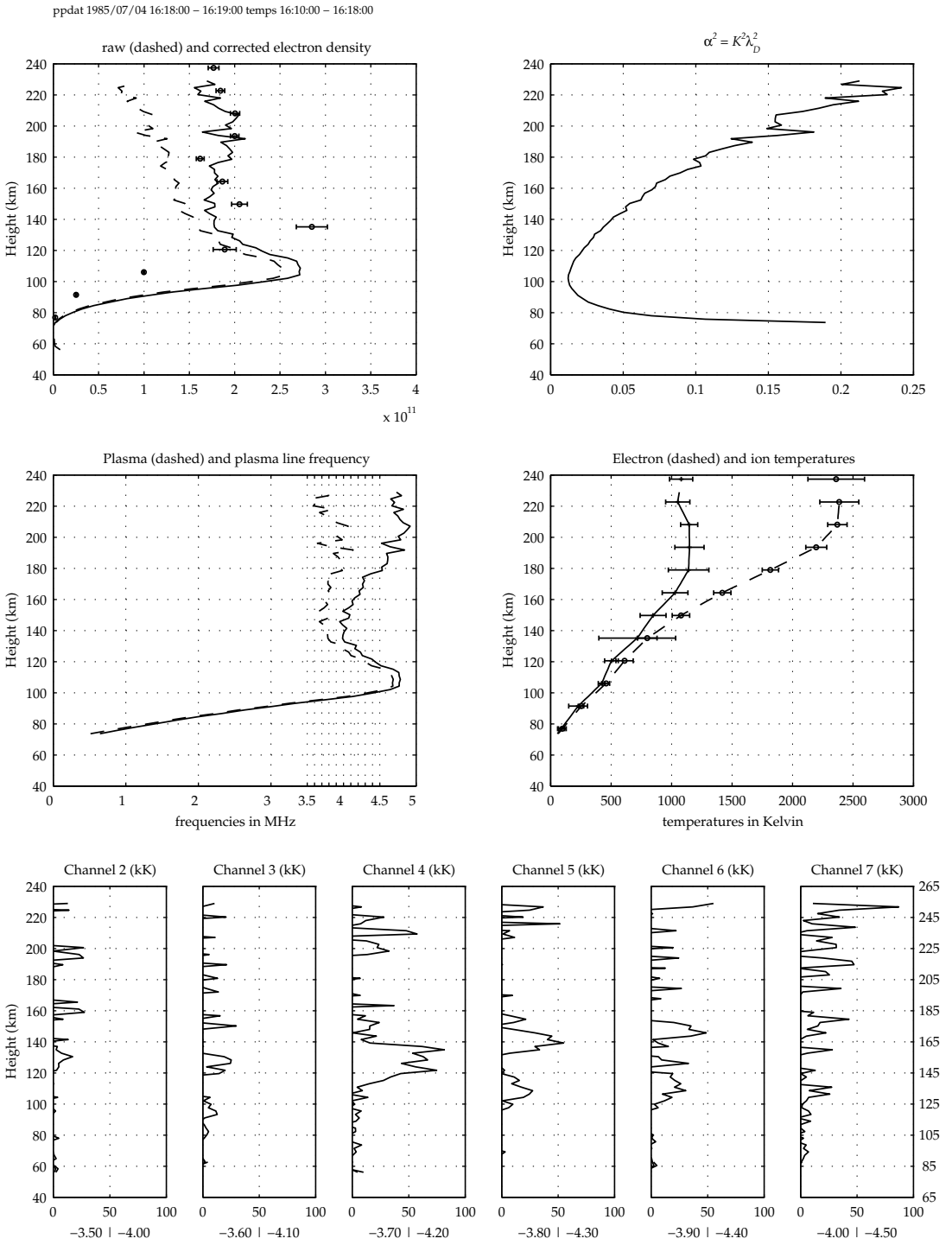

Figure 4.6: Plasma line Power Profile data 16:18–16:19 UT. The temperatures used are from the period 16:10 – 16:18

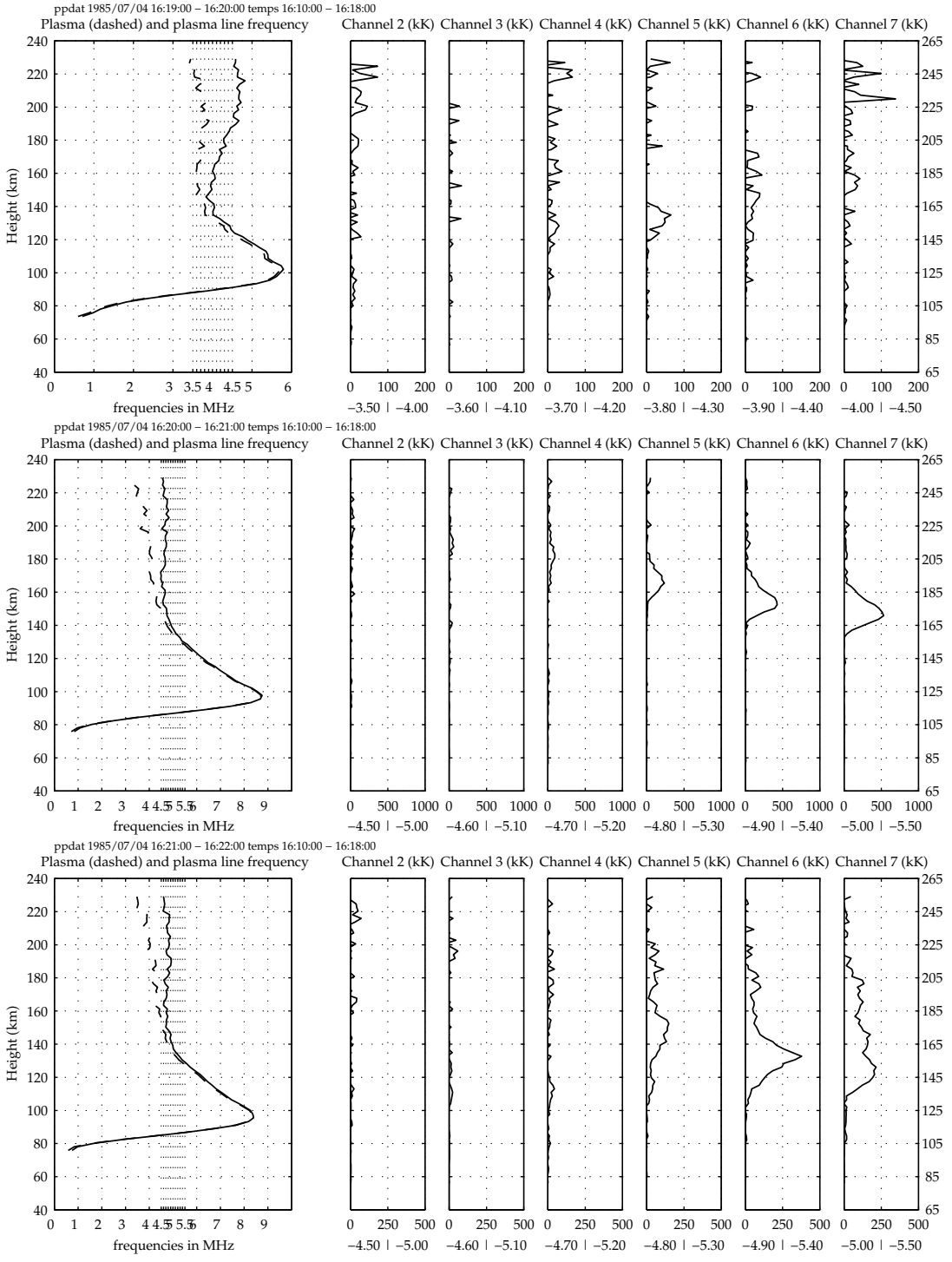

Figure 4.7: Plasma lines for the period 16:19 – 16:22. The temperatures used are from the period 16:10 – 16:18

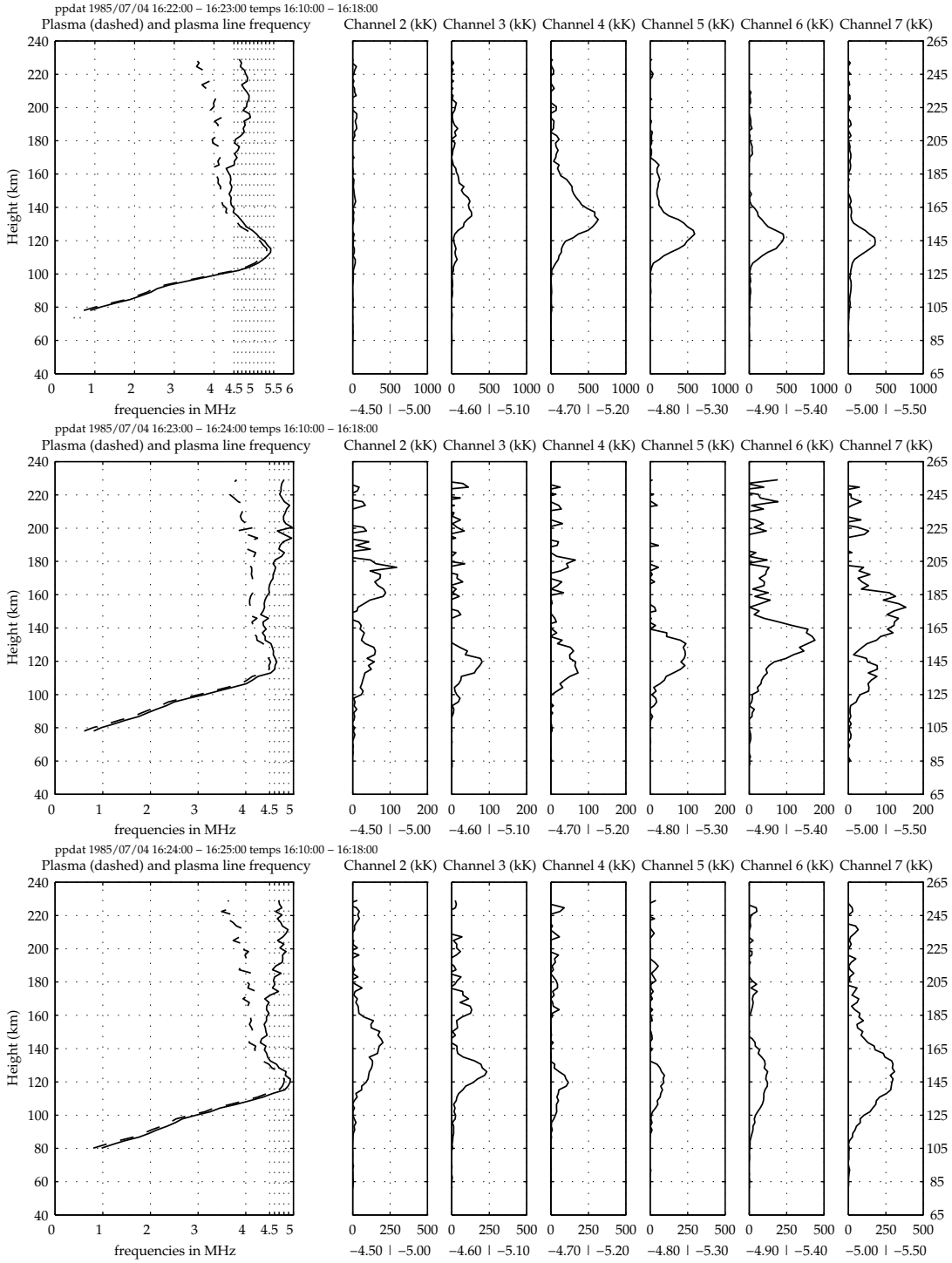

Figure 4.8: Plasma lines for the period 16:22 – 16:25. The temperatures used are from the period 16:10 – 16:18

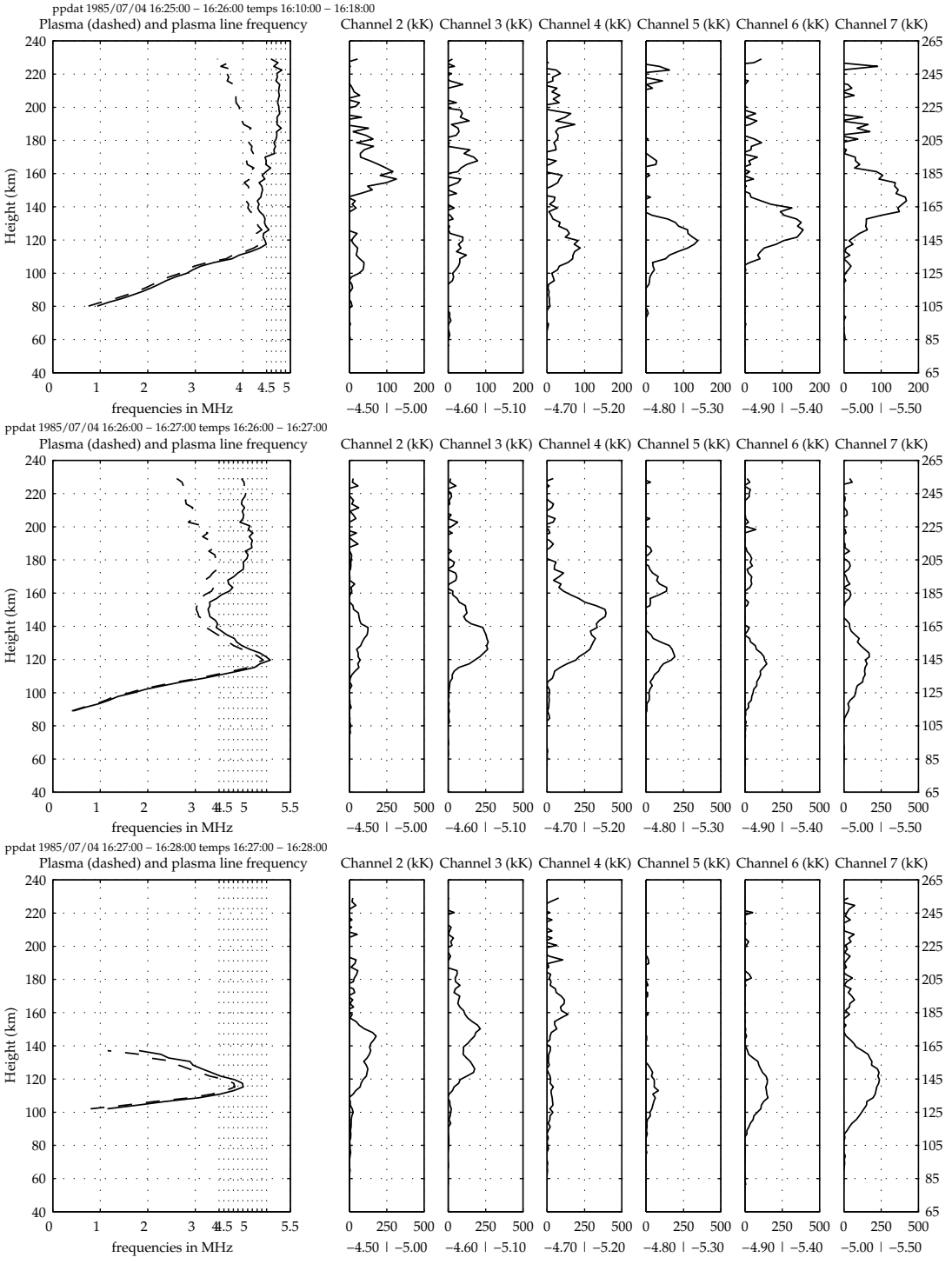

Figure 4.9: Plasma lines for the period 16:25 – 16:28. The temperatures used are from the period 16:10 – 16:18

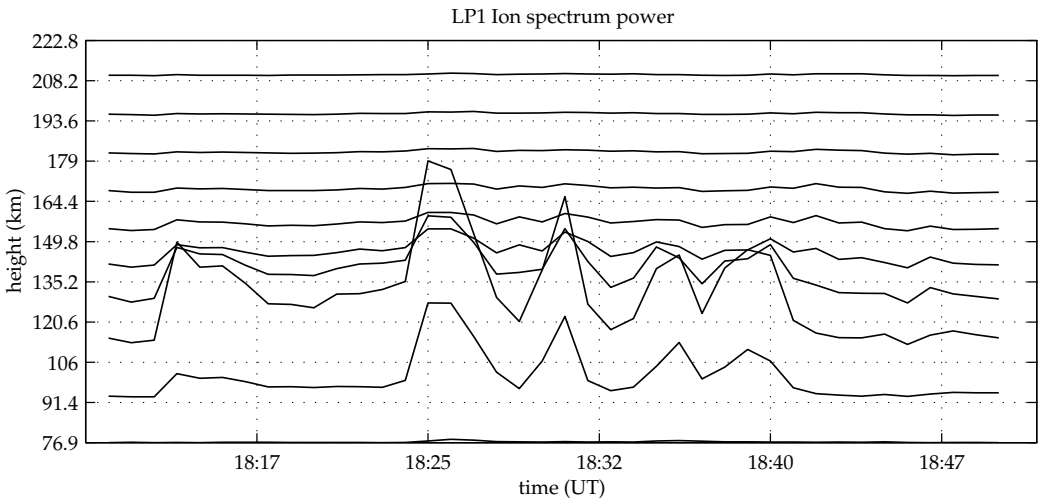

Figure 4.10: Ion spectrum power (lag zero from LP1 ACFs) as a function of time for the ten lowermost range gates of LP1. As we can see, the lower ionosphere is severely disturbed in this period, and we have the plasma line filters in the positions of the greatest offsets only during the first part of this event.

4.4 Event 2; 18:18 – 18:25

The temperatures used throughout this event are taken from the period 18:05 to 18:15, the relatively quiet period immediately preceding this event. This event, like the previous one, comprises plasma lines from the 4.5 to 5.5 MHz downshifted frequency interval, the interval monitored from 18:20 to 18:30.

The power in the ion spectrum ACFs are plotted as a function of time in figure 4.10, and the maximum points of the different plasma line channels and their heights are reproduced in table 4.2 and presented graphically in figure 4.11 in the same way as we did for event 1.

As in the previous event, we observe the transition from an ordinary precipitation situation in the 18:19 to 18:20 period, figure 4.12, to the more unusual situation. We again observe the peak of the plasma frequency profile being lowered to 90 km, and the inversion of the plasma line frequency profile. Determining which plasma line we see is as difficult as during the last event. In the first few integration periods of the event, 18:20 to 18:23, the altitudes of the plasma lines seem to indicate that we observe plasma lines from LP1, possibly on both sides of the raw electron density peak. In the next three minutes, the situation becomes more muddled. The peak of the frequency profiles has increased from 6 to more than 9 MHz, and the altitudes where we expect

		Ch. 2	Ch. 3	Ch. 4	Ch. 5	Ch. 6	Ch. 7
18:20	$T_{\max}$	49.98	58.56	47.98	37.99	34.44	72.14
	Alt.	178.67	218.08	220.27	104.28	104.28	220.27
18:21	$T_{\max}$	72.87	86.79	85.68	81.42	82.35	93.53
	Alt.	108.65	106.46	106.46	218.08	104.28	102.09
18:22	$T_{\max}$	71.71	67.88	83.58	70.85	65.04	79.27
	Alt.	106.46	108.65	108.65	108.65	102.09	97.71
18:23	$T_{\max}$	76.21	97.06	94.24	86.30	104.76	113.93
	Alt.	115.21	117.40	115.21	115.21	113.03	110.84
18:24	$T_{\max}$	100.57	201.47	258.76	243.44	757.77	265.59
	Alt.	128.34	126.15	126.15	121.78	137.09	117.40
18:25	$T_{\max}$	89.15	200.13	194.99	209.72	271.52	318.53
	Alt.	139.28	128.34	126.15	126.15	128.34	126.15
18:26	$T_{\max}$	99.29	115.58	132.26	150.03	168.83	192.60
	Alt.	134.90	134.90	132.72	128.34	126.15	126.15
18:27	$T_{\max}$	60.29	48.48	43.66	29.45	45.19	50.09
	Alt.	220.27	161.16	220.27	102.09	222.46	220.27
18:28	$T_{\max}$	86.46	136.82	177.27	186.18	160.59	191.68
	Alt.	128.34	126.15	130.53	123.97	123.97	121.78
18:29	$T_{\max}$	82.77	144.35	197.86	187.50	170.19	157.31
	Alt.	222.46	121.78	121.78	121.78	115.21	117.40
18:30	$T_{\max}$	56.49	9.35	39.56	29.51	35.97	78.63
	Alt.	226.84	165.54	196.19	167.73	220.27	215.89

Table 4.2: The temperature and altitude of the peak of the plasma line channels during event 2, assuming that the prominent plasma lines are from LP1

plasma lines increases to close to 120 km and above. In the period from 18:24 to 18:25 we have the strongest plasma lines of the whole experiment in channel 6; the plasma line temperature is 750 kK, a thousand times higher than the electron temperature at the same altitude. In this integration period, channels 6 and 7 display two distinct peaks in the intensity. The highest peak in channel 6 is almost 20 km above the trend from channels 2 to 5. Determining which of the offsets we're seeing is not possible from these plots. The final integration period plotted displays plasma lines with an altitude extent which would indicate the 210 μs pulse. Again we observe that plasma lines are observed at altitudes not matching the intersection of the plasma line frequency profile and the filters.

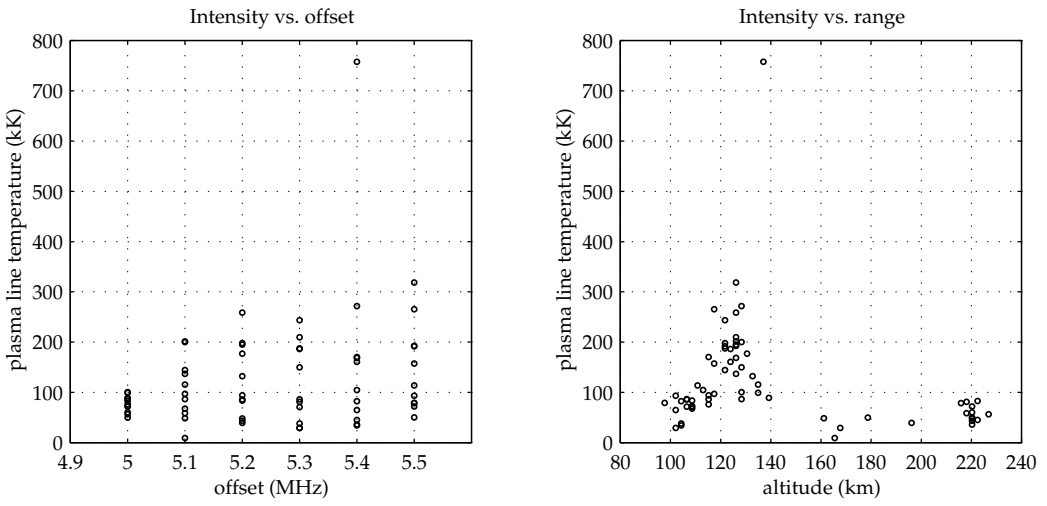

Figure 4.11: The maximum points from each of the plasma line channels for the period 18:20 to 18:30 are plotted against offset frequency in the left panel and against altitude in the right panel.

4.5 Discussion

We have presented in detail the observations made of two very interesting events causing enhanced scattering from both the ion-acoustic and the plasma line components of the incoherent scatter spectrum. We will briefly consider how well these observations fit the different enhancement mechanisms presented in chapter 2.

4.5.1 Plasma instabilities

The ion-ion and electron-ion beam instabilities discussed in section 2.2 were initially thought to be at least part of the explanation for the observations made in this experiment. These instabilities severely distort the ion-acoustic part of the scattering spectrum, typically resulting in skewed spectra with one or sometimes both of the shoulders in the spectrum very pronounced. As the ion spectra we observe during our events are single-humped, clearly a different shape, we reject these instabilities as an explanation for the phenomenon.

The electron-electron beam instability is also rejected as an explanation. By carrying out the same calculations as those made in section 2.2.4, we can see that it might occur at frequencies affecting the plasma lines. The onset of the instability would require the one-dimensional electron distribution to display

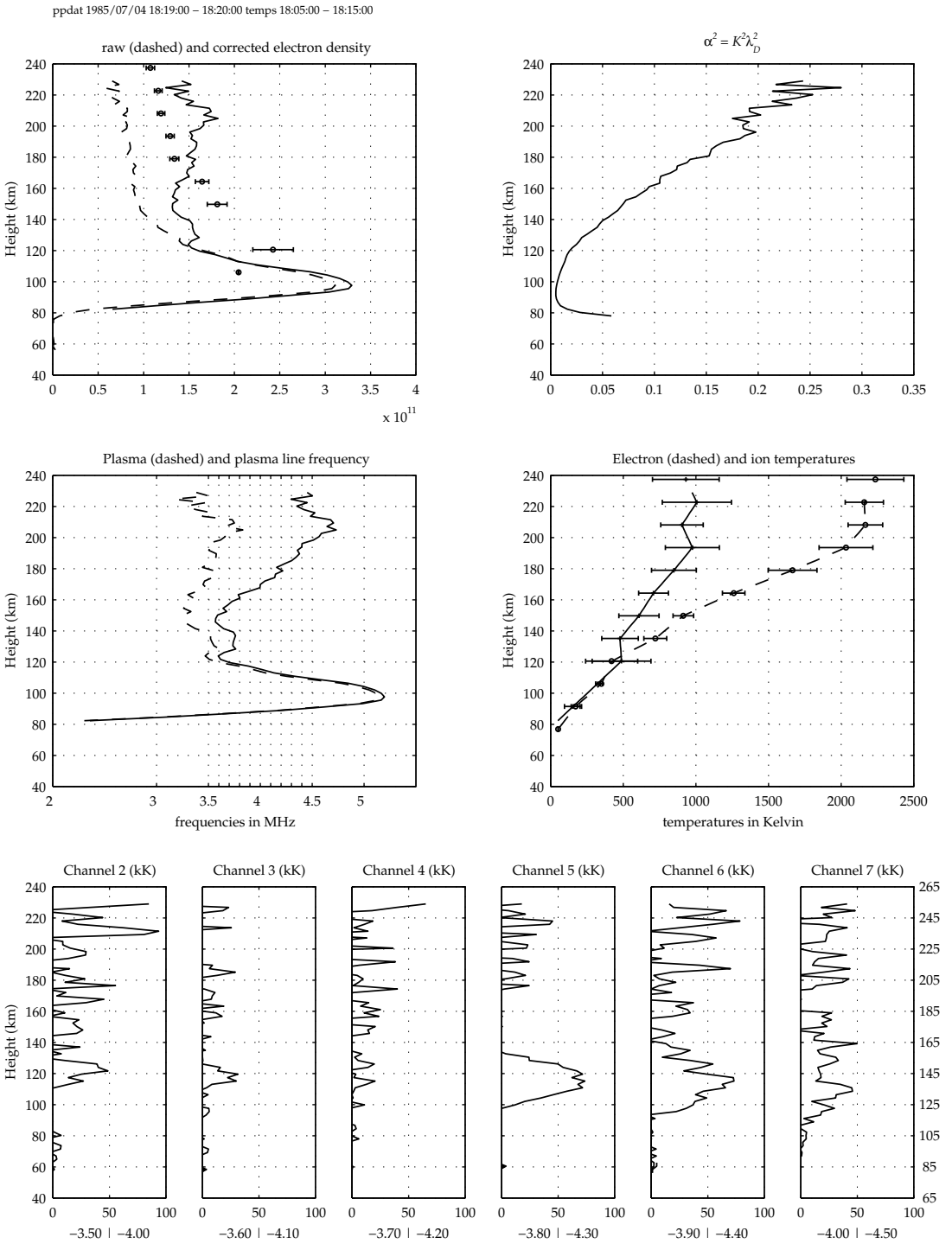

Figure 4.12: Plasma line Power Profile data 18:19–18:20 UT. The temperatures used are from the period 18:05 – 18:15

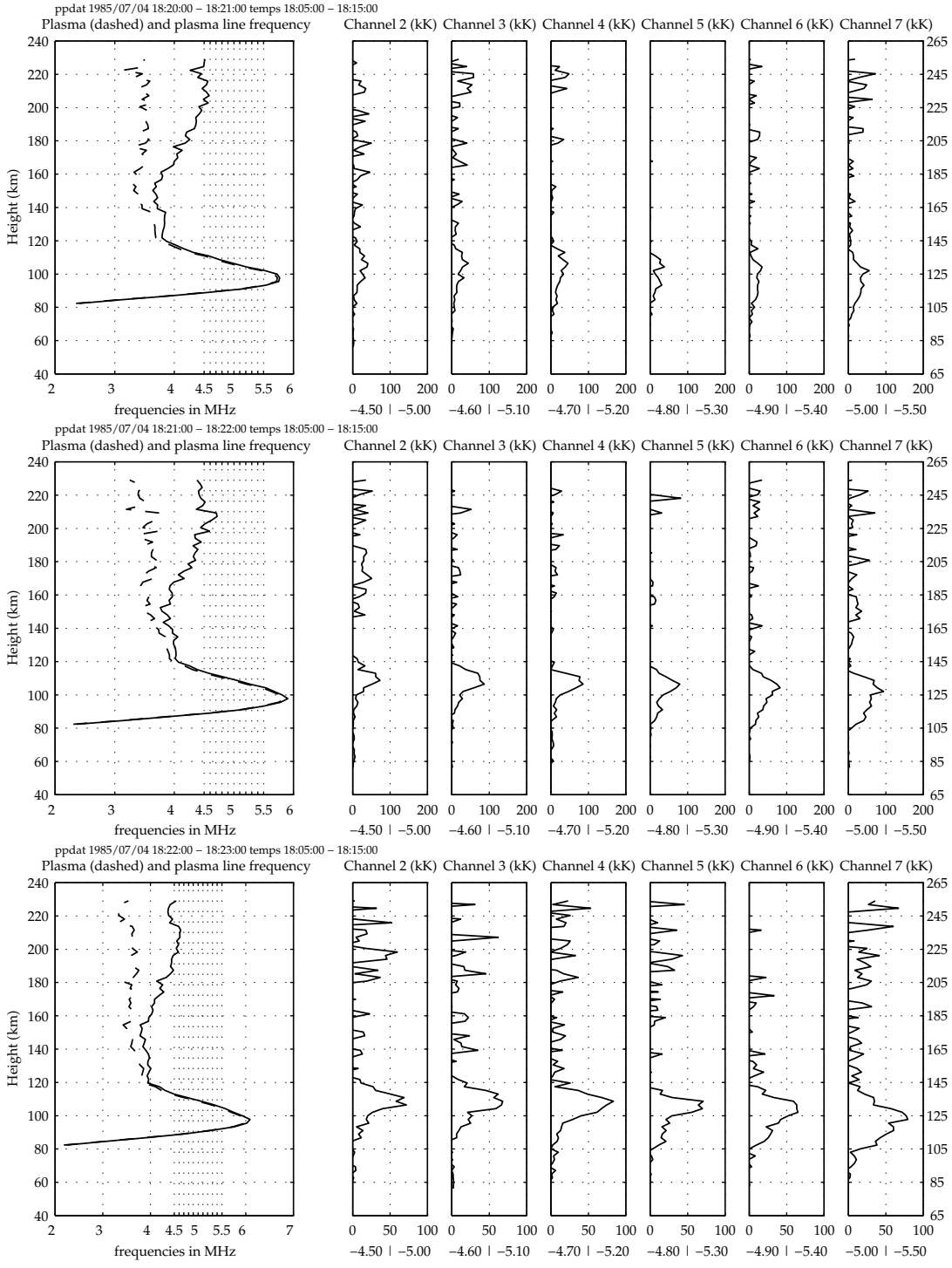

Figure 4.13: Plasma lines for the period 18:20 – 18:23. The temperatures used are from the period 18:05 – 18:15

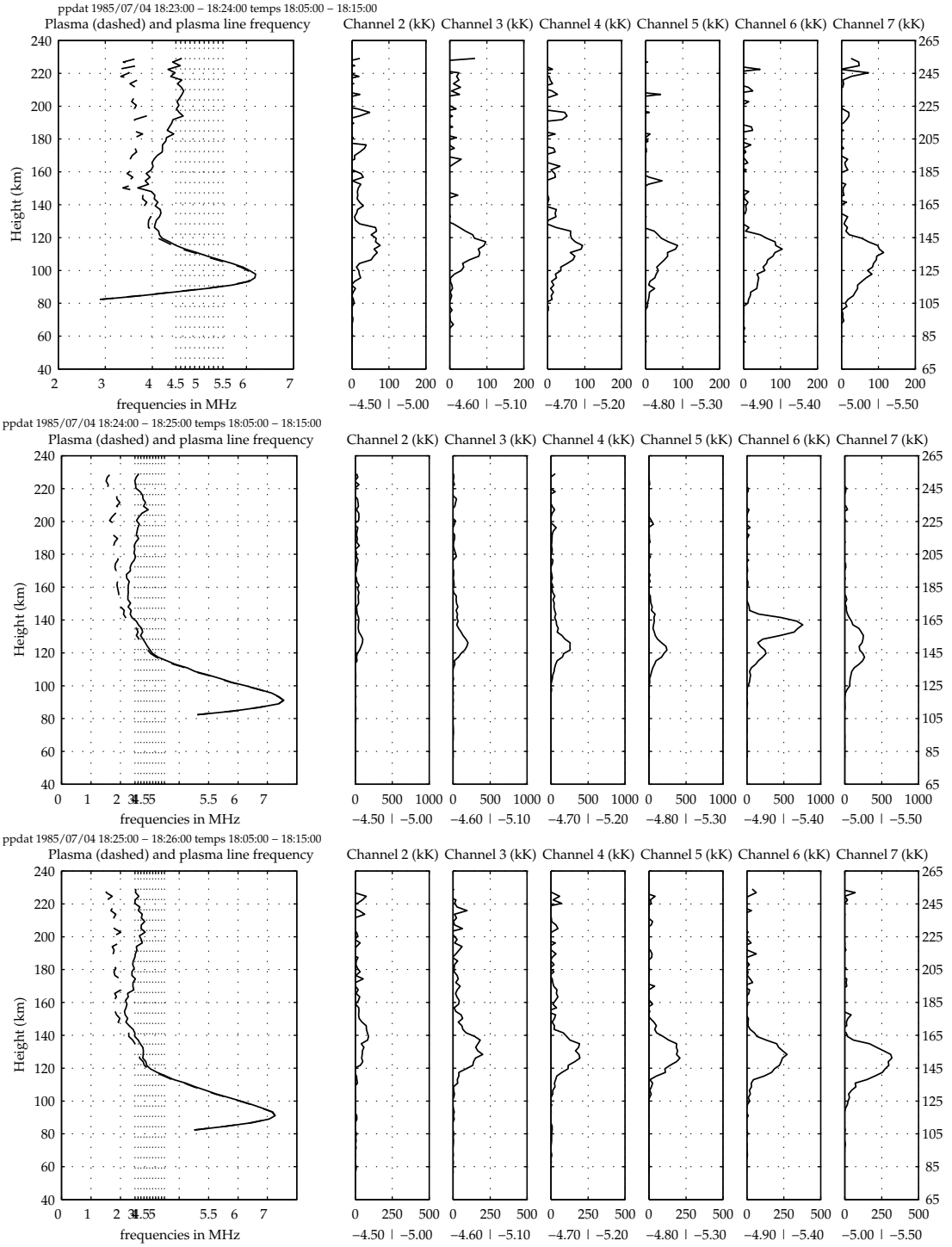

Figure 4.14: Plasma lines for the period 18:23 – 18:26. The temperatures used are from the period 18:05 – 18:15

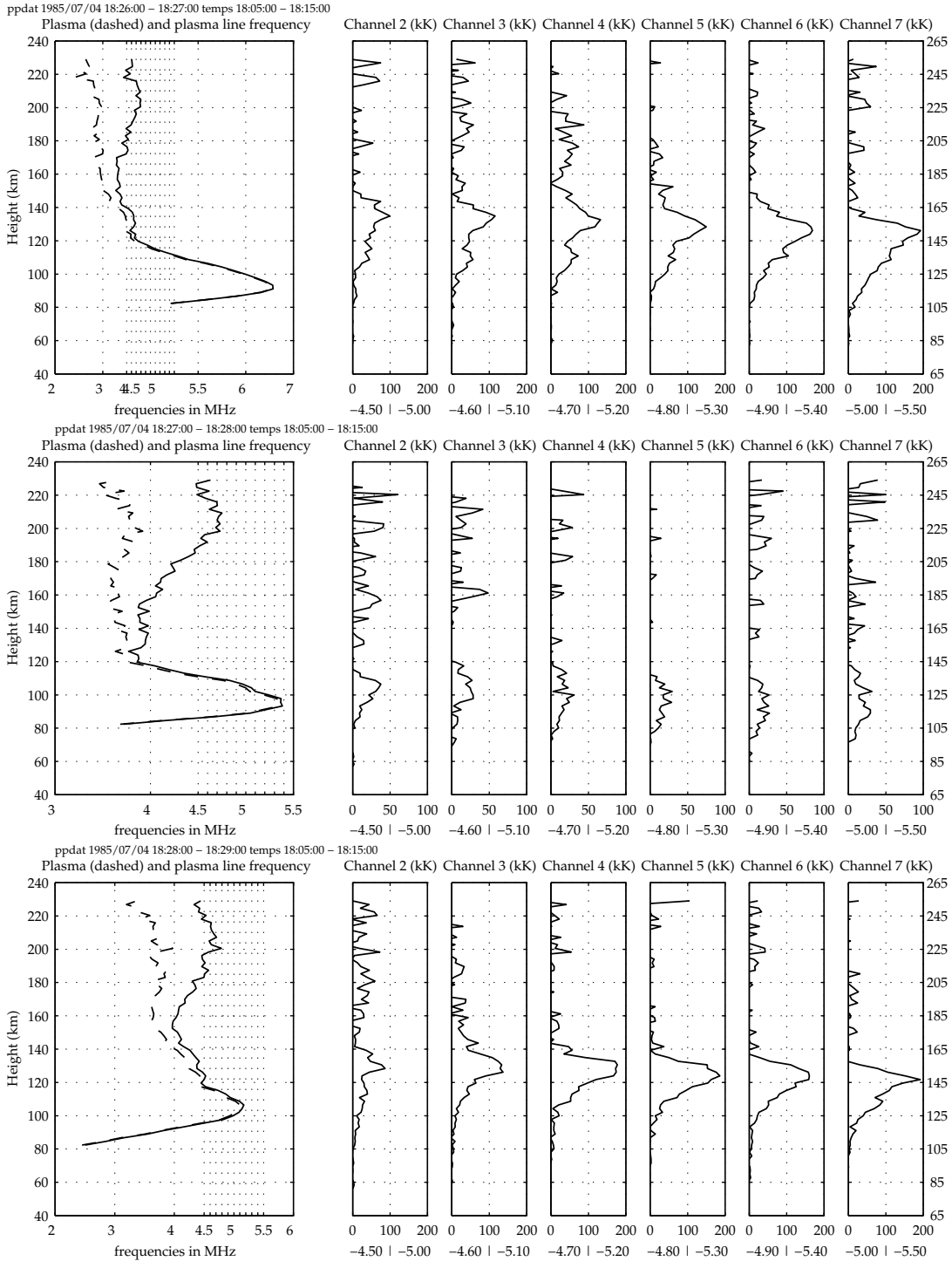

Figure 4.15: Plasma lines for the period 18:26 – 18:29. The temperatures used are from the period 18:05 – 18:15

a significant "bump" at sufficiently low velocity. In the production region, we expect an isotropic electron flux, and from the discussion in section 2.2.3, we know that an isotropic flux is stable. Even so, the suprathermal electrons can be increasingly mono- or bi-directional above the production region, and we could expect to see an electron-electron beam instability at these altitudes. In this case, we would expect enhanced plasma lines only above a minimum altitude, and with the enhancement increasing with height as the distribution becomes increasingly anisotropic. What we see is instead scattered power decreasing with altitude, and extending down into what is most likely the production region of secondary electrons.

4.5.2 Sporadic *E* layers

A phenomenon which has received considerable attention in ionospheric research and which has been studied extensively also with incoherent scatter radar is the sporadic *E* layer [e.g. *Behnke and Vickrey*, 1975; *Miller and Smith*, 1978; *Turunen et al.*, 1985, 1988; *Huuskonen et al.*, 1988*a*; *Jones*, 1989; *Nygrén*, 1989; *Nygrén et al.*, 1990]. The sporadic *E* layer is a thin 1–3 km layer of enhanced plasma density, usually occuring at altitudes of 90 to 140 km. Such layers are usually explained in terms of horizontal neutral winds and heavy, metallic ions, assumed to be of meteoric origin [*Huuskonen et al.*, 1988*a*]. At high latitudes, sporadic *E* layers can also be formed by auroral electric fields [*Turunen et al.*, 1985].

We have briefly considered whether the observations we have presented were due to a sporadic *E* layer. The possibility was dismissed, however, for two reasons. Firstly, the intensity observed in the scattered ion spectrum is an order of magnitude larger than what is customary in other sporadic *E* studies. Secondly, the layer we observed is much thicker than the 1 to 3 km mentioned above. The observed thickness is 20 km or more, more than sporadic *E* layers, even when the smearing from the 15 km range contributing to the scattering from the shortest pulse is taken into account.

4.5.3 Proton precipitation

The calculated enhancement of plasma lines from precipitating protons for the UHF radar in the *E* region is about 20. The observed enhancements are more than an order of magnitude greater than this, and so proton precipitation must be rejected as an explanation for our observations.

4.5.4 Suprathermal electron enhancement

The simple addition of a suprathermal population described by e.g. a power-law distribution is unable to explain the observations. Since the plasma lines observed are at offsets of 5.5 MHz and less, the power-law distribution should not be used in the first place. Apart from that, the enhancement is is much larger than one could expect from such a mechanism.

Taking properly into account the details of ionospheric electron fluxes and production of secondary electrons like the calculations of *Kirkwood et al.* [1995], much larger enhancement can be expected in the energy range 5.3 to 7 MHz because of the absorption of electron at these energies by N_2, and the resulting plateau in the one-dimensional electron distribution. See figure 2.3. Of course, our observations cover only a small part of this energy range. We do, however, see similar range distribution of the intense plasma lines as those reported by *Kirkwood et al.* [1995], although our observations are more concentrated at lower altitudes; below 160 km in the first event, and below 140 km in the second. Compare figures 4.4 and 4.11 with figure 5 of *Kirkwood et al.* [1995].

The indications are not conclusive. The intensities calculated have a maximum intensity at or just below 6 MHz offset for all the cases investigated, while we see plasma lines where maximum intensity decreases with offset (e.g. figure 4.8, top panel); is almost the same for all offsets (e.g. figure 4.13, bottom two panels) or more erratic behaviour. The maximum intensity in our observations is still ≈ 4.5 times higher than the ones calculated by *Kirkwood et al.* [1995], and ≈ 3 times higher than the observations cited in this article.

In this picture, the enhanced scattering from the ion spectrum is caused by the increase in electron density due to energetic electron precipitation, see e.g. figure 4.13.

4.6 Conclusions

We have observed two events where intense plasma lines are coupled with strongly enhanced raw electron densities. The peak of the raw electron density has been lowered to below 100 km, and we have seen narrow, single-humped ion spectra of unusual power. The plasma lines observed had temperatures up to 750 000 K, or 68 eV, three times more intense than previously reported observations, with 25 to 45 eV observed over several minutes.

The observations have many similarities with the observations reported by *Kirkwood et al.* [1995], and we find that an interpretation in terms of this enhancement mechanism is reasonable, although it can't explain all features of

the observations we have made. In particular, the variability of the intensity as a function of offset needs to be explained, as does the extra factor of five in the enhancement. Furthermore, *Kirkwood et al.* [1995] does not report unusually enhanced ion spectra together with the plasma line enhancement.

The most obvious conclusion is that an interesting observation has been made with an experiment less suited for understanding the physics of the phenomenon. A thorough understanding will only be possible through better observations, and for that a new experiment is needed. We will return to this matter in chapter 5.

Chapter 5

Design and implementation of a new experiment

Our experiences from analysing and interpreting the data from the experiment discussed in this thesis clearly suggest that the experiment was far from optimal for studying the phenomena we have observed. This is not surprising. The experiment was designed for a completely different purpose.

In this chapter we will review the criteria that need to be taken into account when designing an experiment tailor-made for the observation of phenomena like the ones observed accidentally in the experiment we've investigated.

As noted in section 4.5.2, the observed phenomena share many similarities with sporadic *E*, so our design will clearly benefit by inheriting properties from existing experiments made for such studies. A different phenomenon which is observed with high-resolution experiments at low altitudes is Polar Mesospheric Summer Echoes (PMSE). None of these experiments have, to our knowledge, looked for plasma lines in conjunction with *D*- and *E*-region studies. This means that a good design for our special purposes could also be used to shed more light on the phenomena of sporadic *E* and PMSE.

After a general discussion on the kinds of tradeoffs and compromises that must be made in the design regardless of the physical properties of the radar system, section 5.1, we will examine some of the experiments used in recent *E* region studies in section 5.2. This section is like a history of EISCAT experiment design, going through increasingly sophisticated multi-pulse modulations and leading up to the introduction of alternating codes to the EISCAT system.

After this brief review, we return in section 5.3.2 to the problem at hand; to construct an experiment incorporating modern experimental techniques like alternating codes into an experiment for high-resolution *E* region observations, while at the same time keeping the lessons of history in mind.

When we now know what we want to achieve with our program, we are ready to implement the design we've arrived at. We take a closer look at the signal processing hardware of the existing EISCAT radar system in section 5.4.1. We then describe the correlator program we have made for our experiment and finally we describe the experiment generation program which is used to create all the files necessary for an EISCAT experiment based on our design. In the hope that this experiment generation program and our correlator program can be of use for other experimenters as well, this section has been written almost like a user's guide, outlining the wide range of possibilities inherent in the design rather than immediately focusing on the realisation best suited for our purposes.

Finally, the possibility of realising the design on the EISCAT Svalbard Radar (ESR) is briefly considered. Although the hardware description for that system has appeared, very little experience has been made in programming that system. In addition, the problems with ground clutter has not yet been solved, and the hardware necessary for plasma line observations has not yet appeared. This section is therefore necessarily a bit sketchy.

5.1 Tradeoffs and compromises

There are several conflicting design requirements for experiments for low-altitude studies, and a tradeoff between the different requirements is inevitable. We will present some of the conflicting requirements and the tradeoffs between these.

5.1.1 Lag extent vs. low altitude coverage

As discussed previously, the correlation time of the plasma in the *E* region is often on the order of 300 μs or more. When observing this plasma, we would like to estimate the ACF of the plasma fluctuations out to the second zero crossing. This implies a modulation of at least 300 μs. Since we are transmitting and receiving on the same antenna, we cannot transmit and receive simultaneously. In fact, there is a minimum delay between the end of the transmission and the beginning of the reception. This minimum delay is 100 μs for the EISCAT mainland radar systems. For a plain power profile, estimating only the zero lag, this is not a serious limitation, since the length of the pulse needs to be comparable to the scale height of the ionosphere, and even a 10 km long pulse can be received in its entirety from an altitude of 35 km, well below any events observable by IS radar.

For ACF estimation, however, the lower edge of the observable range is determined by the total length of the modulation. The length of the modulation in turn limits the maximum lag at which the ACF of the plasma fluctuations can be estimated. The correlation time increases with decreasing altitude, so for a vertical antenna, the ACF becomes impossible to estimate with any accuracy below a certain altitude. This altitude is influenced, but not dominated by the minimum delay between transmission and reception. For a 400 μs modulation and a filter with a group delay τ_g of 10 μs, the minimum range is increased from 61.5 to 76.5 km because of the 100 μs delay.

Looking at it the other way, if we want a minimum range of, say, 80 km, we must choose a modulation of maximum

$$80/0.15 - 100 - \tau_g$$

or 423 μs. (0.15 km/μs is half the speed of light.) This is then the maximum lag extent we can monitor with our experiment.

5.1.2 Range resolution vs. time resolution

The range resolution of our experiment is defined by the length of the fundamental pulse; the bit in the Barker code or, if plain pulses are transmitted, the bit of the alternating code. On the other hand, the time resolution of the experiment is limited by the weak scattering from the plasma, which again is proportional to the transmitted power. For a transmitter of finite power, shorter pulses will mean less power scattered. This in turn means longer integration time and therefore lower time resolution.

The technique of Barker codes alleviates this situation to some extent, since the power transmitted is modulated such that it has an autocorrelation function which is only a bit wide, hence it "concentrates" the power of all the bits as if they were transmitted as a single bit-long pulse. The decoding of the Barker code is performed by a simple FIR filter, the coefficients of which is simply the sign sequence of the transmitted Barker code.

The "concentration" of the Barker code is not perfect, naturally. There are sidelobes in the ACF, and for Barker-coded multipulse experiments, these sidelobes can lead to stray signal from ranges very different from the main lobe of the signal. These effects are discussed in [*Huuskonen et al.*, 1988*b*], together with an (incomplete) technique for correcting for these effects in a particular experiment. With Barker-coded alternating code experiments, such effects are more localised. The ambiguity functions of Barker coded modulations are still very complicated, and taking this ambiguity properly into account is difficult, if not impossible, without a full profile analysis technique [*Farley*, 1969; *Lehtinen*, 1986; *Holt et al.*, 1992].

5.1.3 Range resolution vs. signal-to-noise ratio

Time resolution is, of course, inextricably coupled to signal-to-noise ratio. We shall see that the coding introduced to improve range resolution while keeping the time resolution introduces more noise into our receivers. If we're not careful, all the benefit of such codes might be lost.

The bandwidth of the signal we want to receive is small; from some kHz for the plasma line to some tens of kHz for the ion spectrum. The background noise, however is uniformly distributed over the entire spectrum. The noise on the same frequencies as our signal is inevitable, but for limiting the noise at other frequencies, we would like our receiver filters as narrow as possible. For short fundamental pulses, the bandwidth of the transmitted signal defines the lower limit on the bandwidth of the receiver filter. For instance, a $2\,\mu$s fundamental pulse has a height resolution of 300 m, but requires a filter with 500 kHz bandwidth, ten times larger than desired. The signal-to-noise ratio thus decreases with another order of magnitude.

5.1.4 Range resolution vs. lag resolution

When employing a 13-bit Barker code to increase the range resolution, the time required to transmit a single baud of the alternating code is a factor 14 greater than the bit length of the Barker code. Since the bit lenght of the Barker code determines the range resolution while the baud length of the alternating code determines the lag resolution, the lag resolution of any Barker coded modulation must necessarily be rather coarse, from $42\,\mu$s for a $3\,\mu$s bit length and upwards.

The problem is less serious with shorter Barker codes, but then the Barker code itself is less effective; the sidelobes are more significant.

The only way to keep a good lag resolution while increasing range resolution is to move to longer alternating codes. This of course means that the number of scans necessary for decoding increases. During highly dynamic situations these codes cannot be used.

5.2 Existing experiments for studies of the E region and sporadic E-layers

Before describing the new experiment design, we will review some of the existing experiments that have been used for similar purposes previously, especially the experiments used for sporadic E observations. Studying the prop-

erties of existing experiments tells us something about the limits of the radar system and also what we can expect to achieve with our new design. By studying old experiments we might also find tricks used to overcome limitations of the system, tricks we might exploit in our own design. Of course, none of these experiments are satisfactory for our purposes, since none of them have the capability to record plasma line signals. In addition, none of the older experiments (e.g. ESLA-T4, GEN6/12) use alternating codes, something we intend to do in our experiment.

The EISCAT radars were designed from the outset with an extensive multifrequency capability. Before the introduction of the GEN system of correlator programs, [*Turunen*, 1985, 1986], these capabilities were rarely, if ever, exploited anywhere near their full potential. One reason could have been failure to grasp the potential of the system, an other reason can have been the sheer difficulty of programming the correlators. Most programs designed in this era were fairly simple, using simple modulations on one or two frequencies. Furthermore, the gating algorithms used for longpulse modulations in this era were not very good. The experiment examined in this thesis is an example of the design of the first period of operation.

5.2.1 Multipulse code experiments and the GEN system

Multipulse codes, introduced in *Farley* [1972], provided a way of estimating longer lags of the autocorrelation function while keeping good heigth resolution. The idea was to transmit an irregularly spaced series of elementary (short or Barker-coded) pulses in pattern where no particular spacing occured more than once. From such a pattern, lags corresponding to each spacing in the pattern could be calculated with a range resolution corresponding to the length of the elementary pulse. The drawback of this method was the reduced total output power and the unwanted clutter from uncorrelated ranges. For some special combination of multipulse patterns, these patterns could be interlaced on different frequencies. This improved the rate of statistics somewhat, while the problem of clutter could not be solved.

While elegant on paper, programming the correlators and radar controllers to correctly extract ACFs from different multipulse patterns on several channels simultaneously turned out to be a daunting task. The solutions used were often *ad hoc*, and used an unreasonable amount of the limited correlator resources, such as registers and instructions (see section 5.4.1).

When the GEN system of correlator algorithms was released in [*Turunen*, 1985] together with a set of experiment design guidelines [*Turunen*, 1986], a much more efficient exploitation of the radar system was within reach of most experimenters, and many new experiments were designed and run based on

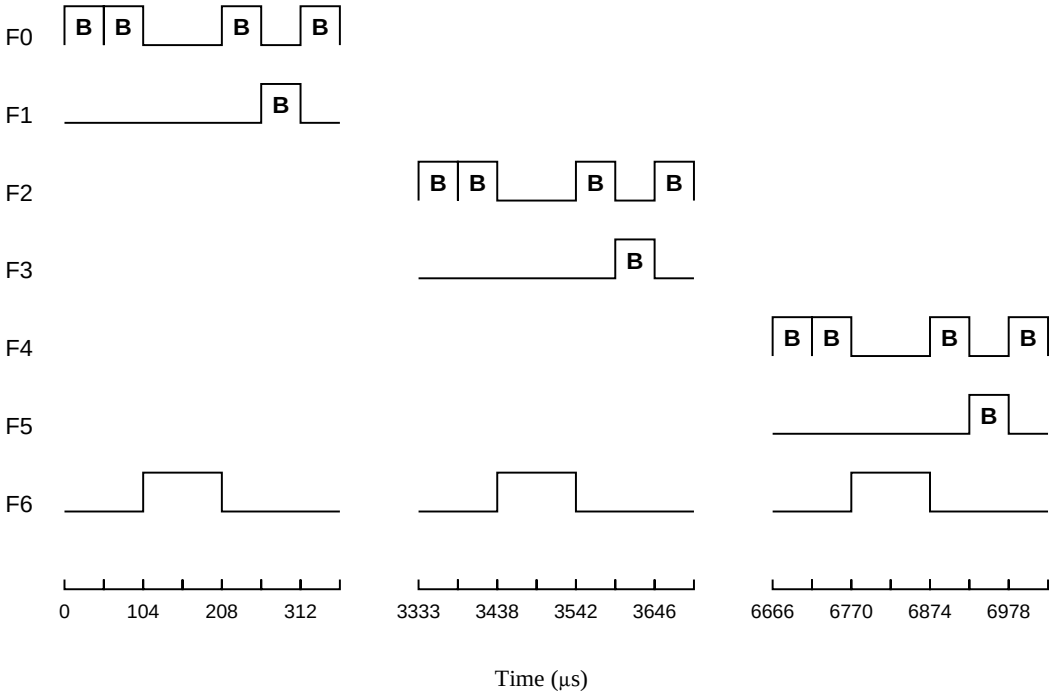

Figure 5.1: The ESLA-T4 modulation pattern. The transmissions marked **B** are coded with a 13-bit Barker code. Each subgroup is received before the next subgroup is transmitted. After [*Huuskonen et al.*, 1986]

this system. The GEN-system consists of a family of correlator algorithms for the common modulations; powerprofiles, longpulses and multipulse codes; and complete correlator programs written using these subroutines. These programs also include radar controller (TARLAN) and eros (ELAN) code which can be used with little or no modification. In exchange for the added utilisation of the radar, the GEN-system required the experimenter to adhere to some guidelines concerning the filling of the buffer and result memories.

One of the successful and popular experiments used for high-resolution *E*-region studies with the mainland EISCAT radar systems in the second half of the '80s is the ESLA-T4 modulation scheme. It was used by *Huuskonen et al.* [1986] for determining ion-neutral collision frequencies and for sporadic *E* studies by *Huuskonen et al.* [1988*a*] and by *Nygrén et al.* [1990].

The experiment ESLA-T4 is described in detail in [*Huuskonen et al.*, 1986]. It is composed of a four-pulse Barker-coded multipulse part providing lags 1 to 6 of the autocorrelation function, a single Barker-coded pulse for power profile (lag zero) and a long pulse received exclusively at the remote sites and used for measuring the electric field. A 13-bit Barker code with bit length 4 μs

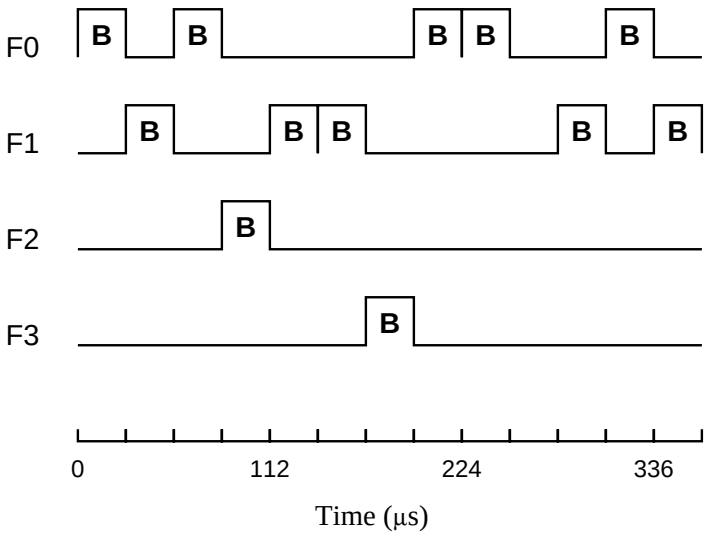

Figure 5.2: One subgroup in the GEN-1B modulation pattern. The pattern is repeated four times using eight different frequencies in such a way that each frequency contains one multipulse code and one short pulse. As in figure 5.1, each baud marked **B** are coded with a 13-bit Barker code, this time with a bit length of 2 μs. The results of all the pulses are added in the correlator.

is used for the multipulse and short pulse transmissions, giving a total baud length of 52 μs. The pattern has a basic spatial resolution of 600 m and provides correlating lags every 52 μs out to 312 μs, good enough for this altitude. The basic time resolution used in these experiments is 10 s.

In 1985, *Turunen et al.* presented observations using a four-pulse Barker-coded experiment with a spatial resolution of 450 m and time resolution of 15 s using a similar pattern with a bit length of 3 μs.

Finally, *Turunen et al.* [1988] reported observations using a pattern of two different Barker-coded five-pulse patterns and two Barker-coded single pulses interlaced with a bit length of 2 μs, giving a basic height resolution of 300 m. The maximum lag calculated by this modulation is 252 μs. This used the algorithm GEN-1B. This algorithm uses the radar exclusively for maximum resolution in the *E* layer, filling the time available for transmission completely, and it is therefore a strictly monostatic experiment.

Huuskonen et al. [1988*b*] analysed the range ambiguities introduced by the sidebands of the Barker code in the ESLA-T4 and present a correction method based on the range-reduced ambiguity function. They conclude that the experiment consistently overestimates the first lag of the ACFs, particularly above

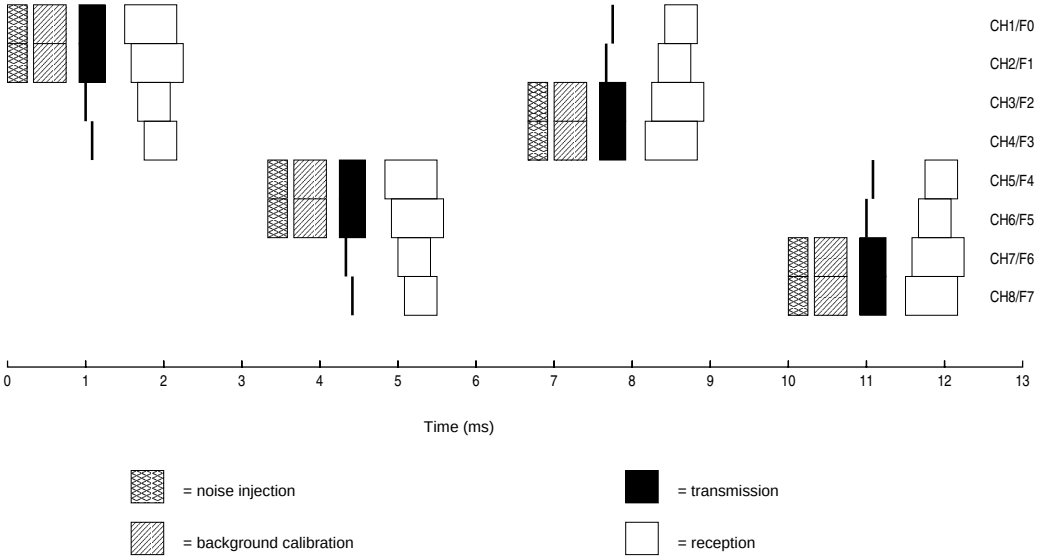

Figure 5.3: The GEN-1B modulation pattern. As can be seen from the figure, all eight available receiver channels are used for the program. Each transmission block (the group of black rectangles) is drawn in more detail in figure 5.2. After [*Turunen et al.*, 1988]

120 km. Other small improvements are also suggested. Codes incorporating these improvements have been constructed; these codes are named GEN-6 and GEN-12.

Forgetting the range ambiguities in this particular experiment for a moment, a problem with the multipulse codes is that they don't utilise the available transmitter duty cycle fully [*Sulzer*, 1986]. Interlacing several multipulse patterns as in the GEN-1B modulation described above improves the situation, but since the transmitter uses 1 μs (EISCAT mainland radars) to change transmitter frequency, gaps are introduced in the transmission. Furthermore, multipulse codes of more than four pulses will not provide estimates of all the lags, there will be gaps in the estimated ACFs. For instance, the five-pulse codes used in GEN-1B provide lags 1–9 and 11, while lag 10 is not available. (In this particular program, lag 11 is not computed, so only lags 1–9 are used.) An additional shortcoming of multipulse codes is that correlations, the individual estimates of the lags of the ACF, can only be computed between pulses transmitted on the same frequency.

5.2.2 Alternating codes and the G2 system

Alternating codes, first presented by Markku S. Lehtinen in 1986, address these problems. An alternating code is a series of phase-coded transmissions (called scans) on a single frequency in a pattern that allows the determination of all possible correlations between pairs of elementary pulses, thus providing the maximum theoretical number of estimates of every single lag. The theory of alternating codes and some related pieces of theory (i.e. the theory of ambiguity functions) is developed in [*Lehtinen*, 1986; *Lehtinen and Häggström*, 1987]. Alternating codes come in two varieties: weak alternating codes, where each baud of the code needs to be Barker-coded and the number of scans is equal to the number of bits in the code; and strong alternating codes where the bauds can be plain and the number of scans is twice the number of bits in the code. In both cases, the number of bits in the code is a power of 2. The code might be truncated as long as the number of scans is kept as if the full code was used. This allows codes of almost arbitrary length, although with relatively longer scan cycles.

At this point we should mention that there exists other types of codes — similar to alternating codes — that also aim at using the available duty cycle of the transmitter more completely while maintaining good spatial resolution and several independent estimates of the different lags of the ACFs. These codes are called random codes and the technique is called the coded long pulse (CLP) technique. [*Sulzer*, 1986, 1993]. In addition, code sets called *complementary codes* which obey conditions similar to those of alternating codes but with significantly shorter cycle lengths have been summarised by *Sulzer* [1989]. Only short complementary codes have been found. A summary of some of the statistical theory underlying random and alternating codes is given in [*Lehtinen and Huuskonen*, 1996] and the different codes are described in the references cited in that paper.

Recently, it was found that alternating codes have significant correlation between different lags at high signal-to-noise levels. A simple modification of the alternating code will address this problem [*Lehtinen et al.*, 1997]. These so-called randomised alternating codes cannot currently be used at the EISCAT mainland radars, but they might be used on the ESR in the near future.

Although quickly recognised as a useful technique to increase the resolution of incoherent scatter radars, especially under low signal-to-noise conditions, the correlators and radar controllers used at EISCAT did not have the capability of decoding the received signals. Alternating codes were not known at the time these were designed and built. The correlator algorithm UNIPROG, by T. Turunen, calculated all the cross products of the reception samples up to a specified lag. This was used for ACF estimation in multipulse experiments. By storing such matrices for each scan separately, the decoding could

be performed off-line after the experiment. The limited result memory of the correlators means that the number of range gates obtainable in this fashion is very limited, even an eight baud code can only calculate 32 range gates and a 16 baud code can have only eight range gates. Nevertheless, the technique was used by Turunen, Häggström and others in 1987. These codes were used in the ERRIS campaign in 1988 and produced scientifically significant data of excellent quality [*Häggström et al.*, 1990; *Williams et al.*, 1990; *Opgenoorth et al.*, 1990; *Jones et al.*, 1991]. One of these publications [*Häggström et al.*, 1990] describes the coding scheme used and also includes a comparison of the number of estimates available of the different lags from using alternating codes versus interlaced multipulse codes.

The good results achieved using alternating codes lead to the upgrade of correlators and radar controllers to enable real-time hardware decoding of alternating codes. The upgrade was performed in the period 1988–1991 and is described in [*Wannberg*, 1993] along with an intended replacement for or extension of the GEN-system, named G2. Also described are two experiments built from this system; a general purpose *E*- and *F*-layer experiment currently run with minor modifications as CP-1 and CP-2 and a Barker-coded experiment for *E*-region studies at 450 m resolution. The alternating code part of the former uses a 16-bit strong code with a bit length of 21 μs, while the latter, called MET2, uses an eight-bit code where each baud is coded with a 13-bit Barker code. Although this experiment could have used the weak condition, the hardware decoding is only programmed for strong condition alternating codes. The total modulation is therefore transmitted over 16 scans. This experiment has been run as a Swedish special program on several occations, and an example of data taken with this experiment is given in [*Wannberg*, 1993]. In both these experiments, long pulses for higher altitudes and power profile short pulses are also transmitted.

Sadly, the EISCAT technical note documenting the G2 System announced by *Wannberg* [1993], never materialised. The documentation for the system mostly consists of "look at the examples". The complexity of these examples, later coupled with the anticipation of the next generation of receiver hardware, has more or less stopped the development of new experiments. Nothing resembling the flurry of new experiments that followed the introduction of the GEN system ever appeared with G2. To our knowledge, the only experiment (apart from Wannberg's own experiments) constructed with G2 is the experiment used in [*Guio et al.*, 1996].

5.3 Design requirements

Since the experiment presented in chapter 3 is the only observation available of simultaneous strongly enhanced ion spectra and plasma lines, we have no observation base from which we can determine the design requirements of our experiment. Some guesswork will be necessary for the initial design. If any observations are made with this experiment, refinements can be made at a later stage.

5.3.1 The properties of sp-no-plasma3

- The experiment we have analysed consisted of two long pulses, one of 105 μs and one of 210 μs. This is inadequate for *E*-region studies. While the height resolution implied by a 105 μs-pulse — $\approx$ 16 km — is acceptable for the top *E*-region and lower *F*-region, it is much too coarse for meaningful results for the *E*-region itself, while the lag extent of maximum 105 μs is unable to resolve typical spectra at *E*-region altitudes. The power profiles of this pulse are taken at $\approx$ 3 km, while the pulse used for the power profile is more than five times as long, so there is significant overlap between the gates in all the power profiles. The 210 μs pulse is used only at altitudes well above the *E*-region.

- The experiment was designed such that plasma lines from two different pulses were received in the same channels at the same time. The time and frequency separation of the pulses was chosen such that downshifted plasma lines would be separated artificially in the channels when the Langmuir frequency increased with height. When the Langmuir frequency profile was inverted, the opposite effect was achieved — the pulses were brought together instead of separated.

- Only downshifted plasma lines were monitored. This is a direct consequence of the pulse scheme used. Whereas downshifted plasma lines were separated, upshifted plasma lines would have been brought together under normal conditions.

- The reception channels for plasma lines were moved about in frequency, thus covering more frequencies, albeit at the expense of losing continuity in the measurements at a particular frequency.

- The basic time resolution of the experiment was one minute, which is reasonable for a low duty cycle experiment like this one, but much less than expected of modern designs.

5.3.2 The design goals

For our new experiment, there are several (conflicting) goals we would like to aim for in our design. We will outline these goals with little or no consideration of hardware limitations. Later we will limit the goals to realisable designs, for the EISCAT mainland radars, and later the ESR.

- First and foremost, we need a good time- and range resolution ion spectrum ACF with sufficient lag resolution and -extent for ordinary to (moderately) inordinary *E*-region situations. This indicates a Barker coded alternating code coupled with a Barker coded short pulse for power profile measurements. The length and bit length of the two codes must be chosen such that the desired height resolution is achieved without losing the necessary lag extent.

  In table 5.1 we have summarised all possible combinations of 8-, 12-, 16- and 32-bit alternating codes, 13- 11- and 9-bit Barker codes and plain pulses and all bit lengths between 3 μs (determined by filter bandwidth) and 32 μs (determined by height resolution) which result in a total modulation length between 300 and 500 μs. In each case, a filter group delay equal to half the elementary pulse length is assumed.

  As we can see, for sub-kilometer range resolution, we must use a Barker-coded 8-, 12- or just possibly a 16-baud alternating code. If we accept lower range resolution and choose good lag resolution instead (something that might be necessary for resolving the spectra of plasma lines), we will need longer codes with plain pulses instead. In this case, the tradeoff will be between range/lag resolution and total lag extent.

- Furthermore, we need to receive plasma line signals. We would like to have spectra for the plasma lines at several different offsets; both up- and downshifted. The considerations of different modulations we made above hold here as well. We need one receiver channel for each offset monitored. Since the number of offsets will have to be limited, we would like to focus on the frequency range around 5 to 5.5 MHz in each direction. The frequency shift of the plasma line is expected to change rapidly with height in the *E*-region, so good height resolution is essential to avoid too much smearing in frequency.

- In order to connect events to the topside ionosphere, it is desirable to include a long pulse for *F*-layer observations. This will have to be secondary to the other observations.

A/C	B/C	Bit	Rg. res.	Filter BW	Lag res.	Lag ext.	min rg.
8 b	13 b	3 μs	450 m	333.3 kHz	42 μs	336 μs	116.02 km
8 b	13 b	4 μs	600 m	250.0 kHz	56 μs	448 μs	149.70 km
8 b	11 b	4 μs	600 m	250.0 kHz	48 μs	384 μs	130.50 km
8 b	11 b	5 μs	750 m	200.0 kHz	60 μs	480 μs	159.38 km
8 b	9 b	4 μs	600 m	250.0 kHz	40 μs	320 μs	111.30 km
8 b	9 b	5 μs	750 m	200.0 kHz	50 μs	400 μs	135.38 km
8 b	9 b	6 μs	900 m	166.7 kHz	60 μs	480 μs	159.45 km
12 b	11 b	3 μs	450 m	333.3 kHz	36 μs	432 μs	144.82 km
12 b	9 b	3 μs	450 m	333.3 kHz	30 μs	360 μs	123.22 km
12 b	9 b	4 μs	600 m	250.0 kHz	40 μs	480 μs	159.30 km
12 b	0 b	25 μs	3750 m	40.0 kHz	25 μs	300 μs	106.88 km
12 b	0 b	26 μs	3900 m	38.5 kHz	26 μs	312 μs	110.55 km
12 b	0 b	27 μs	4050 m	37.0 kHz	27 μs	324 μs	114.22 km
12 b	0 b	28 μs	4200 m	35.7 kHz	28 μs	336 μs	117.90 km
12 b	0 b	29 μs	4350 m	34.5 kHz	29 μs	348 μs	121.57 km
12 b	0 b	30 μs	4500 m	33.3 kHz	30 μs	360 μs	125.25 km
12 b	0 b	31 μs	4650 m	32.3 kHz	31 μs	372 μs	128.92 km
12 b	0 b	32 μs	4800 m	31.2 kHz	32 μs	384 μs	132.60 km
16 b	9 b	3 μs	450 m	333.3 kHz	30 μs	480 μs	159.22 km
16 b	0 b	19 μs	2850 m	52.6 kHz	19 μs	304 μs	107.62 km
16 b	0 b	20 μs	3000 m	50.0 kHz	20 μs	320 μs	112.50 km
16 b	0 b	21 μs	3150 m	47.6 kHz	21 μs	336 μs	117.38 km
16 b	0 b	22 μs	3300 m	45.5 kHz	22 μs	352 μs	122.25 km
16 b	0 b	23 μs	3450 m	43.5 kHz	23 μs	368 μs	127.12 km
16 b	0 b	24 μs	3600 m	41.7 kHz	24 μs	384 μs	132.00 km
16 b	0 b	25 μs	3750 m	40.0 kHz	25 μs	400 μs	136.88 km
16 b	0 b	26 μs	3900 m	38.5 kHz	26 μs	416 μs	141.75 km
16 b	0 b	27 μs	4050 m	37.0 kHz	27 μs	432 μs	146.62 km
16 b	0 b	28 μs	4200 m	35.7 kHz	28 μs	448 μs	151.50 km
16 b	0 b	29 μs	4350 m	34.5 kHz	29 μs	464 μs	156.38 km
16 b	0 b	30 μs	4500 m	33.3 kHz	30 μs	480 μs	161.25 km
16 b	0 b	31 μs	4650 m	32.3 kHz	31 μs	496 μs	166.12 km
32 b	0 b	10 μs	1500 m	100.0 kHz	10 μs	320 μs	111.75 km
32 b	0 b	11 μs	1650 m	90.9 kHz	11 μs	352 μs	121.42 km
32 b	0 b	12 μs	1800 m	83.3 kHz	12 μs	384 μs	131.10 km
32 b	0 b	13 μs	1950 m	76.9 kHz	13 μs	416 μs	140.78 km
32 b	0 b	14 μs	2100 m	71.4 kHz	14 μs	448 μs	150.45 km
32 b	0 b	15 μs	2250 m	66.7 kHz	15 μs	480 μs	160.12 km

Table 5.1: All possible combinations of alternating codes of 8, 12, 16 and 32 bits, Barker codes of 9, 11 or 13 bits or plain pulses, and bit lengths between 3 and 32 μs — corresponding to height resolutions between 450 m and 5 km — which gives modulations with a total length between 300 and 500 μs

5.4 An experiment for the EISCAT mainland radars

In this section, we present the realisation of our design in terms of an experiment for the existing EISCAT mainland radars. Since we hope and expect the design to be general and useful enough that it can be applied to different observational requirements than the ones presented by our phenomenon, we try to make this description broad enough to illustrate the potential of our design. The intention of this chapter is to serve as a "user's guide" for experimenters who want to use a realisation of our experiment design.

In order to understand the properties and limitations of the generated experiment, some background on the signal processing hardware — the correlators — is necessary. This is given in section 5.4.1. Section 5.4.2 takes a closer look at the internals of a correlator program. This should provide sufficient background to understand how the correlator program used in the design works, and also the comments on possible future developments.

After this, rather technical section, the correlator program used for our experiment design is presented in sections 5.4.3 and 5.4.4. The presentation includes a comparison with the program MET2 by Gudmund Wannberg which our program is based upon.

Finally, the experiment generation program is described in section 5.4.5, along with the input expected by the program and the files it generates.

We round off this chapter with some pointers into the future. Section 5.4.6 outlines the possibilities for using the experiment for observations in the immediate future, while section 5.4.7 hints at the improvements that might be possible in the correlator program.

5.4.1 The EISCAT correlators

The EISCAT correlators are quite remarkable. Designed and built in the late '70s to the early '80s, they were well ahead of their time. The design is a two-way superscalar (or rather VLIW) four-stage pipelined architecture running at 5 MHz, and where each stage of the pipeline is programmed separately in each instruction. The result is an amazingly powerful and flexible computer (for its application), but one that is not particularly easy to program. As a measure of the success of the design, we can mention that only recently have general-purpose workstations appeared with a sustained computing power matching the performance of the correlators. The correlators are described in a series of EISCAT Technical notes [*Alker*, 1979; *Ho*, 1981*a*,*b*; *Gras*, 1982]. Programming the correlators is described in detail in [*Törustad*, 1982], the GEN-system of correlator algorithms written in that language are described in detail in [*Turunen*,

1985, 1986]. More information on the correlators are also available in the references in all of these reports.

These computers, although powerful, are limited in several ways. There is memory for 16k of complex receiver samples — called the buffer memory — in each reception period. (there are two such buffer memories, used in a double-buffer scheme. One memory is written by the receiver while the other one is read by the correlator.) There are only 4095 memory locations for computed results — called the result memory. There are only 16 "permanent" registers within each of the address processors. Some of these are used by the algorithms as working registers, so only a limited number of these registers are available to the programmer and finally, there are only 64 locations of program memory. The correlator instruction format does not provide immediate operands, except that the number zero can be used as a result in each of the address processors. This means e.g. that one register in each address processor is occupied storing the number one!

There are three loop counters in the correlator, each with its associated loop counter register which holds the initial value of the loop counter. All conditional flow control instructions can only have conditions relating one or more loop counters to zero (equal to or not equal to) and only in certain combinations. Due to the pipelined design, there must be a one instruction delay between reloading the loop counter registers and assigning the reloaded value to a loop counter. The loopcounters can be reloaded from registers and/or decremented in any combination in every instruction *after* any tests have been made.

In addition, there are the data manipulation instructions for forming products of the different samples in the buffer memory or from the external bus. There is also provision for the accumulation of such products, called integration in EISCAT parlance. Although these instructions are the reason to have the correlators at all, these instructions are only used in the library subroutines; LONGPULSE, ALTCODE etc.

5.4.2 Overview of a correlator program

The correlator programming language, CORLAN, is really more like a symbolic assembly language than a programming language. It provides unlimited access to all parts of the system, and every operation which is to performed needs to be mentioned explicitly. There are some shortcuts and mnemonic aliases available. Furthermore, there is provision for symbolic constants. Since there are no immediate operands in the correlator instructions, this is only meaningful for register numbers in the register stacks of the address processors. CORLAN also provides named labels and symbolic names for the scratch

register in the address processors and the various latches and special purpose registers throughout the computer. Finally, there are symbolic names for some special operations related to decoding alternating codes, (DECODER), data transfer, (PREPARETRANSFER, TRANSFER), the state of various registers, (STROBE, LOAD, STORE) etc. CORLAN accepts comments, extending from a percent sign to the end of the line. The authoritative guide to CORLAN is [*Törustad*, 1982].

An instruction in a correlator program consists of these parts:

- An address for this instruction (NEXT or LOCATION=*nn*). Since an instruction consists of so many parts, it makes good sense to explicitly state the instruction borders.
- An optional label (LABEL or SUBROUTINE).
- Optionally reloading one of the loop counter registers (RELOAD and RELOADVALUE).
- APB instructions, accessing QAPB, BUFFERADDRESS and at most two references to the APB register stack.
- APM instructions, accessing QAPM, RESMEMADDRESS and at most two references to the APM register stack.
- Multiply and accumulate in two channels (real part and imaginary part.)
- Data flow and decoding instructions.
- Determining the address of the next instruction, can be conditional (GOTO, CALL, RETURN, GOTOANDPUSH, CONTINUE).
- Loading and/or decrementing loop counters, can be conditional.

Here is an example taken from the LONGPULSE subroutine of the GEN-system as it appears in the G2-experiments, e.g. G2-IV

```
NEXT
LABEL TRIANGLELOOP
BUFFERADDRESS=RSAPB(BMSTARTADD)
QAPB=BUFFERADDRESS
RESMEMADDRESS=RSAPM(WR1)+RSAPM(WR2)
QAPM=RESMEMADDRESS
CHANNEL1=OLDVALUE*X+OLDVALUE*Y
CHANNEL2=OLDVALUE*X-OLDVALUE*Y
STROBE IREG
```

```
LOAD IREG
STORE OREG
IF (LC1=0) THEN LC1=LCR1A ELSE LC1=LC1-1
IF (LC1=0) THEN CONTINUE ELSE GOTOANDPUSH ROWLOOP
```

(Note that the last two lines are confusing. The loop counter LC1 is not modified between the tests, and they are conceptually carried out in parallel.)

Often, though, experimenters don't need to get involved with programming the correlators at all. Since there are no immediate operands, all correlator programs are automatically parametrised. In many cases, all the experimenter needs to do is to identify and define these parameters. (Of course, they still need to make sure that the buffer memory contains the correct number of samples from the desired channel and modulation.)

Even when programming new correlator programs, subroutine libraries like GEN and G2 makes the construction of correlator programs easier than the above would seem to indicate.

As an example of this, here are the first few instructions from the G2-2 correlator program.

```
%%%%%%%%%%%%%%%%%%%%%%%%%%%%%%%%%%%%%%%%%%%%%%%%%%%%%%%%%%%%%%%%%%%%%%%%%%%%
%
% - compute LP (signal + background) part
NEXT
RSAPM(WR1)=RSAPM(LPSRES)
RELOAD LCR3       RELOADVALUE=RSAPB(NLPSG)
CALL LONGPULSE
%
%%%%%%%%%%%%%%%%%%%%%%%%%%%%%%%%%%%%%%%%%%%%%%%%%%%%%%%%%%%%%%%%%%%%%%%%%%%%
%
% - compute LP background (independent gates):
NEXT
RSAPM(WR1)=RSAPM(LPBRES)
RSAPB(WR1)=RSAPB(NLPBG)
CALL BGGATE
%
%%%%%%%%%%%%%%%%%%%%%%%%%%%%%%%%%%%%%%%%%%%%%%%%%%%%%%%%%%%%%%%%%%%%%%%%%%%%
%
% - compute LP noise injection (independent gates):
NEXT
RSAPM(WR1)=RSAPM(LPCRES)
RSAPB(WR1)=RSAPB(NLPCG)
```

```
CALL BGGATE
%
%%%%%%%%%%%%%%%%%%%%%%%%%%%%%%%%%%%%%%%%%%%%%%%%%%%%%%%%%%%%%%%%%%%%%%%%%%%%%%%
%
% - compute PP signal part
NEXT
RSAPM(WR1)=RSAPM(PPSRES)
RSAPB(WR1)=RSAPB(NPPSG)
CALL POWERCOMPUTE
%
%%%%%%%%%%%%%%%%%%%%%%%%%%%%%%%%%%%%%%%%%%%%%%%%%%%%%%%%%%%%%%%%%%%%%%%%%%%%%%%
%
% - save buffer address of altcode data before computing ACFs
NEXT
RSAPB(WR2)=RSAPB(BMSTARTADD)
CONTINUE
%
%%%%%%%%%%%%%%%%%%%%%%%%%%%%%%%%%%%%%%%%%%%%%%%%%%%%%%%%%%%%%%%%%%%%%%%%%%%%%%%
%
%      - call ALTCODE to process signal part of A/C data
NEXT
RSAPM(WR1)=RSAPM(ACSRES)
RELOAD LCR2      RELOADVALUE=RSAPB(NACSG)
CALL    ALTCODE
%
```

As we can see, this part of the program consists of loading the working registers in the APM and APB units and/or loopcounter registers (WR1, WR2, LCR2 and LCR3) with the parameters of the different subroutines and then calling the subroutines LONGPULSE, BGGATE, POWERCOMPUTE and ALTCODE. Programming new experiments can therefore be accomplished by using existing subroutines, but combining them in new ways.

5.4.3 A G2-experiment for the UHF

The G2-system builds upon the concept of virtual channels. The different modulations you want to use are rotated among the available physical receiver channels, while the transmissions switch to frequency to frequency. In a pure ion line experiment, there is no interference between the channels and the same signal should be seen in them all, so the results from the different channels are added on top of each other in the correlator result memory. Receiving

all scans of the same modulation on different channels means that the channels are automatically balanced.

In a plasma line experiment, we need to be very careful with the offsets between the different channels to avoid contamination between them. This is even more difficult since the frequency of the plasma line depends on the electron density, and we have no way of knowing in advance what frequency they will appear at, if at all. We will need the ability to move the frequency offsets of the plasma line channels if we want to track plasma lines in a dynamic environment. In short, it is necessary to dedicate receiver channels to plasma line measurements exclusively.

In the scheme we came up with, there are seven virtual channels; one longpulse channel, three A/C channels and three power profiles. Two of the A/C and power profile channels are intended for plasma line measurements. Each virtual channel occupies two physical channels, where one is used for signal and the other one is used for background determination and noise calibration within each subscan. The A/C ACFS and the power profiles are taken in the same physical channels and use the same calibration signal. The signal and background channels then change roles for the next subscan. Each subscan is split in three subcycles

1. The longpulse and the A/C scan is transmitted and received, the latter on three channels.

2. After a sufficient gap, the power profile short pulse is transmitted and received on three channels

3. The other four channels receive background and noise calibration

5.4.4 The epla1 correlator program

For the purpose of this experiment, we've developed a correlator program, called epla1 (for *E*-layer Plasma Line Alternating code, number 1). It is derived from the only existing Barker-coded alternating code experiment so far, Gudmund Wannberg's MET2, and shares some of this program's features. However, the desire to process plasma lines and the resources required for this processing means limiting some properties of the original experiment.

- MET2 records the degenerate (ambiguous) zero lag from the alternating code. This profile is used in variance estimation. No such calculation is done for epla1. In the correlator program for MET2, the combined operation of calling the subroutines for decoding the alternating code and

calculating the zero lag takes up five instructions of the nineteen available after all the necessary subroutines for alternating code, long pulse and power profile computations have been included. It is clear that this is too expensive to repeat even three times. In epla1, only signal gates are calculated for the alternating codes, but see below.

- MET2 takes two separate Barker code power profiles on two separate channels. Such power profiles are not expensive in terms of buffer memory, result memory or compute time; but they do require registers for indexing the memories and instructions to call the necessary subroutine. It turned out that even with the tricks employed to minimise the code, every single program location was filled, and thus the second power profile had to be left out.

In epla1, as in MET2, the Barker coding is optional. One of the parameters to the program, called DISPLACEMENT, indicates the displacement between samples of different bauds of one gate of the alternating code. For plain pulses, this parameter is one, while for Barker coded experiments, it is equal to the length of the Barker code plus one. No change is necessary in the correlator program.

Otherwise, the programs share the same GEN and G2 subroutines for alternating codes (ALTCODE), long pulses (LONGPULSE, BGGATE) and power profiles (POWERCOMPUTE); data dumping (GEN-SHORT-DUMP) and various small one- or two-instruction utility subroutines. To save space in identical calls to SKIPSAMPLES (which skips the garbage samples in the beginning of a Barker coded sample stream) and POWERCOMPUTE there was a utility routine called SKIPANDPC. A similar routine was constructed for the alternating code called SKIPANDAC. With one call to LONGPULSE, two to BGGATE (for background and calibration of the longpulse), three to SKIPANDAC and nine to SKIPANDPC, the instruction memory is completely full.

The program computes

1. Long pulse (signal+background) gates
2. Long pulse background gates
3. Long pulse calibration gates
4. Plasma line 1 A/C signal gates
5. Plasma line 1 PP (signal+background) gates
6. Plasma line 1 PP background gates

7. Plasma line 1 PP calibration gates
8. A/C signal gates
9. PP (signal+background) gates
10. PP background gates
11. PP calibration gates
12. Plasma line 2 A/C signal gates
13. Plasma line 2 PP (signal+background) gates
14. Plasma line 2 PP background gates
15. Plasma line 2 PP calibration gates

5.4.5 The experiment generation program

The radar controllers of the EISCAT mainland systems are programmable only in the loosest possible sense of the word. They have no control structures, no variables and no decision capability. The only thing it can be programmed to do is to turn on and off specific bits in its status word at a fixed time. With the complexity of Barker-coded alternating codes switched between different channels, writing such code by hand is unthinkable, not just because it would be extremely tedious, but also because errors would be inevitable. Furthermore, by careful programming of the experiment generation program, it can be made parameter driven, thus enabling a family of experiments to be created simply by changing the input parameters of the code.

As mentioned in section 5.4.1, the correlator program is already parametrised. The setting of the parameters is done by EROS, the EISCAT Real-Time Operating System. For the purpose of running experiments, the commands to EROS are provided in a file. Our experiment generation program calculates what the input parameters to the correlator program should be and generates the appropriate ELAN-file.

The experiment generation program was written in Perl [*Wall et al.*, 1995]. A lot of knowledge of the radar system is built into the program, such as minimum delay times, sizes of the various memories, the time required to write samples from specific channels to the buffer memory before calculation can start, and processor speeds and processing needs. We believe that this program will enable even casual users to tailor an *E*-region plasma line experiment to their own needs.

The experiment generated will have the following properties:

- It will have a long pulse part with signal, background and calibration gates. The parameters describing the long pulse are

  LPLEN The length of the pulse, in μs.

  LPFRANGE The range of the first LP gate, in km. The closest possible range will be used.

  LPADCINT The sampling interval of the ADC in the LP channels

  VOLINDEX The number of lag zero points added in each gate.

  The number of signal, background and calibration gates for the long pulse is defined by the parameters **NLPSG**, **NLPBG** and **NLPCG**, respectively.

- It will have a power profile part, also received in the plasma line channels, defined by the following parameters:

  BITLEN The length of the elementary pulse in μs. For a non-Barker coded experiment, this is the length of the entire pulse.

  BCLEN The length of the Barker code. The legal values of this parameter are 0 (meaning plain pulses), 7, 9, 11 and 13. It is still not certain whether other lengths than 0 and 13 can be used.

  PPFRANGE The range of the first PP point, in km. Currently, no attempt is being made to coordinate the ranges of the power profile with the alternating code gates. This will be done later.

  The number of signal, background and calibration gates for the power profile is defined by the parameters **NPPSG**, **NPPBG** and **NPPCG**, respectively.

- It will have an alternating code part, also received in the plasma line channels. The parameters **BITLEN** and **BCLEN** apply to the alternating code part as well as the power profile part. In this case, a **BCLEN** of zero indicates that the bauds of the alternating code are plain. In addition, this part uses the following parameters:

  ACLEN The length of the alternating code. The corresponding code sequence, as defined by the hardware decoder, is hard-wired into the program.

  DELTA The distance, in samples, between successive alternating code gates. To increase the range interval monitored without loosing range resolution, it might be desirable to calculate every Nth gate. Currently, **DELTA** can only be one. This is checked by the program.

The alternating code part is currently taken as low as allowed by the radar system. The number of alternating code signal gates is defined by the parameter **NACSG**. No background or calibration is taken for the alternating code.

- The final parameter of the experiment is called **PP_GAP** and is the number of microseconds between transmitting the alternating code and the power profile. If this interval is too short, spurious returns from the alternating code might contaminate the power profile. The program will complain about, but not disallow, such short intervals. By tuning the **PP_GAP** parameter, the experimenter can stretch the inter-pulse period to minimise idle time after the last complete scan in an integration period.

As an example, we have generated a plain-pulse experiment using a $16 \cdot 25\,\mu$s alternating code, $25\,\mu$s power profile and $240\,\mu$s long pulse. The timing diagram for that experiment (called `epla1_16`) is presented in figure 5.4.

When a parameter file containing all these parameters has been created, the program is run with (optionally) an argument `-t`, `-e`, `-g`, `-v` or `-l`, and the name of the parameter file. The optional argument specifies the generation of a `tlan`, `elan`, `gdef`, `vcinit.m` or `LP.m` file, respectively. The `tlan` and `elan` files contain radar controller (TARLAN) and EROS code. The `gdef` file contains data dump layout description for the real-time graph program used to monitor experiments while running. The `vcinit.m` file contains virtual channel definitions and the `LP.m` file contains lag profile definitions as MATLAB programs for use with GUISDAP.

Regardless of whether the optional parameter is specified, the program prints some generic information to standard error. The information printed includes the number of buffer memory samples used, the number of result memory locations used, estimated time needed for LP and AC calculations (the time required for PP calculations vanishes in this context), the time of a subscan and the number of complete cycles that will fit into a 10 s integration time. This enables tuning parameters without actually generating files.

EISCAT files

The generated files intended for the EISCAT radar system are

- The `elan` file, including the code to load the correlator and radar controllers with the correct programs, and the code necessary to set the different permanent registers in the correlator and the buffer memory mapping unit.

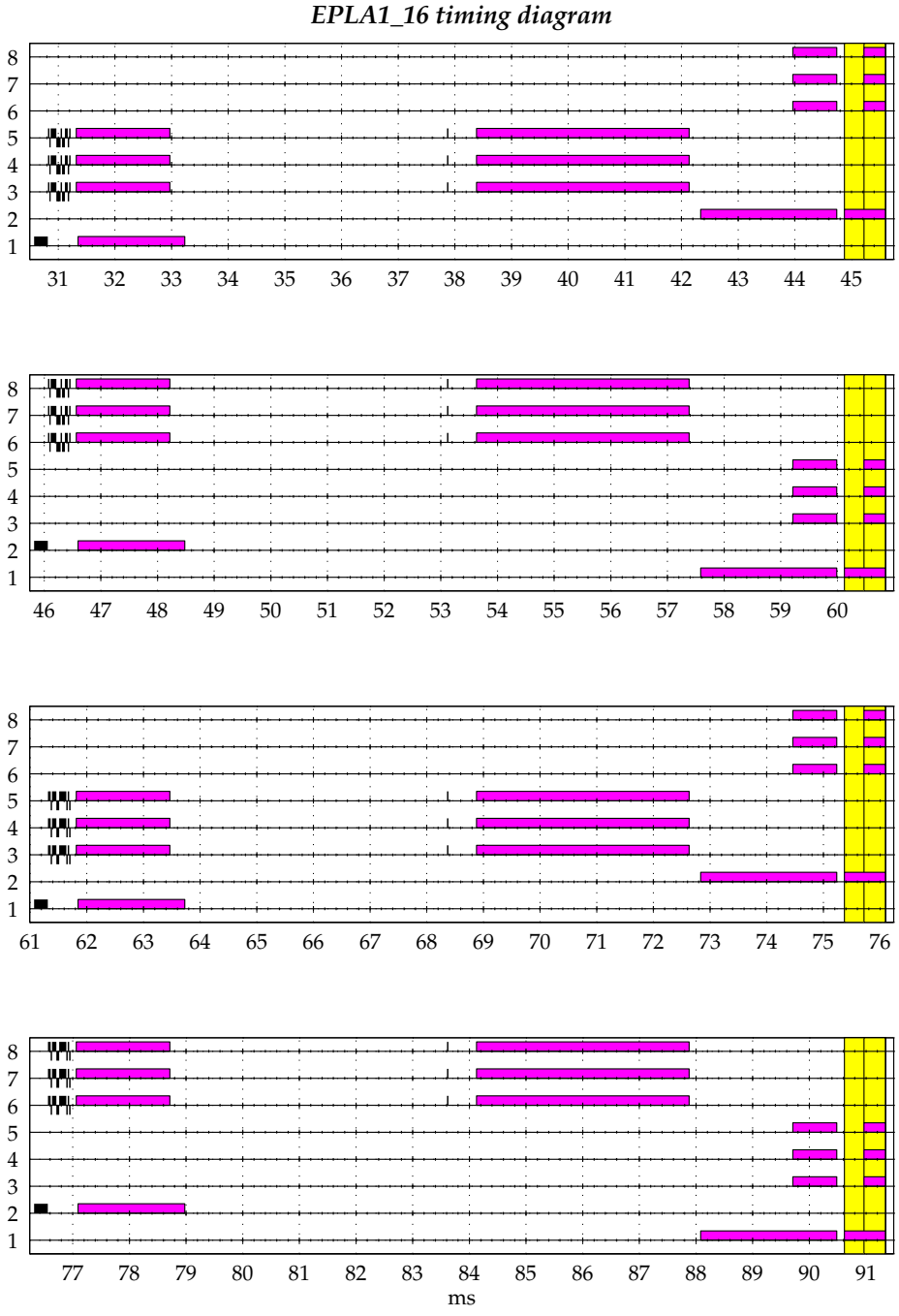

Figure 5.4: Timing diagram for epla1-16, second and third cycle. The long pulse is in channels 1 and 2 alternately, while the alternating codes and power profiles are in channels 3–5 and 6–8 alternately. Notice that the same scan of the alternating code is used in the two first subscans while a different scan is used for the next two subscans.

- The `tlan` file, which contains the transmitted modulations divided over the subscans and a final "padding cycle" which is needed to let the correlator process the final scan in the alternating code cycle before proceeding.
- In addition, the program can generate a `gdef` file which contains a description of the data which can be used by the real-time data monitoring program `rtg`. The file contains block definitions for all seven virtual channels and some window definitions.

The generated `elan` and `tlan` files are well commented, and include a header stating when it was generated and by whom and a summary of the properties of the experiment.

GUISDAP files

Before using GUISDAP for analysis of such an experiment, the grouping of signals and definition of the data must be made available in the form of GUISDAP variables. When designing experiments using GUISDAP's own design package, these variables are automatically initialised by GUISDAP. Generating these variables from `elan` and `tlan` files is mostly automated, but the layout of the data dump must be described in detail to GUISDAP since it makes no attempt at understanding correlator programs.

The initialisation of the GUISDAP variables is performed in several steps. First we run the program `tlan2ps`, either as a standalone program or as a routine linked into MATLAB, then we read the `tlan` and `elan` files to translate this into TX on/off, RX on/off and CAL on/off instructions that GUISDAP can understand. `tlan2ps` doesn't understand plasma line experiments. The generated instructions are a MATLAB m-file called *exp-name*`pat_PS.m` and a utility (MATLAB) function called `load_PS.m`. Loading these instructions is potentially time-consuming, particularly in MATLAB4, and the resulting MATLAB variables are therefore stored in a mat-file which can be loaded by MATLAB in an instant. With this information, a timing diagram like the one in figure 5.4 can be created.

Secondly, the virtual channels must be defined for GUISDAP. In GUISDAP parlance, a virtual channel is a single pulse or a group of pulses together with reception and optionally background and/or calibration. This is therefore different from the virtual channels of the G2 system. For simple one- or two-pulse experiments, there is one virtual channel per physical channel. If several modulations are transmitted on a single physical channel, one virtual channel must be defined for each of these. In the case of alternating code experiments, one

virtual channel must be defined for each physical channel in each subscan of each scan. Whereas we had seven G2 virtual channels in our experiment, we have fourteen GUISDAP virtual channels per scan, or 448 virtual channels for a 16-bit alternating code experiment. A virtual channel is defined by specifying which physical channel it is transmitted/received on, and the start/end time of that virtual channel. All transmitted pulses found within this interval will be taken to be a single modulation and treated together. This specification is performed in the file *exp-name*`vcinit.m`, which is called by the `init_KST` routine.

5.4.6 Planned observations

With the observation presented in chapter 4 being the only ones of this phenomenon, we don't expect it to be occuring with any regularity. An observational schedule for this phenomenon exclusively would therefore be potentially very expensive and with the risk of no or only a few new observations. Observation time can obviously be spent better elsewhere.

Occuring much more frequently and regularly are sporadic *E*-layers, typically at altitudes between 90 and 140 km [*Turunen et al.*, 1985, 1988; *Huuskonen et al.*, 1988*a*; *Nygrén et al.*, 1990]. To our knowledge, no attempt has been made to observe plasma lines in conjunction with sporadic *E*. An experiment using the design described above could provide new insights to the phenomenon of sporadic *E*, and an unusual phenomenon like the one we have analysed here should occur, that would be an extra bonus.

If we wish to push the observational envelope of the radar system even further, the experiment could be used to monitor Polar Mesospheric Summer Echoes, (PMSE) [see e.g. *Hoppe et al.*, 1988; *Röttger and La Hoz*, 1988; *Risbeth et al.*, 1988]. These have typically been observed at or close to 85 km. Plasma line observations have never been made or attempted together with PMSE observations, and any results will be highly valuable.

For both sporadic *E* and PMSE, the above experiment is not as finely-tuned for ion spectrum observations as for instance ESLA-T4 or MET2. Providing plasma line observations naturally demands resources that could otherwise be spent on the ion spectrum. The added information from the plasma lines should still be an advantageous trade.

As a final possibility, observation time could be granted under UP (Unusual Program) terms; that is, if an interesting situation appeared to develop during a common program, this program could be interrupted for up to an hour and the unusual program run in its place. Such an arrangement could provide the best possible coverage at the least cost in observation time, although at the great risk of not observing the initial phase of any situation that should arise.

5.4.7 Future developments

Currently, one register is unused in each of the address processors in the correlator. With no instructions to spare, these cannot be used. If the three calls to SKIPANDPC (for signal, background and calibration) are combined, six instructions, two APB registers and two APM registers will be available. Since there are garbage samples in the beginning of each Barker coded powerprofile, this will result in (BCLEN − 1) garbage gates between the signal and background gates and between the background and calibration gates. For non-Barker coded power profiles there is no overlap. Thus, the resulting data will be exactly the same - there will be no "garbage gates."

We also imagine it possible to combine two operations in the SKIPANDAC to ALTCODE transition. This will have to be confirmed.

The current correlator program, epla1, uses certain resources to provide for Barker-coded alternating codes. If plain pulses are used, these resources could be spent elsewhere. In particular, one APB register is used for the Barker code length and a total of six instructions of 64 are used for skipping "garbage" samples in the beginning of a Barker coded sample stream.

To summarise, improvements are possible, but we believe that the current correlator program has the power and flexibility necessary for a useful experiment which will enable scientifically significant observations.

5.5 An experiment for the ESR

The EISCAT Svalbard Radar (ESR) system is described in [*Wannberg et al.*, 1997]. Detailed as this description is, it is still difficult to provide anything more than a sketch of what the realisation of an experiment design will look like. Although *Wannberg et al.* [1997] claims that the receiver chains for the plasma lines "will be added in 1997", they haven't been installed as of this writing. The programming of the signal processing hardware is possibly even more convoluted than in the existing correlators. Only two experiments have been created for use with the ESR, and only one of these is currently in use. The experiments are

gup0 which is a long-pulse experiment for *F*-region studies, ranging from 150 to 550 km, using four plain long pulses, three of 360 μs length and one of 150 μs length. This experiment is routinely used in regular operation of the ESR.

gup1 is an alternating-code experiment for *E*-region studies together with a long-pulse part for *F*-region studies. This experiment has been run on

some occasions, but due to problems with ground clutter, it is not being run at the moment.

One big difference between the mainland EISCAT radars and the ESR in the case of long pulses is that the latter stores its raw data in the form of a lag profile matrix reminescent of the UNIPROG matrices of yore, whereas the former usually forms range gates from the different cross products to reduce the total amount of data. In the case of alternating codes, the difference is less apparent, since alternating codes add the lagged cross products of the samples (which contain range ambiguities) in such a way that the range ambiguities cancel out at all ranges but one in a complete cycle, and the sums of the different lagged products contribute to a specific lag and range.

The "correlator" on one (currently the only one) of the receiver chains of the ESR consists of a VME-board with two Texas Instruments TMS320C40 Digital signal processors (DSP), called C40 for short. The C40 is described in [*Texas Instruments*, 1992]. Released in 1991, the C40 is a pipelined floating-point DSP which runs at up to 50 MHz clock frequency. The C40 is designed with signal processing applications in mind; it contains parallell instructions for pipelined multiply-and-accumulate in every clock, and a no-overhead inner loop. It is therefore well suited for FIR applications. The C40 also sports a wide range of addressing modes (including a bit-reversed addressing mode for base 2 FFTs!), hardware floating-point multiply and divide instructions, 512 B of on-chip cache controllable by the programmer and 8 kB of on-chip memory. The two DSPs are mounted on the board in such a way that one of them can access the input (the samples from the six channel boards) and the other one can write the result memory. The work is therefore split between the processors such that one calculates the complex lagged products, while the other one forms autocorrelation coefficient estimates and integrates the result. Any decoding of alternating codes is performed in the server.

Each receiver chain on the ESR has a total available bandwidth of ≈ 4 MHz with a variable center frequency. One is installed, and two more will be installed shortly, one for each of the plasma lines. An offset of, say, 3 to 7 MHz, can then be monitored in each plasma line.

The Svalbard radar, when installed with the new receiver chains, has far more storage space available for resulting raw data; furthermore, it has separate processing units for the ion spectrum and each of the plasma line units. Thus, neither result memory size or processing time is expected to present limitations like the ones experienced on the UHF system. Furthermore, the early digitalisation of the signal in the ESR receivers reduces the problem of balancing and inter-calibrating the channels. We therefore expect to be able to construct an experiment of greater potential for use with the ESR. When the receivers of the

mainland systems are upgraded to match the Svalbard system, this realisation of the experiment design can be put to use on those radars as well.

Appendix A

Definitions and constants

A.1 Some fundamental definitions of plasma physics

Obviously, the definitions of plasma physics can be found in any textbook on the subject, such as [*Krall and Trivelpiece*, 1973]. Plasma physics has traditionally used the cgs system of units, but lately the use of SI units has become more common. Witness, for instance, how *Chen* [1984], uses SI units, while the first edition of that work used cgs units. Furthermore, plasma physicists use temperatures with or without Boltzmann's constant, energies in electron volts or other energies etc. By presenting the definitions we use in the text here, we hope to reduce the potential confusion as much as possible.

- The *gyrofrequency*, or *cyclotron frequency* is given by

$$\Omega_\alpha = \frac{q_\alpha B}{m_\alpha} \tag{A.1}$$

  This definition depends only on the magnetic field, and is valid as long as the magnetic field doesn't change significantly on length scales comparable to the gyroradius (or Larmor radius) $r_L = v_\perp m_\alpha / q_\alpha B$ nor on time scales comparable to one period of gyration.

- 0th moment; density of species α:

$$n_\alpha = \int f_\alpha(\boldsymbol{v})\, d\boldsymbol{v} \tag{A.2}$$

  This definition is obviously valid regardless of the distribution function f.

- The plasma frequency

$$\omega_{p\alpha}^2 = \frac{n_\alpha q_\alpha^2}{m_\alpha \varepsilon_0} \tag{A.3}$$

This definition only depends on density, and is universally valid.

- 1st moment; drift velocity:

$$n_\alpha \boldsymbol{v}_\alpha = \int \boldsymbol{v} f_\alpha(\boldsymbol{v})\, d\boldsymbol{v} \tag{A.4}$$

- 2nd moment; temperature (energy):

$$\frac{3}{2} T_\alpha = \frac{1}{2} m_\alpha \int \|\boldsymbol{v} - \boldsymbol{v}_\alpha\|^2 f_\alpha(\boldsymbol{v})\, d\boldsymbol{v} \tag{A.5}$$

Here, temperature is defined through the second moment of the distribution. Notice that we have defined temperature in units of energy, so Boltzmann's constant will not appear in this text. When defining temperature from (A.5), the thermal velocity appears as a parameter in the distribution function, and the relation between temperature and thermal velocity is given by (A.5).

We define the one-dimensional distribution by

$$F_\alpha(u) = \int f_\alpha(\boldsymbol{v}) \delta\left(u - \frac{\boldsymbol{k}\cdot\boldsymbol{v}}{k}\right) d\boldsymbol{v}. \tag{A.6}$$

Here, u is a projection of $\boldsymbol{v}$ along $\boldsymbol{k}$, and F is the projection of f. For one-dimensional distributions, the temperature is defined as

$$T_\alpha = m_\alpha \int_{-\infty}^{\infty} (u - u_\alpha)^2 F_\alpha(u)\, du \tag{A.7}$$

where u_α is the component of $\boldsymbol{v}_\alpha$ along $\boldsymbol{k}$.

For problems with a preferred direction, we define parallel and perpendicular temperatures by

$$\frac{1}{2} T_{\alpha\parallel} = \frac{1}{2} m_\alpha \int v_\parallel^2 f_\alpha(\boldsymbol{v})\, d\boldsymbol{v} \tag{A.8}$$

and

$$T_{\alpha\perp} = \frac{1}{2} m_\alpha \int v_\perp^2 f_\alpha(\boldsymbol{v})\, d\boldsymbol{v} \tag{A.9}$$

- The Debye length for species α:

$$\lambda_{D\alpha}^2 = \frac{\varepsilon_0 T_\alpha}{n_\alpha q_\alpha^2} \tag{A.10}$$

This definition needs the temperature and density as defined above.

References

Alker, H.-J. *A programmable correlator module for the EISCAT radar system*. Technical Report 79/11, EISCAT Scientific Association, Kiruna, Sweden, 1979.

Behnke, R. A. and J. F. Vickrey. Radar evidence for Fe^+ in a sporadic-*E* layer. *Radio Science*, *10*, 325–327, 1975.

Bjørnå, N. Derivation of ion-neutral collision frequencies from a combined ion line/plasma line incoherent scatter experiment. *J. geophys. Res.*, *94*(A4), 3799–3804, 1989*a*.

Bjørnå, N. Effects of suprathermal particles on the plasma lines. In *La Hoz and Brekke* [1989], pages 7–30, 1989*b*.

Bjørnå, N., O. Havnes, J. O. Jensen, and J. Trulsen. Enhancement of the incoherent scattering plasma lines due to precipitating protons and secondary electrons. *Phys. Scripta*, *25*, 632–636, 1982.

Bjørnå, N. and S. Kirkwood. Observations of natural plasma lines in the *E* region and lower *F* region with the EISCAT UHF radar. *Ann. Geophysicae*, *4*(A2), 137–144, 1986.

Bjørnå, N. and S. Kirkwood. Derivation of ion composition from a combined ion line/plasma line incoherent scatter experiment. *J. geophys. Res.*, *93*(A6), 5787–5793, 1988.

Bjørnå, N. and J. Trulsen. Effect of a power law particle flux on the ionospheric incoherent scattering cross section. *Phys. Scripta*, *33*, 284–288, 1986.

Brekke, A., editor. *Radar Probing of the Auroral Plasma*. Universitetsforlaget, Oslo, 1977. ISBN 82-00 02421-0.

Buchert, S. and C. La Hoz. Occurence of an ion-ion two-stream driven wave mode in the ionosphere. *Adv. Space Res.*, *17*(10), 235–240, 1996.

Cairns, R. A. *Plasma Physics*. Blackie, Glasgow and London, 1985. ISBN 0-216-91783-2.

Carlson, Jr., H. C., V. B. Wickwar, and G. P. Mantas. The plasma line revisited as an aeronomical diagnostic: suprathermal electrons, solar EUV, electron-gas thermal balance. *Geophys. Res. Lett.*, *4*(12), 565–567, 1977.

Chen, F. F. *Introduction to Plasma Physics and Controlled Fusion*. Plenum Press, New York and London, 1984. ISBN 0-306-41332-9.

Cicerone, R. J. photoelectrons in the ionosphere: Radar measurements and theoretical computations. *Rev. Geophys. Space Phys.*, *12*(2), 259–271, 1974.

Cicerone, R. J. and S. A. Bowhill. photoelectron fluxes in the ionosphere computed by a Monte Carlo method. *J. geophys. Res.*, *76*(34), 8299–8317, 1971.

Collis, P. N., I. Häggström, K. Kaila, and M. T. Rietveld. EISCAT radar observations of enhanced incoherent scatter spectra; their relation to red aurora and field-aligned currents. *Geophys. Res. Lett.*, *18*(6), 1031–1034, 1991.

Doering, J. P., W. G. Fastie, and P. D. Feldman. Photoelectron excitation of N_2 in the day airglow. *J. geophys. Res.*, *75*(25), 4787–4802, 1970.

Dougherty, J. P. and D. T. Farley. A theory of incoherent scattering of radio waves by a plasma. *Proc. Roy. Soc.*, *A 259*, 79–99, 1960. part 1 of a series of articles.

Dougherty, J. P. and D. T. Farley. A theory of incoherent scattering of radio waves by a plasma: 3. scattering in a partly ionized gas. *J. geophys. Res.*, *68*(19), 5473–5486, 1963.

Farley, D. T. A theory of incoherent scattering of radio waves by a plasma: 4. the effect of unequal ion and electron temperatures. *J. geophys. Res.*, *71*(17), 1966.

Farley, D. T. Incoherent scatter correlation function measurements. *Radio Science*, *4*(10), 935–953, 1969.

Farley, D. T. Multiple-pulse incoherent-scatter correlation function measurements. *Radio Science*, *7*(6), 661–666, 1972.

Farley, D. T., J. P. Dougherty, and D. W. Barron. A theory of incoherent scattering of radio waves by a plasma, II. scattering in a magnetic field. *Proc. Roy. Soc.*, *A 263*, 238, 1961.

Fejer, J. A. Scattering of radio waves by an ionized gas in thermal equilibrium. *Can. J. Phys.*, *38*, 1114–1133, 1960.

Fejer, J. A. Scattering of radio waves by an ionized gas in thermal equilibrium in the presence of a uniform magnetic field. *Can. J. Phys.*, *39*, 716–740, 1961.

Folkestad, K., T. Hagfors, and S. Westerlund. EISCAT: An updated description of technical characteristics and operational capabilities. *Radio Science*, *18*, 867–879, 1983.

Forme, F. R. E. A new interpretation on the origin of enhanced ion acoustic fluctuations in the upper ionosphere. *Geophys. Res. Lett.*, *20*(21), 2347–2350, 1993.

Foster, J. C., C. del Pozo, K. Groves, and J.-P. St.-Maurice. Radar observations of the onset of current driven instabilities in the topside ionosphere. *Geophys. Res. Lett.*, *15*(2), 160–163, 1988.

Frahm, R. A., J. D. Winningham, J. R. Sharber, and R. Link. The diffuse aurora: A significant source of ionization in the middle atmosphere. *J. geophys. Res.*, *102*(D23), 28, 1997.

Frank, L. A., N. A. Saflekos, and K. L. Ackerson. Electron precipitation in the postmidnight sector of the auroral zones. *J. geophys. Res.*, *81*(1), 155–167, 1976.

Fredriksen, Å., N. Bjørnå, and T. L. Hansen. First EISCAT two-radar plasma line experiment. *J. geophys. Res.*, *94*(A3), 2727–2731, 1989.

Fried, B. D. and S. D. Conte. *The Plasma Dispersion Function*. Academic Press, New York, 1961.

Gordon, W. E. Incoherent scattering of radio waves by free electrons with applications to space exploration by radar. *Proc. Inst. Radio Engrs.*, *46*, 1824, 1958.

Gras, R. *The EISCAT Correlator*. Technical Report 82/34, EISCAT Scientific Association, Kiruna, Sweden, 1982.

Guio, P., N. Bjørnå, and W. Kofman. Alternating-code experiment for plasma-line studies. *Ann. Geophysicae*, *14*, 1473–1479, 1996.

Hagfors, T. Density fluctuations in a plasma in a magnetic field, with applications to the ionosphere. *J. geophys. Res.*, *66*(6), 1699–1712, 1961.

Hagfors, T. The scattering of E.M. waves from density fluctuations in a plasma. In *Brekke* [1977], pages 15–28, 1977. ISBN 82-00 02421-0.

Hagfors, T., W. Birkmayer, and M. P. Sulzer. A new method for accurate ionospheric electron density measurements by incoherent scatter radar. *J. geophys. Res.*, *89*, 6841–6845, 1984.

Hagfors, T. and R. A. Brockelman. A theory of collision dominated electron density fluctuations in a plasma with applications to incoherent scattering. *Phys. Fluids*, *14*(6), 1143–1151, 1971.

Hagfors, T. and M. S. Lehtinen. Electron temperature derived from incoherent scatter radar observations of the plasma line frequency. *J. geophys. Res.*, *86*(A1), 119–124, 1981.

Hanssen, A., E. Mjølhus, D. F. DuBois, and H. A. Rose. Numerical test of the weak turbulence approximation to ionospheric langmuir turbulence. *J. geophys. Res.*, *97*(A8), 12073–12091, 1992.

Hasegawa, A., K. Mima, and M. Duong-van. Plasma distribution function in a suprathermal radiation field. *Phys. Rev. Letters*, *54*(24), 2608–2610, 1985.

Heinselman, C. J. and J. F. Vickrey. On the spectral analysis and interpretation of incoherent scatter plasma line echoes. *Radio Science*, *27*(2), 221–230, 1992.

Häggström, I., H. Opgenoorth, P. J. S. Williams, G. O. L. Jones, and K. Schlegel. Application of alternating codes for EISCAT observation during the ERRIS campaign for *E*-region plasma irregularities. *J. atmos. terr. Phys.*, *52*(6–8), 431–438, 1990.

Ho, T. *Instruction Manual for EISCAT Digital Correlator (Revised)*. Technical Report 81/26, EISCAT Scientific Association, Kiruna, Sweden, 1981*a*.

Ho, T. *Standard Subroutines and Programs for EISCAT Digital Correlator*. Technical Report 81/27, EISCAT Scientific Association, Kiruna, Sweden, 1981*b*.

Holt, J. M., D. A. Rhoda, D. Tetenbaum, and A. P. van Eyken. Optimal analysis of incoherent scatter radar data. *Radio Science*, *27*(3), 435–447, 1992.

Hoppe, U.-P., C. Hall, and J. Röttger. First observations of summer polar mesospheric backscatter with a 224 MHz radar. *Geophys. Res. Lett.*, *15*(1), 28–31, 1988.

Hubert, D. Non-Maxwellian velocity distribution functions and incoherent scattering of radar waves in the auroral ionosphere. *J. atmos. terr. Phys.*, *46*(6/7), 601–611, 1984.

Huuskonen, A., T. Nygrén, L. Jalonen, N. Bjørnå, T. L. Hansen, A. Brekke, and T. Turunen. Ion composition in sporadic *E* layers measured by the EISCAT UHF radar. *J. geophys. Res.*, *93*(A12), 14603–14610, 1988*a*.

Huuskonen, A., T. Nygrén, L. Jalonen, T. Turunen, and J. Silén. High resolution EISCAT observations of the ion-neutral collision frequency in the lower *E*-region. *J. atmos. terr. Phys.*, *48*(9–10), 827–836, 1986.

Huuskonen, A., P. Pollari, T. Nygrén, and M. S. Lehtinen. Range ambiguity effects in Barker-coded multipulse experiments with incoherent scatter radars. *J. atmos. terr. Phys.*, *50*(4/5), 265–276, 1988*b*.

Jones, B., P. J. S. Williams, K. Schlegel, T. Robinson, and I. Häggström. Interpretation of enhanced electron temperatures measured in the auroral *E*-region during the ERRIS campaign. *Ann. Geophysicae*, *9*, 55–59, 1991.

Jones, K. L. Mechanisms for vertical separation of ions in sporadic-*E* layers. *J. atmos. terr. Phys.*, *51*(6), 469–476, 1989.

Kikuchi, K., J.-P. St.-Maurice, and A. Barakat. Monte Carlo computations of *F*-region incoherent radar spectra at high latitudes and the use of a simple method for non-Maxwellian spectral calculations. *Ann. Geophysicae*, *7*(2), 183–194, 1989.

Kirkwood, S., H. Nilsson, J. Lilensten, and M. Galand. Strongly enhanced incoherent-scatter plasma lines in aurora. *J. geophys. Res.*, *100*(A11), 21343–21355, 1995.

Knudsen, W. C. Latitudinal variation of differential photoelectron flux at 560 km altitude. *J. geophys. Res.*, *77*(7), 1233–1241, 1972.

Kofman, W. and G. Lejeune. Determination of low-energy photoelectron distribution from plasma line measurements at Saint Santin. *Planet. Space Sci.*, *28*, 661–673, 1980.

Kofman, W., J.-P. St.-Maurice, and A. P. van Eyken. Heat flow effect on the plasma line frequency. *J. geophys. Res.*, *98*, 6079–6085, 1993.

Kofman, W. and V. B. Wickwar. Plasma line measurements at chatanika with high-speed correlator and filter bank. *J. geophys. Res.*, *85*, 2998–3012, 1980.

Krall, N. A. and A. W. Trivelpiece. *Principles of Plasma Physics*. Mc Graw-Hill, New York, 1973.

La Hoz, C. and A. Brekke, editors. *Proceedings of the EISCAT summer school*. Technical Report 89/50, EISCAT Scientific Association, Kiruna, Sweden, 1989.

Landau, L. D. On the vibrations of the electronic plasma. *J. Phys. USSR*, *10*(25), 574, 1946. In russian.

Lehtinen, M. S. *Statistical theory of incoherent scatter measurements*. Technical Report 86/45, EISCAT Scientific Association, Kiruna, Sweden, 1986. Ph. D. Thesis, University of Helsinki, Helsinki, Finland.

Lehtinen, M. S. and I. Häggström. A new modulation principle for incoherent scatter measurements. *Radio Science*, *22*(4), 625–634, 1987.

Lehtinen, M. S. and A. Huuskonen. General incoherent scatter analysis and GUISDAP. *J. atmos. terr. Phys.*, *58*(1–4), 435–452, 1996.

Lehtinen, M. S., A. Huuskonen, and M. Markkanen. Randomization of alternating codes: Improving incoherent scatter measurements by reducing correlations of gated autocorrelation function estimates. *Radio Science*, *32*(6), 2271–2282, 1997.

Lummerzheim, D. and J. Lilensten. Electron transport and energy degradation in the ionosphere: evaluation of the numerical solution, complarison with laboratory experiments, auroral observations. *Ann. Geophysicae*, *12*, 1039–1051, 1994.

Løvhaug, U. P. *Non-Maxwellian Ion Velcity Distributions and their Consequences on the Analysis and Interpretation of EISCAT Data*. PhD thesis, University of Tromsø, Tromsø, 1985.

Miller, K. L. and L. G. Smith. incoherent scatter radar observations of irregular structure in mid-latitude sporadic *E* layers. *J. geophys. Res.*, *83*, 3761–3775, 1978.

Min, Q.-L., D. Lummerzheim, M. H. Rees, and K. Stamnes. Effects of a parallel electric field and the geomagnetic field in the topside ionosphere on auroral and photoelectron energy distributions. *J. geophys. Res.*, *98*(A11), 19223–19234, 1993.

Mishin, E. and T. Hagfors. On heat flow contribution to plasma line frequency in the *F* region. *J. geophys. Res.*, *99*(A4), 6537–6539, 1994.

Mishin, E. and K. Schlegel. On incoherent scatter plasma lines in aurorae. *J. geophys. Res.*, *99*(A6), 11391–11399, 1994.

Nygrén, T. On the theory of sporadic *E*. In *La Hoz and Brekke* [1989], pages 105–121, 1989.

Nygrén, T., B. S. Lanchester, A. Huuskonen, L. Jalonen, T. Turunen, H. Risbeth, and A. P. van Eyken. Interference of tidal and gravity waves in the ionosphere and an associated sporadic *E*-layer. *J. atmos. terr. Phys.*, *52*(6–8), 609–623, 1990.

Opgenoorth, H., I. Häggström, P. J. S. Williams, and G. O. L. Jones. Regions of strongly enhanced perpendicular electric fields adjacent to auroral arcs. *J. atmos. terr. Phys.*, *52*(6–8), 449–458, 1990.

Oran, E. S., V. B. Wickwar, W. Kofman, and A. Newman. Auroral plasma lines: A first comparison of theory and experiment. *J. geophys. Res.*, *86*(A1), 199–205, 1981.

Perkins, F. and E. E. Salpeter. Enhancement of plasma density fluctuations by nonthermal electrons. *Phys. Rev.*, *139*(1A), A55–A62, 1965.

Perkins, F., E. E. Salpeter, and K. O. Yngvesson. Incoherent scatter from plasma oscillations in the ionosphere. *Phys. Rev. Letters*, *14*, 579, 1965.

Rietveld, M. T., P. N. Collis, and J.-P. St.-Maurice. Naturally enhanced ion acoustic waves in the auroral ionosphere observed with the EISCAT 933-MHz radar. *J. geophys. Res.*, *96*(A11), 19291–19305, 1991.

Rietveld, M. T., P. N. Collis, A. P. van Eyken, and U. P. Løvhaug. Coherent echoes during EISCAT UHF common programmes. *J. atmos. terr. Phys.*, *58*(1–4), 161–174, 1996.

Risbeth, H., A. P. van Eyken, B. S. Lanchester, T. Turunen, J. Röttger, C. Hall, and U.-P. Hoppe. EISCAT VHF radar observations of periodic mesopause echoes. *Planet. Space Sci.*, *36*(4), 423–428, 1988.

Robinson, P. A. Nonlinear wave collapse and strong turbulence. *Rev. Mod. Phys.*, *69*(2), 507–573, 1997.

Rosenbluth, M. N. and N. Rostoker. ——. *Phys. Fluids*, *5*, 776, 1962.

Rostoker, N. Test particle method in kinetic theory of a plasma. *Phys. Fluids*, *7*(4), 491, 1964.

Rottmann, K. *Mathematische Formelsammlung*. Bibliographisches Institut, 1984.

Röttger, J. and C. La Hoz. The structure and dynamics of polar mesosphere summer echoes observed with the EISCAT 224 MHz radar. *Geophys. Res. Lett.*, *15*(2), 1353–1356, 1988.

Salpeter, E. E. Electron density fluctuations in a plasma. *Phys. Rev.*, *120*(5), 1528–1535, 1960.

Salpeter, E. E. Density fluctuations in a nonequilibrium plasma. *J. geophys. Res.*, *68*(5), 1321, 1963.

Schunk, R. W. and J. C. G. Walker. Behaviour of ion velocity distributions in the auroral ionosphere. *Planet. Space Sci.*, *20*, 2175–2191, 1972.

Sharp, R. D. and P. B. Hays. Low-energy auroral electrons. *J. geophys. Res.*, *79*(28), 4319–4321, 1974.

Søraas, F., H. R. Lindalen, K. Måseide, A. Egeland, T. A. Sten, and D. S. Evans. Proton precipitation and the Hβ emission in a postbreakup auroral glow. *J. geophys. Res.*, *79*(13), 1851–1859, 1974.

St.-Maurice, J.-P. and R. W. Schunk. Behaviour of ion velocity distributions for a simple collision model. *Planet. Space Sci.*, *22*, 1–18, 1974.

Stamnes, K. and M. H. Rees. Inelastic scattering effects on photoelectron spectra and ionospheric electron temperature. *J. geophys. Res.*, *88*, 6301–6309, 1983.

Sulzer, M. P. A radar technique for high range resolution incoherent scatter autocorrelation function measurements utilizing the full power of klystron radars. *Radio Science*, *21*(6), 1033–1040, 1986.

Sulzer, M. P. Recent incoherent scatter techniques. *Adv. Space Res.*, *9*(5), 153–162, 1989.

Sulzer, M. P. A new type of alternating code for incoherent scatter measurements. *Radio Science*, *28*(6), 995–1001, 1993.

Summers, D. and R. M. Thorne. The modified plasma dispersion function. *Phys. fluids B*, *3*(8), 1835–1847, 1991.

Summers, D. and R. M. Thorne. A new tool for analyzing microinstabilities in space plasmas modeled by a generalized Lorentzian (kappa) distribution. *J. geophys. Res.*, *97*(A11), 1835–1847, 1992.

Texas Instruments. *TMS320C4x User's Guide*, 1992. SPRU063 Part number 2564090-9721 revision A.

Thorne, R. M. and D. Summers. Landau damping in space plasmas. *Phys. fluids B*, *3*(8), 2117–2123, 1991.

Trulsen, J. and N. Bjørnå. The origin and properties of thermal fluctuations in a plasma. In *Brekke* [1977], pages 29–54, 1977. ISBN 82-00 02421-0.

Törustad, B. W. *CORLAN — CORrelator LANguage*. Technical Report 82/36, EISCAT Scientific Association, Kiruna, Sweden, 1982.

Turunen, T. *The GEN-System for the EISCAT incoherent scatter radars*. Technical Report 85/44, EISCAT Scientific Association, Kiruna, Sweden, 1985.

Turunen, T. GEN-SYSTEM—a new experimental philosophy for EISCAT radar. *J. atmos. terr. Phys.*, *48*(9–10), 777–785, 1986.

Turunen, T., T. Nygrén, A. Huuskonen, and L. Jalonen. Incoherent scatter studies of sporadic-E using 300 m resolution. *J. atmos. terr. Phys.*, *50*(4/5), 277–287, 1988.

Turunen, T., J. Silén, T. Nygrén, and L. Jalonen. Observation of a thin E_s layer by the EISCAT radar. *Planet. Space Sci.*, *33*(12), 1407–1416, 1985.

Valladares, C. E., M. C. Kelley, and J. F. Vickrey. Plasma line observations in the auroral oval. *J. geophys. Res.*, *93*(A3), 1997–2003, 1988.

Vasyliunas, V. M. A survey of low-energy electrons in the evening sector of the magnetosphere with OGO 1 and OGO 3. *Geophys. Res. Space Phys.*, *73*(9), 2839, 1968.

Venkat Raman, R. S., J.-P. St.-Maurice, and R. S. B. Ong. Incoherent scattering of radar waves in the auroral ionosphere. *J. geophys. Res.*, *86*, 4751–4762, 1981.

Wahlund, J.-E., F. R. E. Forme, H. J. Opgenoorth, and M. A. L. Persson. Scattering of electromagnetic waves from a plasma: enhanced ion acoustic fluctuations due to ion-ion two-stream instabilities. *Geophys. Res. Lett.*, *19*(19), 1919–1922, 1992.

Wall, L., T. Christiansen, and R. Schwartz. *Programming Perl*. O'Reilly and associates, 2nd edition, 1995.

Wannberg, G. The G2-System and general purpose alternating code experiments for EISCAT. *J. atmos. terr. Phys.*, *55*(4/5), 543–557, 1993.

Wannberg, G., I. Wolf, L.-G. Vanhainen, K. Koskenniemi, J. Röttger, M. Postila, J. Markkanen, R. Jacobsen, A. Stenberg, R. Larsen, S. Eliassen, S. Heck, and A. Huuskonen. The EISCAT Svalbard radar: a case study in modern incoherent scatter radar design. *Radio Science*, *32*(6), 2283–2307, 1997.

Weinstock, J. Correlation functions and scattering of electromagnetic waves by inhomogeneous and nonstationary plasmas. *Phys. Fluids*, *10*(9), 2065–2072, 1967.

Wickwar, V. B. Plasma lines in the auroral E layer. *J. geophys. Res.*, *83*(A11), 5186–5190, 1978.

Williams, P. J. S., G. O. L. Jones, B. Jones, H. Opgenoorth, and I. Häggström. High resolution measurements of magnetospheric electric fields. *J. atmos. terr. Phys.*, *52*(6–8), 439–448, 1990.

Wrenn, G. L. Satellite measurements of photoelectron fluxes. *Ann. Geophysicae*, *30*, 49–57, 1974.

Yngvesson, K. O. and F. Perkins. Radar Thomson scatter studies of photoelectrons in the ionosphere and Landau damping. *J. geophys. Res.*, *73*(1), 97–110, 1968.